Microwave cavity resonance spectroscopy on ultracold plasma
a proof-of-principle

Daamen, K.A.

Award date:
2019

Eindhoven University of Technology
Department of Applied Physics
Coherence and Quantum Technology Group

Supervisors:
M.A.W. van Ninhuijs, MSc.
Prof. dr. ir. O.J. Luiten

Microwave Cavity Resonance Spectroscopy on an Ultracold Plasma

a Proof-of-Principle

Kees Anton Daamen

October 2019

CQT 2019 – 22

Summary

In microwave cavity resonance spectroscopy (MCRS) the resonance frequency of a cavity mode is tracked to measure perturbations in the permittivity and permeability of the cavity medium as a function of time. As such, the technique can be used to study the electron density evolution of a plasma contained in the microwave cavity interior. The general goal at the heart of this thesis is to reverse the traditional measurement hierarchy and use a known, very controllable plasma to study and advance MCRS as a technique. The idea is to create an ultracold plasma (UCP) in the microwave cavity interior by two-step ionization of a cold atom cloud of ^{85}Rb atoms trapped in a magneto-optical trap (MOT). Experimental parameters of the MOT position, wavelength, power and overlap of the excitation and ionization lasers allow unprecedented control over the initial plasma parameters. The low temperatures of the plasma species, as low as tens of kelvin for the electrons and millikelvins for the ions, result in relatively long plasma lifetimes, and corresponding long MCRS measurement times, of about $\sim 100\,\mu$s. Once demonstrated, MCRS can be used as a new tool to study UCPs as well.

In this thesis a proof-of-principle MCRS experiment on a UCP is demonstrated using the grating based magneto-optical trap (GMOT) concept recently developed by the *Riis group* at the University of Strathclyde, Glasgow. In a traditional MOT three pairs of counter propagating laser beams are required to cool and trap atoms in the beam overlap region. The GMOT concept requires only one laser beam and a diffraction grating to achieve the same result, greatly simplifying microwave cavity design and MOT operation in the cavity interior. A microwave cavity with a cylindrical pillbox geometry has been designed, and the placement and dimensions of the optical access holes in the cavity walls have been optimized in numerical simulation. More specifically, the Q-factor of the fundamental TM_{010} cavity mode has been optimized to maximize the MCRS measurement sensitivity in the experiment. The microwave cavity has been commissioned, and the Q-factor, resonance frequency and electric field profile of the TM_{010} mode have been verified. Finally, a proof-of-principle experiment is conducted.

The unloaded Q-factor of the commissioned cavity measures $Q_{\mathrm{cav}} = 3848 \pm 8$ and has a resonance frequency of about 5 GHz. The Q-factor is very close to the simulated value $Q_{\mathrm{cav}} = 3990$, and close to the theoretical maximum of this cavity geometry $Q_{\mathrm{cav}} \sim 4250$. Optimization of the cavity design has been successful in mitigating the potential detrimental effects of the holes in the cavity walls on the Q-factor. Due to the installation of the grating and grating clamps in the microwave cavity interior, the Q-factor drops significantly to $Q_{\mathrm{cav}} = 491.0 \pm 0.3$. With 100 nm, the thickness of the aluminum grating reflector measures only a faction of the skin depth of the cavity fields ($\delta_s = 1.2\,\mu$m at 5 GHz). Due to its limited thickness, the surface resistance of the grating reflector ($R_S \sim 300\,\mathrm{m}\Omega$) is about a factor 6 higher than the surface resistance of the aluminum

cavity walls. Increased dissipation in the grating reflector results in the drop in Q-factor of the cavity mode. The effect is aggravated by concentration of surface currents on the reflector edges and near the grating clamps. This drop in Q-factor came as a surprise as the effect of the skin depth on the surface resistance of the grating reflector was not included in initial simulations. An idea to mitigate these problems is described in the outlook of this thesis. Preliminary simulations show the drop in Q-factor can be reduced to $Q_{\mathrm{cav}} \sim 3000$ by placing the grating 1 mm below the cavity back wall and ensuring maximal electrical contact between the wall and grating reflector.

The relatively large hole for the trapping laser does have a significant influence on the resonance frequency and field profile of the cavity mode. The analytical 'Bessel' shape of the radial electric field profile of the TM_{010} cavity mode is modified to a flattop profile with 'spikes' near the hole edge. The radial cavity electric field profile has been experimentally verified and is in good agreement with simulations. The changes in the cavity field profile, and mode resonance frequency, are not a problem in the experiment.

To house the cavity in a shared setup for grating based cold atom experiments, a custom flange with cavity support has been developed. Installed in the setup, the resonance frequency of an empty cavity has been determined with a reflection based measurement setup. At room temperature, the resonance frequency of the TM_{010} mode was determined to be $f_0 = 4.986\,\mathrm{GHz}$ and can be resolved with an RMS spread of $\sigma_{f_0} = 34\,\mathrm{Hz}$. The RMS resonance frequency spread σ_{f_0} is the minimum frequency shift that can be detected in the experiment. The detection limit corresponds to about 30 thousand electrons located on the cavity central axis, or a field averaged electron density of $\bar{n}_e = 4\times10^9\,\mathrm{m}^{-3}$. This is more than two orders of magnitude better than the previous record mentioned in scientific literature. A very good result.

We were successful in operating the GMOT in the microwave cavity interior by using a trapping laser beam with a flattop-like transverse intensity profile. To prevent MOT depletion in the experiment, the MOT loading time was approximately matched to the repetition period of the ionization laser (100 ms) by increasing the rubidium background pressure. At a background pressure of $p_{\mathrm{Rb}} = 2.2 \times 10^{-9}\,\mathrm{mbar}$ we were able to trap $N_a = (84.6 \pm 0.3) \times 10^6$ rubidium atoms in the MOT with a loading time $\tau_{\mathrm{load}} = 120 \pm 3\,\mathrm{ms}$. For the proof-of-principle experiment the MOT loading and ionization scheme was kept as simple as possible. UCPs were created by partial MOT ionization at a repetition rate of 10 Hz, while the MOT was continually loaded by the trapping laser. In the experiment the MOT atom number dropped to $N_a = (7.0 \pm 0.1) \times 10^7$ due to the recurrent ionization. The resonance frequency shift of the microwave cavity mode was recorded and fitted with a theoretical model for analysis. Qualitatively, the MCRS signal of the proof-of-principle experiment behaves as expected. Quantitatively the recorded resonance frequency shift is within 20% of the expected value determined through MOT fluorescence measurements and the known photoionization cross section. The MCRS signal shows possible signs of electron heating by the microwave cavity fields, that has to be investigated in more detail in future experiments. The possibility of the breakdown of the self-similar UCP expansion model as the plasma touches the nearest wall is another topic for future research. All-in-all a successful demonstration of a proof-of-principle MCRS experiment on a UCP.

Contents

Nomenclature

AC	Alternating Current
AOM	Acousto-Optic Modulator
CCD	Charge-Coupled Device
dBm	Power expressed in decibels with reference to 1 mW
DC	Direct Current
DIH	Disorder-Induced Heating
EOM	Electro-Optic Modulator
EUV	Extreme UltraViolet
FWHM	Full Width at Half Maximum
GMOT	Grating Magneto-Optical Trap
IC	Integrated Circuit
LSB	Least Significant Bit
MCRS	Microwave Cavity Resonance Spectroscopy
MOT	Magneto-Optical Trap
RMS	Root Mean Square
SEM	Scanning Electron Microscope
TE	Transverse Electric
TM	Transverse Magnetic
TTL	Transistor-Transistor Logic
UCP	UltraCold Plasma
UHV	Ultra-High Vacuum

1 Introduction

Over the last five decades the semiconductor industry has been driven by 'Moore's Law', doubling the number of transistors per dense integrated circuit (IC) about every two years [1]. A straightforward shrink of transistor dimensions has been the primary avenue of achieving this drive, resulting in ever more stringent requirements for IC production and tools. Photolithography is the workhorse of the semiconductor industry and the limiting process step in manufacturing of dense integrated circuits. A schematic representation of the photolithographic process is shown in Fig. 1.1. The reticle, a photomask with the negative of the IC pattern for a specific processing step, is illuminated by a light source. Subsequently the image of the IC pattern is projected onto a semiconductor wafer covered with a photoresistive layer by a projection (lens) system. After illumination, further processing steps yield the IC structure desired.

In photolithography the smallest printable feature size is called the critical dimension CD. It is determined by the maximum resolution of the projection system, and given by [2]:

$$\mathrm{CD} = k_1 \frac{\lambda}{n \sin \theta}, \tag{1.1}$$

with λ the wavelength of the light used for illumination, and $n \sin \theta$ the numerical aperture of the projection system as seen from the wafer. Here n is the refractive index of the medium surrounding the wafer, θ is the maximum half-angle of the projection system, and k_1 an empirical process parameter dependent on the photoresist properties and details of the light field used for illumination (angle distribution, coherence, etc.).

From Eq. 1.1 it is clear the critical dimension can be reduced by decreasing the wavelength of the light used for illumination. Historically this is what has been done. Photolithography tools started out using emission lines from mercury discharge lamps [3]. First the 406 nm line, later the 365 nm line. The development of excimer lasers allowed the wavelength to be reduced further down to 248 nm (KrF) and 193 nm (ArF). Nowadays 193 nm lithography tools are used for processing steps in high-volume production requiring the smallest critical dimensions. However, the technology is stretched to its practical limits requiring multiple patterning steps for the critical layers.

For the next 'technology node' the semiconductor industry has agreed on photolithography using extreme ultraviolet (EUV) light at 13.5 nm. This has profound implications for photolithography tools. A 13.5 nm photon carries about 92 eV of energy and is absorbed by almost all known materials. For example more than 99% of photons are absorbed after 1 mm of propagation in air at standard pressure. Hence EUV lithography tools are operated in vacuum conditions and use reflective optics (mirrors) in the projection system. ASML's NXE:3400B EUV lithography tools are on the brink of high volume manufacturing [4].

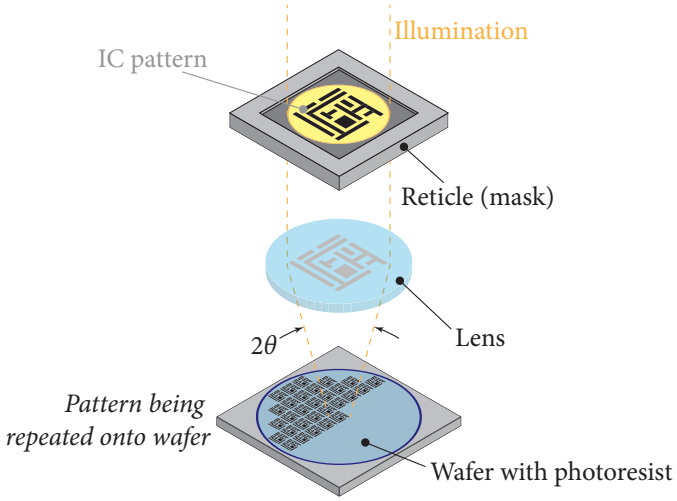

Figure 1.1: The photolithographic process – schematic. A mask with an IC pattern is illuminated. The pattern image is projected onto a semiconductor wafer with photoresist by a lens [5].

One of the many remaining challenges in EUV production tools is in the optimization of the EUV source. The EUV source in ASML's current NXE:3400B flagship machine is a laser-produced plasma source. At a repetition rate of 50 kHz tiny tin (Sn) droplets are ionized and heated by multiple laser pulses. The hot, highly ionized tin plasma emits light at 13.5 nm. After collection, 250 W EUV light enters the machine at intermediate focus [4]. Current EUV lithography machines are not equipped with metrology tools for the EUV beam (measuring beam power and position) as the available technology lacks the time ($> 10\,\mu$s) and spatial ($> 10\,\mu$m) resolution required. Moreover beam sampling would result in loss of EUV beam power available for illumination. With an EUV beam monitor valuable information could be obtained for optimization of important operational machine characteristics as wafer yield, throughput and machine uptime, even if only in the research phase of machine development. The ionizing quality of EUV light might open up possibilities for contactless beam metrology.

1.1 A Microwave Cavity as an EUV Beam Monitor

An EUV photon of 92 eV carries more than sufficient energy for single photoionization of all elements in the periodic system. Hence atoms and molecules in the background gas are ionized all along the beam path in the lithography tool. After ionization, most of the excess photon energy is transferred to the electron. The electron kinetic energy is sufficient to create secondary electrons by impact ionization:

$$\mathrm{X} + \gamma \rightarrow \mathrm{X}^+ + \mathrm{e}^-,$$
$$\mathrm{X} + \mathrm{e}^- \rightarrow \mathrm{X}^+ + 2\mathrm{e}^-,$$

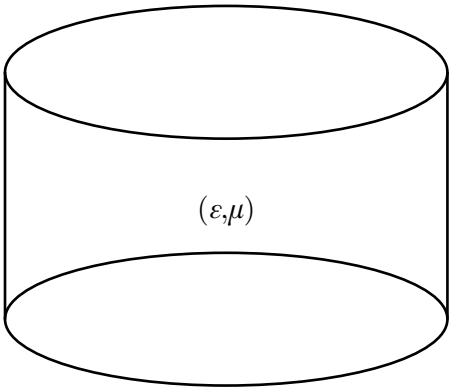

Figure 1.2: Cylindrical geometry microwave cavity with linear isotropic medium (ε, μ).

where X denotes an arbitrary atom or molecule, γ represents an EUV photon and e^- a free electron. With electrons and ions separated, a plasma is formed all along the beam path [3]. The term plasma describes a wildly varying range of media. All plasmas in this thesis are assumed to be macroscopically neutral. In a plasma electrons shield the ions from fluctuations in the electronic potential up to a characteristic angular frequency, the electron plasma frequency ω_{pe}:

$$\omega_{pe} = \sqrt{\frac{e^2 n_e}{\varepsilon_0 m_e}}, \tag{1.2}$$

where ε_0 is the permittivity of free space, m_e and n_e are the electron mass and density respectively, and e is the elementary charge. Commonly the electron prefix is dropped and ω_{pe} is referred to as the plasma frequency. A plasma absorbs electromagnetic radiation below the plasma frequency ($\omega < \omega_{pe}$). Above the plasma frequency ($\omega > \omega_{pe}$) the plasma is transparent, with a permittivity ε given by:

$$\varepsilon = \varepsilon_0 \left(1 - \frac{\omega_{pe}^2}{\omega^2}\right). \tag{1.3}$$

With knowledge of the background gas composition and photoionization cross sections, a localized measurement of the plasma permittivity (electron density) allows the power and position of the EUV beam to be computed. Microwave cavity resonance spectroscopy (MCRS) is a technique that can be utilized to achieve this goal.

A microwave cavity is a space, filled with a linear isotropic medium with permittivity ε, and permeability μ enclosed by metal boundary walls. The metal structure itself is referred to as the *cavity*, the enclosed as the *cavity medium*. In general, cylindrical cavity geometries are used with MCRS, see Fig. 1.2. When excited with electromagnetic radiation, the cavity exhibits resonances at a series of characteristic (angular) frequencies ω_n, $n \in \mathbb{N}$ in the microwave frequency regime. At resonance, standing waves form in the cavity medium and the wave amplitude is amplified. A specific resonance is called a 'mode' and the mode (resonance) frequency ω_n is dependent on the cavity geometry,

dimensions and cavity medium properties (ε, μ). For simplicity the next discussion is restricted to a single mode ω.

A perturbation in the permittivity ($\Delta\varepsilon = \varepsilon' - \varepsilon$) and/or permeability ($\Delta\mu = \mu' - \mu$) of the cavity medium will result in a shift in the mode frequency ($\Delta\omega = \omega' - \omega$). Here the $'$-accent denotes the perturbed case. Perturbations in the cavity medium are related to the resonance frequency shift by *Slater's perturbation theorem*. For small perturbations ($\Delta\varepsilon, \Delta\mu \to 0$, the theorem takes the form [5, 6]:

$$\frac{\omega' - \omega}{\omega} = -\frac{\iiint_{\text{cav}} \left(\Delta\varepsilon E^2 + \Delta\mu H^2\right) \mathrm{d}^3\mathbf{x}}{\iiint_{\text{cav}} \left(\varepsilon E^2 + \mu H^2\right) \mathrm{d}^3\mathbf{x}}, \tag{1.4}$$

where E and H are the amplitudes of the electric and auxiliary magnetic field belonging to mode ω, $\mathbf{x}$ is the position vector in a suitable 3D coordinate, and $\mathrm{d}^3\mathbf{x}$ denotes a volume element for the integration. Electric and magnetic fields obey the usual relations:

$$D = \varepsilon E, \qquad\qquad B = \mu H, \tag{1.5}$$

with D and B the displacement field and magnetic field amplitude respectively. The mode fields in Eq. 1.4 are integrated over the full cavity dimensions and the denominator $\iiint_{\text{cav}} \left(\varepsilon E^2 + \mu H^2\right) \mathrm{d}^3\mathbf{x}$ resembles the energy contained in the cavity fields. Clearly, for small perturbations $\Delta\varepsilon$ and $\Delta\mu$, the relative change in resonance frequency goes as the relative change in energy stored in the cavity fields.

When using a microwave cavity to measure the plasma permittivity and permeability it is convenient to start with an 'empty' or vacuum cavity, where $(\varepsilon, \mu) = (\varepsilon_0, \mu_0)$, and perturb it with the plasma under study. Assuming $\Delta\mu = 0$, and using Eqs. 1.3 and 1.2 we can rewrite Eq. 1.4 in terms of the plasma electron density. Details of this derivation will be discussed in Ch. 3 and result in:

$$\bar{n}_e \equiv \frac{\iiint_{\text{cav}} n_e\left(\mathbf{x}\right) E^2\left(\mathbf{x}\right) \mathrm{d}^3\mathbf{x}}{\iiint_{\text{cav}} E^2\left(\mathbf{x}\right) \mathrm{d}^3\mathbf{x}}, \tag{1.6}$$

where $\bar{n}_e$ is the field-averaged electron density and we have written spatial dependencies explicitly. An MCRS measurement using one mode will yield a volume-averaged measurement value $\bar{n}_e$ in which the local electron density of the perturbation is weighted by the *square* of the local electric field amplitude. The technique is *sensitive* to electron densities located in an antinode of the mode pattern (bulge of the standing wave), and *insensitive* to densities located in a node (zero crossing). Obviously, for a pulsed source, the electron density will have a temporal dependence $n_e\left(\mathbf{x}, t\right)$, as will the measurement result $\bar{n}_e\left(t\right)$, where the variable t denotes time. The temporal dependence in the electron density can be resolved up to the temporal resolution of the cavity used for measurement.

For microwave cavities with resonant frequencies in the GHz range, submicrosecond temporal resolution can be easily achieved. Passing an EUV beam through two small holes in a microwave cavity allows the field-averaged electron density of the locally generated plasma to be determined through MCRS. This technique can be utilized to develop a contactless EUV beam monitor. Once developed, the beam monitor can be used to analyze other sources of ionizing radiation as well, for instance in monitoring the beam power of the X-Ray free electron laser FERMI in Trieste, Italy.

In 2016 a research project was started at the Eindhoven University of Technology to develop an EUV beam monitor. The research project is a collaboration between the *EPG group* and the *CQT group* at the faculty of Applied Physics, the company ASML and the research institution FERMI at Elettra. The project consists of two research lines:

1. Develop an EUV beam monitor with spatial resolution based on *multimode* MCRS. Different cavity modes ω_n have different spatial sensitivities based on their respective mode patterns. Combining MCRS measurements of a suitable combination of cavity modes, the plasma electron density can be reconstructed spatially. The project delivered its first results, which are published in Ref. [7].

2. Study –and possibly improve– the understanding of MCRS as a plasma diagnostic by reversing the measurement hierarchy. Starting from a model plasma with fine control over the electron density distribution, and evolution $n_e(\mathbf{x}, t)$, the interaction between the plasma and cavity fields can be researched.

The project described in this thesis is part of the second research line.

1.2 An Ultracold Model Plasma

On earth, a plasma is an unstable state of matter. Free electrons and ions inevitably collide with other atoms and molecules, slow down and recombine. Hence to start a plasma it needs to be 'ignited', and for a plasma to stay 'alive' it needs an ongoing source of ionization to offset the recombination. Main plasma characteristics as electron and ion temperature, electron density, plasma size and lifetime depend on the technique used for ionization and the medium being ionized. Typically, ionization is the result of particle collisions and the resulting plasma has a temperature in the order of the ionization potential. For most atomic and molecular species the ionization potential is in the order of 1 eV, resulting in an initial electron temperature of order 10^4 K or higher.

The first goal of research line two is to create a model plasma with a well defined, *controllable* evolution of the electron density distribution within the confinement of a microwave cavity. In a plasma, the speed of plasma processes (e.g. expansion) is governed by the thermal energy available in the system. As the ionization process only adds energy to the system, *control* means *cold*. Maximum control is achieved when combining a low thermal energy ionization medium with a controlled ionization process adding as little energy to the system as possible. Arguably the ionization process that yields most control over the resulting plasma properties is photoionization. Combining the best of

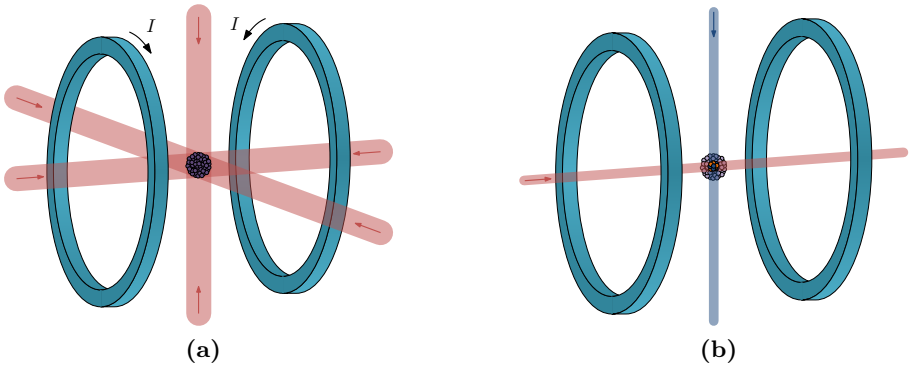

Figure 1.3: Creation of an ultracold plasma (UCP) [8]. **(a)** Two coils in anti-Helmholtz configuration create an quadrupole magnetic field. Three counter-propagating red-detuned laser beam pairs cool and trap atoms in the zero crossing of the quadrupole. **(b)** An ultracold plasma is created by two-step photoionization. The trap transition (red laser) is reused as the intermediate state.

both worlds the idea is to create an *ultracold* model plasma by two-step photoionization of a cloud of laser-cooled gas.

In a diluted gas, an atom (or molecule) in motion can be slowed down by a counter-propagating laser beam slightly red-detuned from a closed optical transition (Doppler cooling). In the overlap region of six counter-propagating red-detuned laser beams one has control over the atom velocity distribution in three dimensions. In a magneto-optical trap (MOT), laser cooling is made position-dependent with the use of a quadrupole magnetic field, see Fig. 1.3a. In the trap about 10^8 atoms can be trapped and cooled down to a temperature in the order of $100\,\mu$K, dependent on the atomic species and limited by the stochastic nature of the cooling process. Typically the cloud of cold atoms, the 'MOT', has a Gaussian density distribution with a size of order 1 mm and a peak density of $1\times10^{16}\,\mathrm{m}^{-3}$ [9]. This is our cold ionization medium. Two-step photoionization is performed by reusing the cooling transition as an intermediate state (red laser). In a second step the electrons are photoionized to the continuum (blue laser), see Fig. 1.3b. By manipulating the position, intensity profile, overlap and power of the excitation and ionization lasers we have control over the initial plasma density distribution. By changing the wavelength of the ionization laser we have control over the excess photon energy above the ionization threshold. As practically all excess photon energy is carried away by the electrons, we can set the initial electron temperature T_e of the system. The ion temperature T_i follows the temperature of the ionization medium. The electron temperature can be as low as the ionization laser bandwidth, which is easily below 1 K. This is exceptionally cold for earth bound plasmas, hence the name *ultracold* plasma (UCP). In general, the initial UCP density distribution follows the Gaussian density distribution of the ionization medium. A Gaussian initial density distribution leads to a self-similar expansion, with a UCP expansion velocity of order 100 m/s. Moreover, above 50 K the expansion velocity is only determined by the initial electron temperature [10,

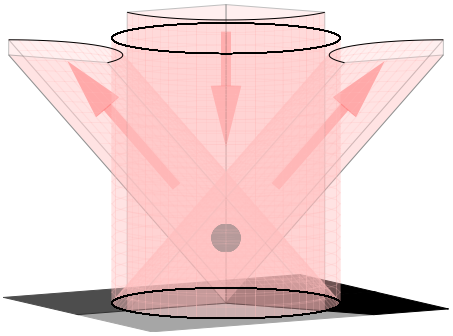

Figure 1.4: The grating magneto-optical trap (GMOT) concept. An incoming laser beam (↓), together with three first order diffracted beams (↖↑↗) span an overlap volume in which a MOT (gray) can be created. Adapted from [12].

11]. This will be our ultracold model plasma.

Aligning six laser beams out of sight within the confinement of a microwave cavity is a cumbersome prospect. Laser alignment is critical as light balance at the MOT position is required for successful MOT operation. Moreover, the six large holes in the cavity walls required for optical access complicate cavity design and can be detrimental to its quality as a resonator. Recently the *Riis group* from the University of Strathclyde in Glasgow has developed a MOT concept utilizing a diffraction grating etched in a silicon chip, the grating magneto-optical trap (GMOT) [13]. The concept requires a single incoming laser beam and creates a MOT in the overlap volume spanned by the incoming beam, together with the first diffracted orders of the grating, see Fig. 1.4. Designing an MCRS experiment utilizing the GMOT concept results in a significant reduction of complexity in cavity design and MOT operation.

1.3 This Thesis

The goal of the project described in this thesis is to conduct a proof-of-principle MCRS measurement on an ultracold plasma created with the GMOT concept. The main focus will be on microwave cavity design. This thesis is organized as follows:

The details of laser cooling and trapping, the subsequent photoionization and resulting ultracold plasma are discussed in Ch. 2. Chapter 3 deals with microwave cavity theory and the theoretical background of microwave cavity resonance spectroscopy. Estimations important for cavity design are made throughout these two theoretical chapters. Microwave cavity design and commissioning is discussed in Ch. 4. In Ch. 5 the MCRS setup is characterized, and a proof-of-principle MCRS experiment on a UCP is demonstrated. Finally, this thesis is concluded in Ch. 6 and an outlook for future research is discussed in Ch. 7.

2 Ultracold Plasma

After the solid, liquid and gas phase plasma is sometimes considered the fourth state of matter. The free electrons and ions interact over relative long distance through the Coulomb force giving the medium its characteristic properties. One of the ways to characterize a plasma is by the electron temperature. On earth, most plasmas are man made with an electron temperature of 10^3 K or higher [11]. Ionizing laser cooled gasses can lead to electron and ion temperatures below 10 K, hence the name *ultracold* plasma (UCP). This chapter deals with the creation of such a plasma from a laser cooled cloud of ^{85}Rb-atoms in a magneto-optical trap (MOT).

Microwave cavity resonance spectroscopy (MCRS) is a plasma diagnostic measuring the plasma electron density. As such the total number of electrons in the plasma is an important parameter to estimate whether we will have enough signal for detection. Throughout this chapter estimates will be made for these calculations.

A general introduction to the MOT concept is described in Sec. 2.1 together with the equations used to determine the MOT characteristics (number of atoms, loading rate) through fluorescence measurements. Details of the cooling and trapping of ^{85}Rb are discussed in Sec. 2.2. Section 2.3 introduces the grating magneto-optical trap (GMOT) concept. The grating principles are explained and the resulting GMOT characteristics (number of atoms, temperature) estimated. In Sec. 2.4 the two-step photoionization process used to ionize the ^{85}Rb-atoms is discussed, and an estimation of the number of electron-ion pairs is made. The resulting UCP serves as a model plasma for the main goal of this thesis, a proof-of-principle MCRS measurement. Plasma processes, evolution and relevant timescales for the experiment are discussed in Sec. 2.5. Finally, all relevant parameters for the experiment and cavity design are summarized in Sec. 2.6.

2.1 Magneto-Optical Trap

In this section a coarse, high-level introduction to the MOT concept is given. For details the reader is referred to other texts, for instance Ref. [9].

Consider a simple two-level atom with a ground state and an excited state. The electronic transition from the ground to the excited state is resonant with a photon of frequency ν_*, it has a FWHM natural linewidth Γ and a corresponding excited state lifetime $\tau_* = 1/(2\pi\Gamma)$. For a two-level atom at rest and in a light field, the rate R_a at which photons are scattered is given by a Lorentzian profile:

$$R_a(I_\delta, \delta) = \pi\Gamma \frac{I_\delta/I_S}{1 + I_\delta/I_S + (2\delta/\Gamma)^2}, \tag{2.1}$$

with I_δ the intensity of the light field, I_S the saturation intensity of the transition, and $\delta = \nu - \nu_*$ the detuning of the light frequency ν with respect to resonance. In the remainder of this section all atoms will be treated with this two-level atom picture.

For an atom traveling at velocity $\mathbf{v}$, laser light with frequency ν in the lab frame is Doppler shifted to $\nu' = \nu - \mathbf{k} \cdot \mathbf{v}$. With $\mathbf{k}$ the wave vector of the laser light in the direction of propagation, $|\mathbf{k}| = 1/\lambda$. $\lambda = c/\nu$ the laser wavelength and c the speed of light. In the remainder of this thesis vectors are denoted in bold to distinguish them from scalars. For simplicity the next discussion is held in one dimension. It will be extended to three dimensions later this section. For a *red* detuned laser beam ($\delta < 0$), and a counter propagating atom with velocity v_x, the laser light can become resonant with the electronic transition due to the aforementioned Doppler shift. If so, the atom slows down –is *cooled*– due to radiation pressure. Conversely, a *blue* detuned laser beam ($\delta > 0$) can cause acceleration, or *heating* of the atom. For an atom in *two* equal intensity counter propagating red detuned laser beams, the first-order Taylor expansion of the force acting upon the atom is given by:

$$F_{\text{cool}} \cong -\alpha v_x, \tag{2.2}$$

with $\alpha = \alpha\left(I_\delta, \delta\right)$ an intensity and detuning dependent constant. F_{cool} is a damping force with α the damping constant. Atoms with initial velocities below a specific capture velocity v_c experience a damping force in the light field and are cooled. An atom in such a light field behaves as if it were traveling through *optical molasses*, hence the popular name of the technique. Due to the stochastic nature of the cooling process, atoms in optical molasses are not cooled down to absolute zero. In the limit of low intensity ($I_\delta \ll I_S$) and optimal detuning ($\delta = -\Gamma/2$), the cooling process is limited to the so-called Doppler temperature limit, or Doppler temperature T_D:

$$T_D = \frac{h\Gamma}{2k_B}, \tag{2.3}$$

with h the Planck constant and k_B the Boltzmann constant. The Doppler temperature typically measures several hundred microkelvin, dependent on the atomic species and transition used for cooling. Associated with the Doppler temperature is a one dimensional velocity $v_D = \sqrt{k_B T_D / m_a}$, with m_a the atomic mass of the species concerned. The Doppler velocity typically measures in the order of 10 cm/s.

The technique of optical molasses can be extended to three dimensions with a proper combination of N red detuned laser beams. For N beams with propagation vectors $\{\mathbf{k}_1, \mathbf{k}_2, \ldots \mathbf{k}_N\}$, the same detuning $\delta_i = \delta < 0$ and intensities $\{I_1, I_2, \ldots I_N\}$. One ends up with optical molasses provided the intensities add up to zero in three dimensions, $\sum_{i=1}^{N} I_i \cdot \mathbf{k}_i = \mathbf{0}$. In most common configurations $N = 4 - 6$. Applying the technique of optical molasses one gains control over the *velocity* distribution of an atomic species. Atoms are slowed down, but still move in and out of the cooling region. To gain control over the atom *position* distribution requires a second technique discussed next.

Again consider a two-level atom with a ground state and an excited state, in one dimension. The ground state has a total electronic angular momentum quantum number $J_g = 0$, and an excited state $J_e = 1$. In an external magnetic field the three degenerate

magnetic quantum levels of the excited state M_e = -1, 0, +1 separate and become distinguishable (Zeeman effect). Due to the quantum mechanical selection rules electronic transitions ΔM = -1, 0, +1 are driven by photons with σ^-, π and σ^+ polarizations respectively. Here σ^- (σ^+) denotes a photon with circular polarization, rotating in the clockwise (anti-clockwise) direction with respect to the quantization axis, the direction of the local magnetic field. π denotes a linear polarization. For a careful combination of two counter propagating circular polarized (σ^- and σ^+), red detuned ($\delta^- = \delta^+ = \delta < 0$) laser beams and a magnetic field that varies linear with position ($B_x = bx$, with b the linear magnetic field gradient), the radiation pressure exerted upon the atom takes the form of a restoring force around the zero crossing of the B-field:

$$F_{\text{trap}} = -\frac{\alpha\beta}{k_x}x, \tag{2.4}$$

where $\beta = \beta(b)$ is a constant depending on the local magnetic field gradient. Atoms deviating from a position $x = 0$ are pushed back, effectively holding them in place. There are very few atoms with strict $J_g = 0$ to $J_e = 1$ transitions, however this scheme can be extended to all atomic transitions where $J_g \to J_e = J_g + 1$ as well.

Combining the cooling force of Eq. 2.2 with the restoring force of Eq. 2.4 results in:

$$F_{\text{MOT}} = -\alpha v_x - \frac{\alpha\beta}{k_x}x, \tag{2.5}$$

where F_{MOT} is the time-averaged force exerted upon the atom. Eq. 2.5 is a good 1D approximation of the force atoms experience in a magneto-optical trap [9]. This force results in cooling and trapping atoms in the region around the zero crossing of the magnetic field. Cooling and trapping in three dimensions is achieved by combining a set of N lasers with appropriate polarizations, intensities and detunings (the same requirement as in the case of optical molasses), with an appropriate magnetic field. Although it is an example of sloppy language use, both the technique and the resulting cloud of cold atoms are referred to as a MOT.

A magnetic field that varies linear with position around a zero crossing in three dimensions can be constructed with two coils in anti-Helmholtz configuration. Consider two coils placed along the z-axis. The current through the coils is flowing in opposite direction with respect to each other (anti-Helmholtz configuration). The resulting field pattern is a quadrupole magnetic field. For an impression of the field in a plane containing the z-axis see Fig. 2.1. Arrows in the figure follow magnetic field lines, logarithmic field intensity is given in blue. The field in the region of the zero crossing (white region in the center of Fig. 2.1) is given by $\mathbf{B}_{\text{MOT}} = b\left(-\frac{x}{2}, -\frac{y}{2}, z\right)$ and ticks all the boxes required for MOT operation.

In three dimensions, the force of Eq. 2.5 results in a Gaussian density distribution of the trapped atoms:

$$n_a(\mathbf{x}) = n_{a0}\exp\left(-\frac{x^2}{2\sigma_{ax}^2} - \frac{y^2}{2\sigma_{ay}^2} - \frac{z^2}{2\sigma_{az}^2}\right), \tag{2.6}$$
$$n_{a0} = \frac{N_a}{\sqrt{2\pi}^3\sigma_{ax}\sigma_{ay}\sigma_{az}},$$

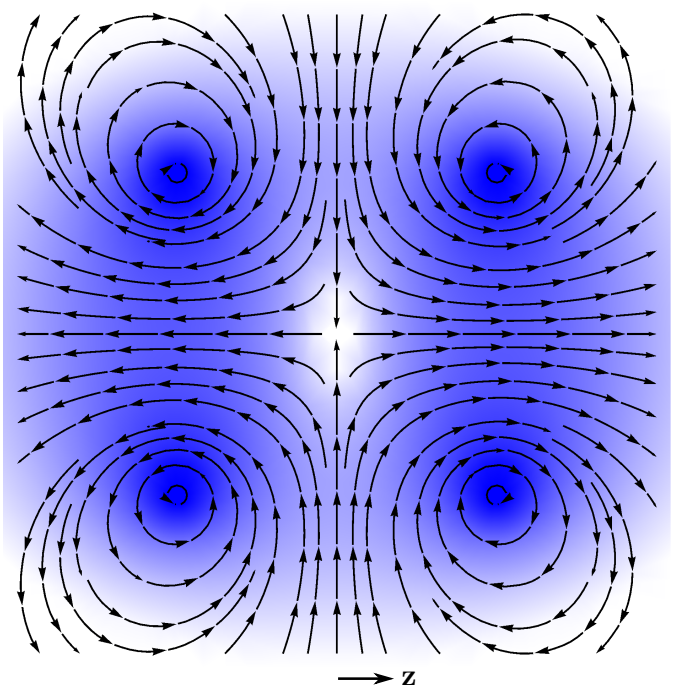

Figure 2.1: Schematic plot of a quadrupole magnetic field $\mathbf{B}_{\mathrm{MOT}}$ in a plane containing the z-axis. Arrows follow field lines, logarithmic field intensity given in blue. Note $\mathbf{B}_{\mathrm{MOT}} = \mathbf{0}$ at the MOT position, in the center of the image.

with $n_a(\mathbf{x})$ the atomic density distribution, $\mathbf{x} = (x, y, z)$ the position vector, and n_{a0} the peak atom density. The total number of trapped atoms is given by N_a, and σ_{al} is the RMS size of the distribution in the direction of coordinate $l = x, y, z$. The spontaneously emitted photons of the trapping process are on resonance and can easily be absorbed by an adjacent atom. The resulting radiation pressure is directed radially outward and limits the peak density in the center of the distribution to a typical value of $n_{a0} \sim 1 \times 10^{16}\,\mathrm{m}^{-3}$ [9, 14].

Quantitative determination of $n_a(\mathbf{x})$ can be achieved with the help of a CCD camera. The scattering rate in Eq. 2.1 defines the number of photons scattered per atom and unit of time. Knowing the quantum efficiency and shutter time of the camera, given the solid angle covered by the camera sensor, the characteristics of the density profile N_a and σ_{al} can be determined by fitting the camera image with a 2D Gaussian profile. Obviously one camera position only yields spatial information in the plane perpendicular to the normal of the camera sensor.

The number of trapped atoms at a specific point in time $N_a(t)$ is determined by the differential equation:

$$\frac{dN_a}{dt} = R_{_L} - \Gamma_{\mathrm{BG}} N_a, \tag{2.7}$$

with proper boundary conditions. Here $R_{_L}$ is the loading rate, and Γ_{BG} is the linear loss rate; the rates at which atoms in the MOT are loaded from, and lost by collisions with, hot background atoms respectively. With the boundary condition of $N_a(0) = 0$, integrating Eq. 2.7 yields:

$$N_a(t) = \frac{R_{_L}}{\Gamma_{\mathrm{BG}}} \left(1 - \exp\left(-\Gamma_{\mathrm{BG}} t\right)\right). \tag{2.8}$$

For instance, the aforementioned boundary condition can be realized by switching on the lasers used for cooling and trapping at $t = 0$. The factor $R_{_L}/\Gamma_{\mathrm{BG}}$ in Eq. 2.8 is the maximum number of trapped atoms at long times ($t \gg \Gamma_{\mathrm{BG}}^{-1}$) and corresponds to N_a in Eq. 2.6. $R_{_L}$ and Γ_{BG} can be determined from a series of fluorescence measurements of a loading MOT at successive time steps t_i. Fitting the series $N_a(t_i)$ with Eq. 2.8 yields the rates sought. $R_{_L}$ and Γ_{BG} are pressure dependent constants. $R_{_L}$ is dependent on the partial pressure p_a of the atomic species used for trapping , and Γ_{BG} is dependent on the total background pressure p. For stable MOT operation $p = p_a + p_{_X}$ is typically below a few times $10^{-8}\,\mathrm{mbar}$, here $p_{_X}$ denotes the sum of the partial pressures of all other atomic species in the background. It originates from the residual gas left after pumping down the vacuum vessel and from the outgassing of the vessel materials. For $p_a/p_{_X} \gg 1$ the ratio $R_{_L}/\Gamma_{\mathrm{BG}}$ is essentially constant although both rates increase with pressure. To end up in this regime with some room for error $p_{_X}$ is preferably below $10^{-9}\,\mathrm{mbar}$, or in the UHV regime. This is an important consideration for the design of the vacuum setup, pumps and materials used.

Table 2.1: Rubidium-85 data for laser cooling with the $\left(5^2\mathrm{S}_{1/2},\, F=3 \rightarrow 5^2\mathrm{P}_{3/2},\, F'=4\right)$ transition [18].

Quantity	**Symbol**	**Value**	
Atomic mass	m_a	84.91	u
Wavelength (in *vacuum*)	λ_*	780.24	nm
Natural linewidth	Γ	6.07	MHz
Excited state lifetime	τ_*	26.23	ns
Saturation intensity	$I_{_S}$	1.67	mW/cm^2
Doppler temperature	$T_{_D}$	145.57	μK
Doppler velocity	$v_{_D}$	11.94	cm/s

2.2 Rubidium-85

The most obvious candidates for magneto-optical trapping are atomic species with transitions most closely resembling the two-level atom picture of the previous section. Alkali metals, with one electron in the outer shell and all other shells fully populated, are the closest match. Alkali earth metals, with an additional electron in the outer shell, and metastable noble gasses, where one outer shell electron is in a high metastable state, are still quite easy to cool and trap. Laser cooling and trapping of rare earth metals and molecules has been achieved, but is in general an Herculean task [15, 16].

In this research rubidium-85 (^{85}Rb) is used. ^{85}Rb is one of the workhorses in atomic physics. Its outer electron has a closed optical transition usable for magneto-optical trapping in a wavelength region where cheap commercial high power diode lasers are available, hence the popularity. The cooling and trapping scheme is operated between the $5^2\mathrm{S}_{1/2}$ and $5^2\mathrm{P}_{3/2}$ energy levels. Here the electron energy level is denoted with the Russell-Saunders term symbol $n^{2S+1}L_J$. All letters in the term symbol denote electronic quantum numbers; of which n is the principal quantum number, L denotes the orbital angular momentum in spectroscopic notation (S, P, D, F...) and $J = L + S$ is the total electronic angular momentum including electron spin S. We have encountered J before in the description of magneto-optical trapping of a two-level atom in Sec. 2.1. ^{85}Rb has a nuclear angular momentum with value $I = 5/2$ leading to a hyperfine structure within the electronic energy levels and a total atomic angular momentum quantum number $F = J + I$. A graphical representation of the ^{85}Rb level structure with hyperfine splitting is shown in Fig. 2.2. The cooling and trapping scheme is operated between the $5^2\mathrm{S}_{1/2}$, $F = 3$ and $5^2\mathrm{P}_{3/2}$, $F' = 4$ levels by the *trapping laser*. Due to the finite bandwidth of the laser, the $5^2\mathrm{P}_{3/2}$, $F' = 3$ level can be excited off-resonance. This opens up the possibility of the electron decaying back to the $5^2\mathrm{S}_{1/2}$, $F = 2$ level, out of reach for the trapping laser. To keep the cooling transition populated one has to apply a *repumper* to continuously empty the $5^2\mathrm{S}_{1/2}$, $F = 2$ level. Characteristics of ^{85}Rb and the $\left(5^2\mathrm{S}_{1/2},\, F=3 \rightarrow 5^2\mathrm{P}_{3/2},\, F'=4\right)$ cooling transition are listed in Table 2.1.

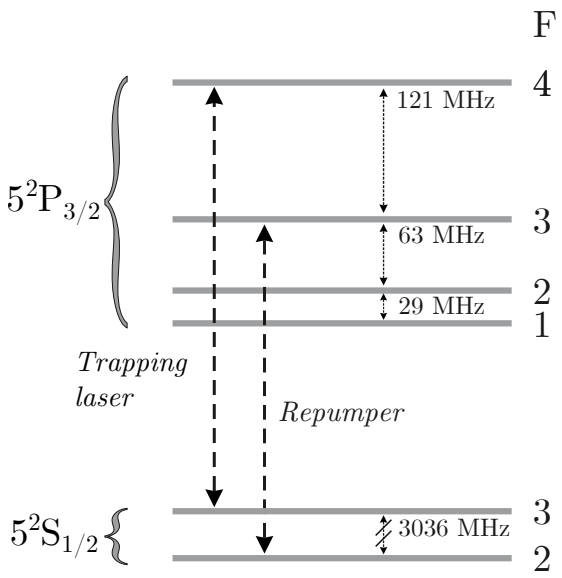

Figure 2.2: ^{85}Rb energy level diagram with hyperfine levels $5^2S_{1/2}$ and $5^2P_{3/2}$. Adapted from [17].

2.3 Grating Magneto-Optical Trap

Recently the Riis group at the University of Strathclyde, Glasgow, has developed the new concept of a grating magneto-optical trap [13]. In short the technique boils down to using the first order reflections of a grating chip, together with the incoming laser beam, to create a MOT in the overlap region of the aforementioned beams. Thereby, the number of laser beams required to build a MOT is reduced to 1. This simplifies alignment and operation compared to a conventional 6-beam MOT. A grating chip was obtained for this project and this section details the grating workings. All grating details in this section are from Ref. [13] unless stated otherwise. Measurements in Ref. [13] are performed for ^{87}Rb, which produces reliable data for estimates about our ^{85}Rb MOT.

In their research the Riis group has developed gratings with different diffraction structures. The grating used in this project is of the so called *linear* grating type, using a simple line pattern as the repeating entity. A SEM image of a section of the grating surface is shown in Fig. 2.3a. The diffraction pattern is etched in a silicon wafer. 825 lines per mm with a $50-50\%$ etched $-$ unetched duty cycle result in a grating period of $d = 1.21\,\mu$m. A 100 nm aluminum layer sputter coated on top of the diffraction structure serves as a reflector. The full chip measures $20 \times 20\,\text{mm}^2$ and consists of three sections with line patterns rotated 120° with respect to each other, see Fig. 2.3b. The trapping laser is coupled to an optical fiber and transported to the setup. Light exiting the fiber is collimated by a lens, and made circularly polarized by a $\lambda/4$-waveplate before hitting the grating at normal incidence, see Fig. 2.3c. Laser light diffracting off the grating chip obeys the well known Bragg diffraction condition:

$$n\lambda = d\sin(\theta)\,, \tag{2.9}$$

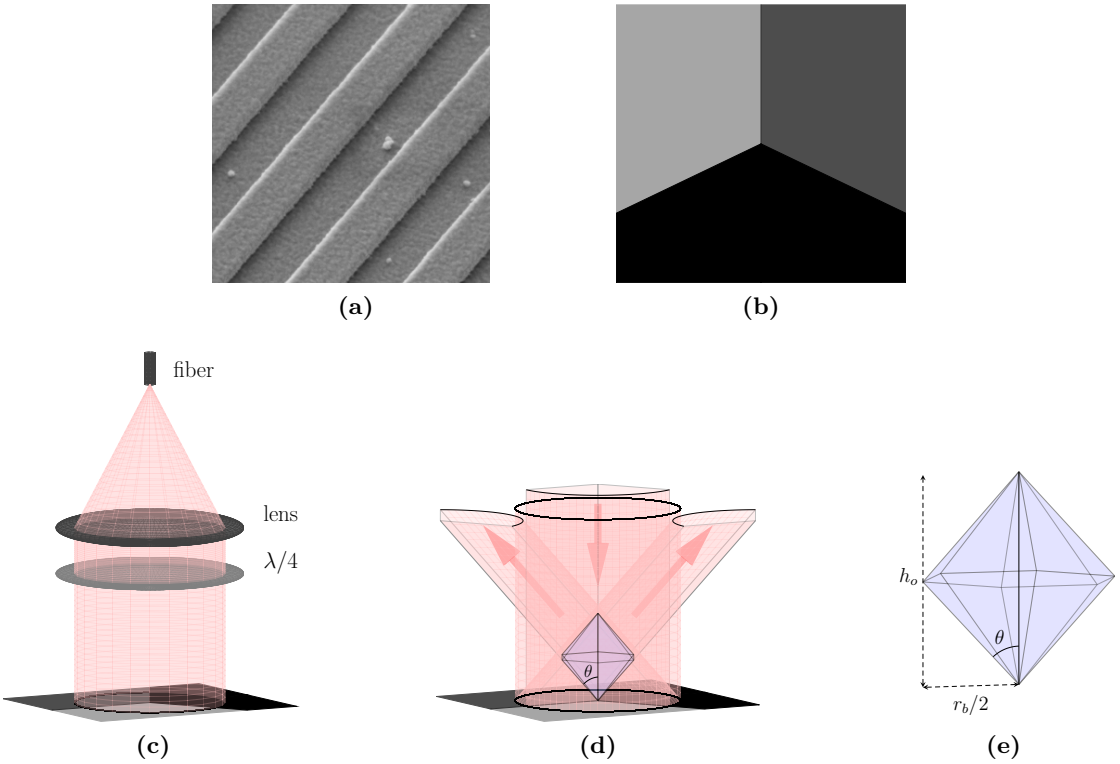

Figure 2.3: Images of the linear grating chip, illumination and overlap volume. **(a)** SEM image of a surface section. **(b)** Grating schematic. **(c)** Illumination schematic. **(d)** Diffracted orders $n = +1$ with overlap volume. **(e)** Overlap volume - detail. Images **(b)** through **(e)** from [12].

with n the diffraction order, d the period of the diffraction structure and θ the angle of diffraction with respect to the grating surface normal. For the trapping laser with $\lambda_\delta = 780\,\mathrm{nm}$ the first order diffracts at an angle $\theta = 40°$. The grating is optimized to couple laser power to the $n = \pm 1$ order. The etch depth of the line pattern is close to $\lambda_\delta/4 = 190\,\mathrm{nm}$ to suppress the 0^{th}-order reflection. Orders $n \geq 2$ are cut off as $n\lambda_\delta/d > 1$. The fraction incident laser power reflected into the first orders is $\sim 38\%$ [13].

Laser light in the +1-orders is directed towards the center of the grating. Together with the incident laser beam they form an overlap volume above the chip, see Fig. 2.3d. Atoms in the overlap volume are cooled in three dimensions and can be captured to form a MOT. For a trapping beam with circular cross section the overlap volume can be approximated by a hexagonal bipyramid. The height h_o of the bipyramid is given by:

$$h_o = \frac{r_b}{\tan(\theta)}, \tag{2.10}$$

with r_b the $1/e^2$ radius of the laser beam. The related $1/e^2$ overlap volume V_o is given by:

$$V_o = \frac{\sqrt{3}}{8}\frac{r_b^3}{\tan(\theta)}. \tag{2.11}$$

An schematic view of the bipyramid with relevant dimensions and angles is given in Fig. 2.3e. In our setup we work with a trapping beam with a $r_b = 11.25\,\mathrm{mm}$ radius, only limited by the use of 1 inch optics. With this beam $h_o = 13.4\,\mathrm{mm}$ and $V_o \approx 370\,\mathrm{mm}^3$ for our grating. As we want to create a MOT in the interior of a microwave cavity, h_o is a natural minimum for the cavity height. In these conditions $2r_b$ is bigger than the grating dimensions, hence part of the beam does not contribute to the overlap volume. However, as Eq. 2.11 is an underestimation of the actual overlap volume that can only be computed numerically, $V_o \approx 370\,\mathrm{mm}^3$ still is a good approximation.

The MOT atom number N_a is an important intermediate parameter influencing the MCRS signal. Hence N_a is maximized and estimates about the MOT characteristics are made in the remainder of this section. The MOT position can be controlled by manipulating the location of the zero crossing of the quadrupole magnetic field. To maximize N_a the MOT is centered in the overlap volume. The atom number scales with the overlap volume. This can be understood as $V_o^{1/3}$ is a measure for the distance over which atoms can be cooled and trapped from the hot background gas, the 'stopping distance'. The larger the stopping distance, the larger the fraction of hot background atoms that can be trapped. An empirical study shows the grating MOT follows the approximate scaling law $N_a \propto V_o^{1.2}$, just like a regular 6 beam MOT of similar overlap volume [13]. For optimal conditions of trap laser intensity $I_\delta \approx 45\,\mathrm{mW/cm^2}$ and detuning $\delta \approx -2\Gamma$ the Riis group has reported they can trap $N_a = 2.0 \times 10^7$ atoms in a MOT with $V_o = 560\,\mathrm{mm}^3$ (data digitized with [19]). Hence we should be able to trap about $N_a \approx 1.2 \times 10^7$ atoms with our grating. Atoms in the trap form a ellipsoid of revolution with a Gaussian density profile according to Eq. 2.6. The RMS size of the distribution is split in a direction parallel ($\sigma_\parallel$) and perpendicular ($\sigma_\perp$) to the plane of the grating with $\sigma_\perp/\sigma_\parallel = 0.7$. At these optimal conditions $I_\delta \gg I_S$ hence the Doppler temperature

Table 2.2: Estimated MOT characteristics.

Quantity	Symbol	Value	
Atom number	N_a	1.2	$\times 10^7$
RMS size	$\sigma_\perp$	340	μm
	$\sigma_\parallel$	475	μm
Atom temperature	T_a	~ 1	mK

limit of Eq. 2.3 is not reached. The temperature of the trapped atoms is a few times the Doppler temperature, or about $\sim 1\,\mathrm{mK}$. Estimated MOT characteristics are listed in Table 2.2.

2.4 Ionization

To create a plasma, the MOT is ionized with a two-step photoionization scheme. The scheme is shown schematically in Fig. 2.4a and in the form of an energy level diagram in Fig. 2.4b. To reduce the complexity of first measurements, the trap laser is used to drive the excitation transition from the $5^2\mathrm{S}_{1/2}$ ground state to the $5^2\mathrm{P}_{3/2}$ excited state. The trap laser wavelength λ_δ is detuned from resonance and has polarization σ^+ (σ^- after reflection). The trap laser intensity is high enough to saturate the transition ($I_\delta \gg I_S$) over the full MOT. In the second step the excited atoms from the intermediate level are photoionized above the ionization threshold $E_0 = hc/\lambda_0$ by the linear polarized ionization laser pulse λ_I. Here E_0 denotes the threshold energy corresponing to a photon of wavelength λ_0, and h is the Planck constant. The excess energy of the ionization photon ΔE is given by:

$$\Delta E = hc\left(\frac{1}{\lambda_I} - \frac{1}{\lambda_0}\right), \tag{2.12}$$

with $\lambda_0 = 479.06\,\mathrm{nm}$ in ^{85}Rb [18]. The ionization process adds energy and momentum to the electrons and ions. Neglecting the initial kinetic energy of the atom, energy and momentum conservation yield:

$$\Delta E = \frac{p_e^2}{2m_e} + \frac{p_i^2}{2m_i}, \tag{2.13}$$

$$h\mathbf{k}_I = \mathbf{p}_e + \mathbf{p}_i, \tag{2.14}$$

where $\mathbf{k}_I$ is the wave vector of the ionization photon and m_e (m_i) , p_e (p_i) are the electron (ion) mass and momentum respectively. Since the momentum of the ionization photon is very small, $\mathbf{p}_e \approx -\mathbf{p}_i$. Now due to the large mass ratio of the ion and electron ($m_i/m_e \sim 10^5$) effectively all the excess photon energy is carried away by the electron in the form of kinetic energy E_e:

$$E_e = \frac{p_e^2}{2m_e} \approx \Delta E. \tag{2.15}$$

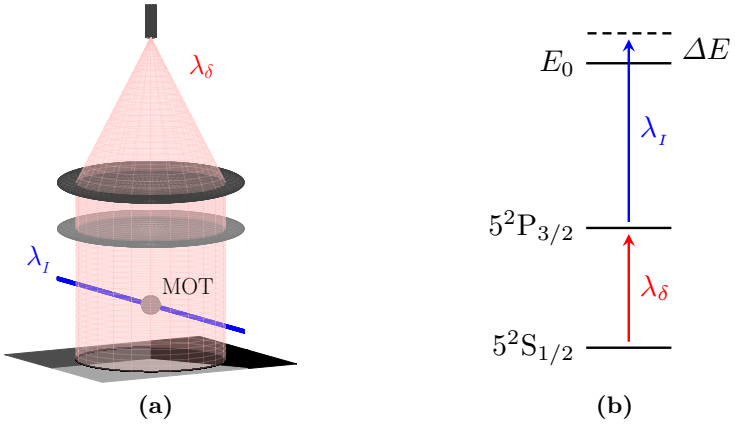

Figure 2.4: Two-step photoionization. The MOT atoms are excited by the trapping laser λ_δ, then ionized above the ionization threshold E_0 by the ionization laser λ_I. **(a)** Schematic. **(b)** Energy level diagram with excess energy ΔE. Adapted from [12].

Changing the wavelength of the ionization laser gives control over the initial electron kinetic energy E_e.

The chance of creating a free electron (or ion for that matter) is given by the single atom ionization probability $p_I(\mathbf{u})$:

$$p_I(\mathbf{u}) = p_* \left(1 - \exp\left(\frac{-\sigma_{\mathrm{PI}} \mathcal{F}_I(\mathbf{u})}{h\nu_I}\right)\right), \tag{2.16}$$

where $\mathbf{u} = (u, v)$ is a 2D Cartesian coordinate to be determined later, p_* is the probability of finding the atom in the excited state, σ_{PI} is the photoionization cross section from the excited state, $\nu_I = c/\lambda_I$ is the frequency of the ionization photon, and $\mathcal{F}_I$ is the fluence of the ionization laser pulse. Since the trap laser intensity is high enough to saturate the transition $p_* \approx 1/2$. In UCP experiments atoms are ionized in the near-threshold region with typically $\Delta E = 0.1 - 100\,\mathrm{meV}$. The minimum ΔE is limited by the bandwidth of the ionization laser. For pulsed dye lasers typically used in experiments $\Delta E_{\min} \sim 10\,\mu\mathrm{eV}$. However, in most UCP experiments up to now $\Delta E \geq 0.1\,\mathrm{meV}$ [11]. The photoionization cross section from the $5^2P_{3/2}$-state of rubidium measures $\sigma_{\mathrm{PI}} = 18.8 - 13.6 \times 10^{-22}\,\mathrm{m}^2$ for the range of excess photon energies $\Delta E = 0 - 106\,\mathrm{meV}$ [20]. The photoionization cross section is maximal at the threshold, and has a significant RMS measurement error of 16%.

The fluence of the ionization laser pulse $\mathcal{F}_I(\mathbf{u})$ is a 2D Gaussian distribution given by:

$$\mathcal{F}_I(\mathbf{u}) = \mathcal{F}_0 \exp\left(-\frac{u^2}{2\sigma_{Iu}^2} - \frac{v^2}{2\sigma_{Iv}^2}\right), \tag{2.17}$$

$$\mathcal{F}_0 = \frac{E_{\mathrm{pulse}}}{2\pi\sigma_{Iu}\sigma_{Iv}}.$$

With $\mathcal{F}_0$ the peak fluence in the center of the distribution and σ_{Iu}, σ_{Iv} its RMS size in the respective coordinate. E_{pulse} is the ionization pulse energy. By combining Equations 2.16 and 2.6, the initial charged particle distribution $n_j(\mathbf{x}, t=0)$ can be determined:

$$n_j(\mathbf{x}, 0) = p_I(\mathbf{u})\, n_a(\mathbf{x}), \tag{2.18}$$

where $j = e, i$ denotes the distribution for electrons and ions respectively. In the remainder of this report the subscript j will denote these species. Integration of Eq. 2.18 over 3D space yields the total number of free electrons and ions $N_e = N_i$ and the total ionization fraction $f_I = N_j/N_a$. For this proof-of-principle MCRS experiment N_e is maximized as it is one of the important parameters that determine whether we will have sufficient signal for detection.

The ionization laser at our disposal is a nanosecond pulsed dye laser currently capable of producing $\sim 300\,\mu$J pulses at the MOT position. Assuming $p_* = 1/2$, and optimizing the overlap of the circular ionization beam with the MOT distribution of Table 2.2, the maximal ionization fraction measures $f_I = 20 - 23\%$ for the range of excess photon energies $\Delta E = 0 - 106\,$meV. The expected maximum number of free electrons is about $N_e \approx 2 \times 10^6$ in a volume a little smaller than the MOT dimensions $\sigma_0 \sim 350\,\mu$m.

2.5 Plasma

As alluded to before, the defining characteristic of plasma as a medium originates from the availability of free charge carriers; electrons and ions. The Coulomb force causes long range interactions between particles, whereas in gaseous media interactions are dominated by close binary collisions. In this report we will restrict the word *plasma* to macroscopically neutral charged particle collections. In the case of our singly ionized plasma the electron density equates the ion density in the bulk of the medium.

Even the lightest ion, the proton, has a large mass as compared to the electron, i.e. $m_i/m_e > 10^3$. Hence electrons respond much quicker to potential fluctuations than the ions, effectively screening the ions from these fluctuations. The characteristic 1/e length scale for screening of potential fluctuations in a plasma is the famous Debye (screening) length λ_D:

$$\lambda_D = \sqrt{\frac{\varepsilon_0 k_B T_e}{n_e e^2}}, \tag{2.19}$$

where T_e is the electron temperature. This screening of potential fluctuations is the defining characteristic of plasma as a medium. To qualify a medium as a plasma, three conditions emerge from this definition [21]. Firstly: the length scale σ_0 of the plasma dimensions should be large compared to the Debye length, $\sigma_0 \gg \lambda_D$. For $\sigma_0 \leq \lambda_D$ screening is not effective and the medium loses it's characteristic property. Secondly: since the shielding effect is the result of the collective particle behavior, the Debye number $N_D \gg 1$, where:

$$N_D = \frac{4\pi}{3} n_e \lambda_D^3. \tag{2.20}$$

The Debye number is the average number of electrons to be found in a sphere with radius λ_D. If, on average, there is no electron to be found in a region spanned by the Debye length, there is no screening and one cannot speak of a plasma.

The typical excess ionization energy $\Delta E = 0.1 - 100\,\mathrm{meV}$ discussed in the previous section leads to an initial electron temperature $T_e = 1 - 1000\,\mathrm{K}$[1]. With a typical electron density $n_e \sim 10^{15}\,\mathrm{m}^{-3}$ in a volume with dimensions $\sigma_0 \sim 350\,\mu\mathrm{m}$, the first plasma condition ($\sigma_0 \gg \lambda_D$) is easily fulfilled. The second condition ($N_D \gg 1$) is not fulfilled in the low-end of the initial electron temperature range $T_e = 1 - 10\,\mathrm{K}$. With less than one electron in a Debeye sphere short-range interactions become important in describing the medium characteristics. However, as we will see later this section, the electron temperature in a freely expanding UCP rises to order $\sim 10\,\mathrm{K}$ in the first $\sim 100\,\mathrm{ns}$ after creation and the second plasma condition is fulfilled in the bulk of the medium.

With both of these conditions fulfilled, the charged particles exhibit collective behavior and a characteristic frequency arises, the plasma frequency:

$$\omega_{pj} = \sqrt{\frac{e^2 n_j}{\varepsilon_0 m_j}}. \tag{2.21}$$

The plasma frequency is the characteristic (angular) collision frequency for electron-electron (ω_{pe}), and ion-ion interactions (ω_{pi}). In general the electron plasma frequency is much higher than the ion plasma frequency ($\omega_{pe} \gg \omega_{pi}$) due to the aforementioned large mass ratio of the electrons and ions. Here the third plasma condition comes in. If the electron-neutral interactions (ω_{pn}) dominate electron-electron interactions ($\omega_{pn} > \omega_{pe}$), the electrons (and ions) will be in forced equilibrium with the neutrals and the medium can be treated as a neutral gas. Hence for the medium to be a plasma, $\omega_{pe} \gg \omega_{pn}$. This is the case down to a surprisingly low critical ionization fraction $f_{Ic} \ll 1$. For example in the case of helium with an electron temperature of $10^4\,\mathrm{K}$, it is found $f_{Ic} \simeq 10^{-7}$ [22]. Hence our ^{85}Rb plasma at a temperature $T \leq 10^3\,\mathrm{K}$ and a ionization fraction $f_I \sim 10^{-1}$ certainly behaves as a plasma.

The lifetime of a UCP can be divided in three distinctive phases related to the timescales of the inverse plasma frequency ω_{pj}^{-1}. These phases are depicted graphically in Fig. 2.5. From ionization at time $t = 0\,\mathrm{s}$ in order of increasing timescale [11]:

electron equilibration The first phase is characterized by electron-electron interactions at a typical timescale of $\omega_{pe}^{-1} \sim 1\,\mathrm{ns}$. Three processes develop in parallel.

- Directly after ionization the UCP is neutral. 'Fast' electrons escape over the first few periods of the electron plasma frequency and the remaining 'slow' ions turn the plasma slightly positively charged. The resulting potential well traps the remaining electrons. The initial stage of this process is finished after $\sim 10\,\mathrm{ns}$. Electrons

[1] Note directly after ionization one can not strictly speak of an electron temperature. Electron velocities are still uncorrelated and have not yet developed a Maxwellian velocity distribution. However, the electron kinetic energy is a good approximation for the thermal energy, $E_e \approx {}^3/_2 k_B T_e$. Details will be discussed later this section.

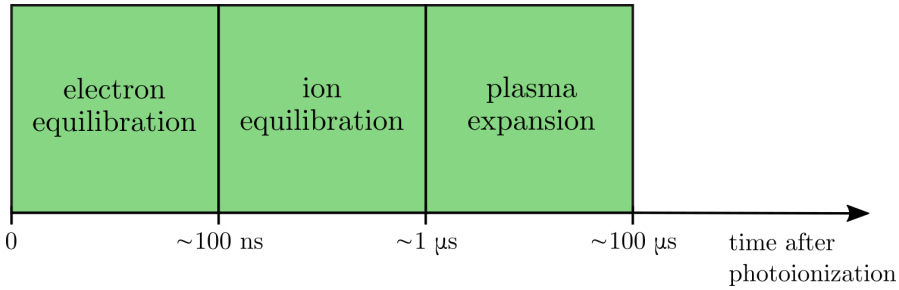

Figure 2.5: Typical UCP timescales. Adapted from [10].

will keep escaping the plasma at a much lower pace due to heating processes discussed later this section. This process is finished after about $\sim 1\,\mu$s. In our UCP with $N_e \approx 2 \times 10^6$, more than 90% of the electrons remain trapped for $\Delta E = 0.1 - 100\,\text{meV}$.

- Electrons thermalize through collisions among each other and establish a temperature, with $E_e \approx {}^3\!/_2 k_B T_e$. The range of excess photon energies $\Delta E = 0.1 - 100\,\text{meV}$ leads to a contribution to the electron temperature of $1 - 1000\,\text{K}$. The aforementioned heating processes provide another contribution. After about $\sim 100\,\text{ns}$ the electron temperature is well established.
- Ionization is a stochastic process, electrons are ionized at random positions with random directions of propagation. With the Coulomb force this creates a potential energy landscape for the electrons. Over the first few periods of the electron plasma frequency the potential energy is converted to thermal energy of the electrons. This process is called disorder-induced heating (DIH). DIH and other heating effects lead to a minimum electron temperature in the order of $\sim 10\,\text{K}$. At higher initial electron temperatures above 100 K, these contributions are of limited importance.

ion equilibration The second phase is characterized by ion-ion interactions at a typical timescale of $\omega_{pi}^{-1} \sim 100\,\text{ns}$. As the ion temperature follows the temperature of the MOT atoms, the ion velocity distribution is Maxwellian from the start. In our experiment $T_i \approx T_a \sim 1\,\text{mK}$. However, the ion positions are not yet correlated. DIH of the ions results in an increased ion temperature in the order of $\sim 1\,\text{K}$. During this process electrons are heated as well. Ion equilibration is finished after about $\sim 1\,\mu$s.

plasma expansion The third phase is characterized by plasma expansion. In typical UCP experiments the plasma simply expands into free space, cooling the electrons and ions adiabatically. Plasma lifetime is mostly determined by the electron temperature, as hot electrons increase the plasma expansion velocity. At long times $t \gg \omega_{pi}^{-1}$ the potential well holding the electrons together becomes shallow, allowing hot electrons to escape. A typical UCP lifetime is in the order of $100\,\mu$s.

Typically, UCP expansion is well described by the famous electronic Vlasov equation. For singly ionized ions:

$$\frac{\partial f_j}{\partial t} + \mathbf{v} \cdot \frac{\partial f_j}{\partial \mathbf{x}} - \frac{q_j}{m_j} \frac{\partial f_j}{\partial \mathbf{v}} \cdot \frac{\partial \varphi(\mathbf{x})}{\partial \mathbf{x}} = 0, \tag{2.22}$$

where $f_j(\mathbf{x}, \mathbf{v})$ is the one particle phase space distribution function for species j, q_j is the species' charge, and $\varphi(\mathbf{x})$ is the total mean-field potential determined by the Poisson equation:

$$\nabla^2 \varphi = \frac{e}{\varepsilon_0} (n_e - n_i). \tag{2.23}$$

The electronic Vlasov equation neglects particle collisions which results in the zero on the right-hand side of Eq. 2.22. This is a good approximation because of two conditions in our definition of a plasma. In the limit $N_{_D} \gg 1$ there are very many charged particles in a Debye sphere and collective particle interactions will dominate over close binary collisions. Hence we can get away with neglecting these collisions altogether and only the mean-field potential $\varphi(\mathbf{x})$ remains [22]. In the limit $\omega_{pe} \gg \omega_{pn}$ we can neglect collisions with neutrals as well.

A general, closed-form analytical solution of Eq. 2.22 cannot be given [10]. However, we can apply two additional assumptions: as recombination is negligible over a typical UCP lifetime, we can assume $\partial f_j / \partial t = 0$. Furthermore assuming quasineutrality ($n_e(\mathbf{x}) \approx n_i(\mathbf{x})$) leads to a whole set of solutions with a self-similar expansion. Starting with a Gaussian initial density distribution for the ions, leads to an expansion of the form:

$$n_j(\mathbf{x}, t) = n_{j0}(t) \exp\left(-\frac{x^2}{2\sigma_{jx}^2(t)} - \frac{y^2}{2\sigma_{jy}^2(t)} - \frac{z^2}{2\sigma_{jz}^2(t)} \right), \tag{2.24}$$

$$n_{j0}(t) = \frac{N_j}{\sqrt{2\pi}^3 \sigma_{jx}(t) \sigma_{jy}(t) \sigma_{jz}(t)},$$

$$\sigma_{jl}(t) = \sqrt{\sigma_{jl}^2(0) + v_{\exp}^2 t^2}, \qquad \text{for } l = x, y, z. \tag{2.24a}$$

Where $j = i$ and $v_{\exp}$ denotes the expansion velocity at long times $t \gg \omega_{pi}^{-1}$. This equation holds for $j = e$ as well as the electrons follow the ions during UCP expansion. The assumption of quasineutrality might seem counter intuitive as $\varphi(\mathbf{x}) \neq 0$ in Eq. 2.23. The details behind the derivation are subtle and can be found in Ref. [10]. Note $n_i(\mathbf{x}, 0)$ from Eq. 2.18 is not strictly Gaussian, but nearly. A Gaussian self-similar expansion describes experiments well in a UCP made from laser cooled metastable xenon [23]. Moreover, for $T_e \geq 50\,\mathrm{K}$ the expansion velocity is determined by the initial electron temperature:

$$v_{\exp} = \sqrt{\xi k_{_B} T_e / m_i}, \tag{2.25}$$

with $\xi = 0.9$ a fit constant [23]. At $\xi = 1$ the 1D expansion velocity is fully determined by the electron thermal energy, $m_i v_{\exp}^2 = k_{_B} T_e$.

This will be our model plasma for the proof-of-principle MCRS experiment on a UCP. By two-step photoionization of a ^{85}Rb MOT we create a UCP with a Gaussian density

distribution and a self-similar expansion. By setting the wavelength of the ionization laser to $\lambda_{50} = 477.86\,\text{nm}$ the electron temperature becomes $T_e = 50\,\text{K}$, see Eq. 2.12. At $T_e = 50\,\text{K}$ the plasma expansion velocity becomes predictable $v_{\text{exp}} \approx 66\,\text{m/s}$ while plasma lifetime is maximized and of order $\sim 100\,\mu\text{s}$. Note the expansion velocity might differ from the value expressed here as the $\xi = 0.9$ dependence is derived for a singly ionized Xe UCP. In this derivation the influence of the quadrupole magnetic field required for MOT operation is neglected as well. During expansion electrons are expected to gyrate around magnetic field lines, reducing the expansion velocity. The reduction in the transverse UCP expansion velocity has been studied experimentally in an homogeneous magnetic field [24]. As effects in a quadrupole magnetic field are not easily computed, this problem is left to be solved later. A reduction in the expansion velocity is expected.

2.6 Summary for Design

The idea is to create a UCP in a microwave cavity. The plan is to achieve this goal by two-step photoionization of a GMOT consisting of ^{85}Rb-atoms. For reliable MOT operation the vacuum system should be capable of pumping down the cavity to the UHV regime, or below $10^{-9}\,\text{mbar}$. As we will see in Ch. 3 the MCRS signal is dependent on the total number of electrons N_e in the plasma. To maximize N_e we need to maximize the number of atoms N_a in the MOT. The MOT atoms are trapped in the overlap volume V_o of the trapping beams. To maximize N_a the full overlap volume should fit in the cavity interior, leading to a minimum cavity height $h_o = 13.4\,\text{mm}$. The expected maximum number of trapped atoms is $N_a = 1.2 \times 10^7$ with a temperature $T_a \sim 1\,\text{mK}$ in a volume with a RMS size of roughly $\sigma \sim 400\,\mu\text{m}$. To maximize the MCRS measurement time, and have a simple, predictable model for the UCP expansion, the optimum electron temperature is $T_e = 50\,\text{K}$. This requires an ionization wavelength of $\lambda_{50} = 477.86\,\text{nm}$ and leads to a maximum ionization fraction of $f_I = 20\%$. The resulting UCP totals about $\sim 2 \times 10^6$ electrons in a volume a little smaller than the MOT dimensions $\sigma_0 \sim 350\,\mu\text{m}$. The UCP has an expansion velocity of $v_{\text{exp}} \approx 66\,\text{m/s}$ and an expected lifetime of $\sim 100\,\mu\text{s}$. An MCRS measurement resolution of $\sim 1\,\mu\text{s}$ should be fine to resolve the plasma expansion with good accuracy. All relevant parameters for the design of the experiment are summarized in Table 2.3.

Table 2.3: Summary of estimations for design.

MOT			
Atom number	N_a	1.2	$\times 10^7$
RMS size	$\sigma_\perp$	340	μm
	$\sigma_\parallel$	475	μm
Atom temperature	T_a	~ 1	mK
Ionization			
Ionization wavelength	λ_{50}	477.86	nm
Pulse energy	E_{pulse}	300	μJ
Total ionization fraction	f_I	20	%
UCP			
Number of electrons	N_e	2	$\times 10^6$
RMS size	σ_0	~ 350	μm
Electron temperature	T_e	50	K
Ion temperature	T_i	~ 1	K
Expansion velocity	v_{exp}	~ 66	m/s
Measurement			
Resolution	t_{min}	~ 1	μs
UCP lifetime	t_{max}	~ 100	μs
Cavity			
Minimum cavity height	h_{min}	13.4	mm
Background pressure	p	$< 10^{-9}$	mbar

3 Theory of Microwave Cavity Resonance Spectroscopy

The proof-of-principle microwave cavity resonance spectroscopy (MCRS) experiment on an ultracold plasma (UCP) that is the subject of this thesis, entails designing and building a microwave cavity, operating the grating magneto-optical trap (GMOT) in the cavity interior, ionization of the ultracold atom cloud (MOT) and tracking the evolution of the cavity resonance frequency as a function of time. To that end relevant theory for cavity design, characterization and operation is discussed in this chapter, together with the theoretical background of the MCRS technique.

This chapter is divided into three sections. Section 3.1 deals with microwave cavity theory. It discusses the resonant mode used in the MCRS experiment, and introduces the concept of the quality factor (Q-factor) of a cavity mode. The Q-factor is an important figure of merit for cavity performance as it determines the trade-off between two competing qualities of the MCRS measurement. The Q-factor determines the width of a mode resonance peak, and thus influences the *measurement* resolution of an MCRS measurement. A high Q-factor means a narrow resonance peak which is more easy to resolve with high accuracy. Conversely, build up of cavity fields in a high Q-factor cavity is slower, reducing the *temporal* resolution of the MCRS measurement. A trade-off needs to be found. The analytical expressions derived in this section will guide the considerations for cavity design in Ch. 4.

Section 3.2 deals with microwave cavity perturbation theory in two distinct cases. In the first case the theoretical background of the MCRS technique is discussed for a vanishingly small perturbation by a plasma. The second case deals with a perturbation by a spherical, high permittivity dielectric bead. Operating the GMOT in the cavity interior requires large holes in the cavity walls for optical access. Holes in the cavity walls alter the resonant geometry of the cavity in a non-trivial way and the cavity fields, resonance frequency and Q-factor will have to be determined through numerical simulation. The simulations of the cavity field profile can be verified experimentally with the aforementioned perturbation with a dielectric bead (bead-pull method). Again, as in the previous chapter, estimations important for cavity design are made throughout this chapter, and summarized in Sec. 3.3.

3.1 Cavity Theory

The plan is to design and conduct an MCRS experiment using a cylindrical 'pillbox' cavity geometry. Therefore it is convenient to introduce a cylindrical coordinate system next to the Cartesian coordinate system used in the rest of the setup, see Fig. 3.1.

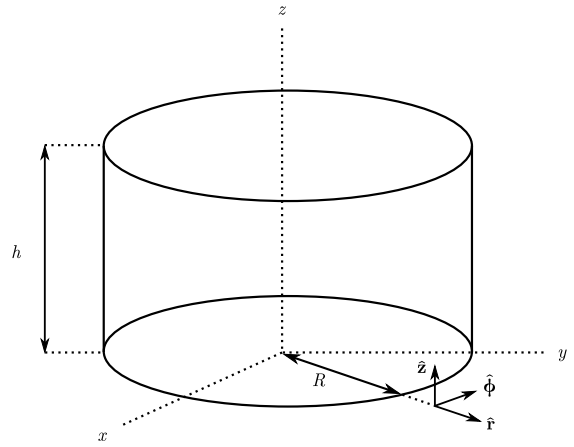

Figure 3.1: Pillbox cavity with definition of the Cartesian and cylindrical coordinate systems, where h is the cavity height and R the cavity radius. Adapted from [25].

The origin of the right-handed Cartesian coordinate system (x, y, z) is located on the axis of revolution (the z-axis) at the back plane of the cavity. The cylindrical coordinates (r, ϕ, z) are defined with respect to the same origin. In Fig. 3.1, h is the cavity height and the cavity radius is denoted by R.

Cavity fields in the cylindrical coordinate system are defined in the usual fashion. The electric field vector $\mathbf{E}$ has a total amplitude E with components E_r, E_ϕ and E_z in the respective directions. The same holds for the magnetic field vector $\mathbf{B}$:

$$\mathbf{E} = E_r\,\hat{\mathbf{r}} + E_\phi\,\hat{\boldsymbol{\phi}} + E_z\,\hat{\mathbf{z}} \qquad \text{and} \qquad E = |\mathbf{E}| = \sqrt{E_r^2 + E_\phi^2 + E_z^2}, \tag{3.1a}$$

$$\mathbf{B} = B_r\,\hat{\mathbf{r}} + B_\phi\,\hat{\boldsymbol{\phi}} + B_z\,\hat{\mathbf{z}} \qquad \text{and} \qquad B = |\mathbf{B}| = \sqrt{B_r^2 + B_\phi^2 + B_z^2}, \tag{3.1b}$$

here $\hat{\mathbf{r}}$, $\hat{\boldsymbol{\phi}}$ and $\hat{\mathbf{z}}$ denote the unit vectors in the respective directions. Full field expressions are obtained by multiplying the components in Eq. 3.1 with the time factor $\mathrm{e}^{\mathrm{i}\omega t}$ and taking the real part of the expression. In the time factor, ω denotes the angular frequency of the field and i is the imaginary unit. Note the phase difference between the electric and magnetic field is 90°. In the remainder of this thesis *angular* frequencies are denoted by ω and *ordinary* frequencies by f, keeping the same subscripts by convention. Obviously $\omega = 2\pi f$.

3.1.1 Resonant Mode

Solving Maxwell's equations with proper boundary conditions in a cylindrical cavity geometry leads to two sets of resonant solutions. The solutions are called 'modes', and divided in a transverse electric (TE) and transverse magnetic (TM) set. Historically microwave cavities have been developed in the context of beam manipulation (radar), with the z-axis being the direction of beam propagation. Hence the transverse direction is defined with respect to this axis. TE (TM) modes have no components of the electric

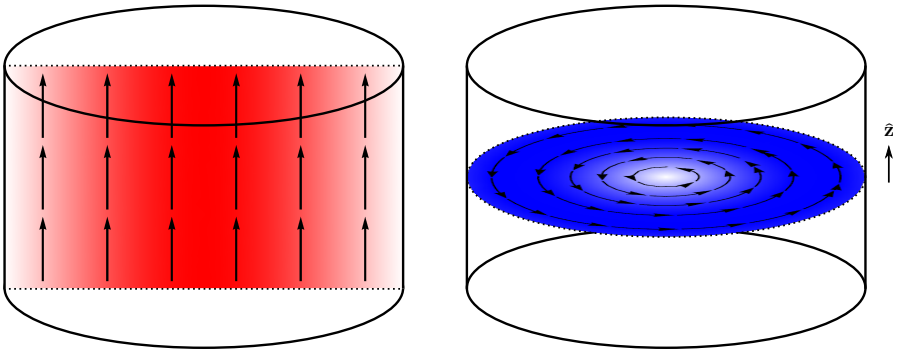

Figure 3.2: TM_{010} mode profiles. Left: E-field (red). Right: B-field (blue). Arrows follow field lines. Field amplitude in red and blue respectively. Adapted from [25].

(magnetic) field in the direction of propagation, only *transverse* components. To distinguish the individual modes, both sets are labeled with the indices m, n and p (TE_{mnp} and TM_{mnp}) related to the number of nodes in the ϕ, r and z direction respectively. For both sets of modes the indices m, n and p are represented by a natural number, while for TM modes $n \geq 1$ and for TE modes $p \geq 1$ *as well*.

In the proof-of-principle experiment we plan to use the TM_{010} mode. It is the fundamental mode for a pillbox cavity where the cavity diameter exceeds the cavity height ($2R > h$). In the TM_{010} mode only field components E_z and B_ϕ exist and both only depend on the radial coordinate. For an 'empty' (vacuum) cavity the field amplitudes are given by [26]:

$$E_z(r) = E_0 J_0\left(\frac{x_{01} r}{R}\right), \tag{3.2a}$$

$$B_\phi(r) = \sqrt{\varepsilon_0 \mu_0} E_0 J_1\left(\frac{x_{01} r}{R}\right), \tag{3.2b}$$

where x_{mn} is the n^{th} root of $J_m(x)$, the Bessel function of the first kind, ε_0 and μ_0 are the vacuum permittivity and permeability respectively, and E_0 is the peak electric field amplitude on the z-axis. Bessel functions are the harmonic functions of cylinder geometries and thus encountered here. A graphical representation of the TM_{010} mode profiles is plotted in Fig. 3.2. The electric field profile (red) is plotted on the left side of the figure, the magnetic field profile (blue) on the right. Arrows denote field lines, and field amplitude is color coded on a linear scale. Note the electric field has an antinode on the z-axis, where the magnetic field has a node.

The resonance frequency ω_0 of the TM_{010} mode only depends on the cavity radius and is given by:

$$\omega_0 = \frac{x_{01}}{R\sqrt{\varepsilon_0 \mu_0}}. \tag{3.3}$$

With $x_{01} \approx 2.405$, the TM_{010} mode in a cavity with a radius $R = 25\,\text{mm}$ has a resonance frequency of $f_0 = 4.6\,\text{GHz}$.

Thermal Stability

An MCRS experiment depends on measuring the resonance frequency shift of a microwave cavity. Other, uncontrolled parameters influencing the resonance frequency lead to a decrease in measurement accuracy. All solid materials expand and contract during temperature fluctuations, and so will the microwave cavity. Hence the resonance frequency of the TM_{010} mode in the microwave cavity is dependent on temperature T. The partial derivative of the resonance frequency in Eq. 3.3 with respect to temperature is given by:

$$\frac{\partial f_0}{\partial T} = \frac{-x_{01}}{2\pi\sqrt{\varepsilon_0\mu_0}}\frac{1}{R^2}\frac{dR}{dT} = -f_0\kappa_{_T}, \tag{3.4}$$

here $\kappa_{_T} = \frac{1}{R}\frac{dR}{dT}$ is the linear expansion coefficient of a solid material. For example, in the case of an aluminum cavity at room temperature $\kappa_{_T} = 23.1 \times 10^{-6}\,\mathrm{K}^{-1}$ [27] which leads to a change in resonance frequency of $\sim 100\,\mathrm{kHz}\cdot\mathrm{K}^{-1}$ for the TM_{010} mode in our 4.6 GHz model cavity.

3.1.2 Quality Factor

The quality factor (Q-factor) Q is an important figure of merit for microwave cavity performance. It is an important design criterion in the design of an MCRS experiment as we will see later this section. The Q-factor is the ratio of time-averaged energy stored in the cavity fields U to the energy lost *per cycle*. In terms of *time-averaged* energy loss P_{loss} this becomes [26]:

$$Q \equiv \omega_0 \frac{U}{P_{\mathrm{loss}}}. \tag{3.5}$$

With the cavity fields known analytically from the previous section, the Q-factor of the model cavity can be estimated. Integrating the time-averaged energy in the cavity fields of Eq. 3.2 over the cavity dimensions yields [26, 28]:

$$U = \frac{1}{4}\iiint_{\mathrm{cav}} \left(\varepsilon_0 |\mathbf{E}|^2 + \frac{1}{\mu_0}|\mathbf{B}|^2\right) \mathrm{d}^3\mathbf{x} = \frac{\pi\varepsilon_0}{2} E_0^2 J_1^2(x_{01})\, hR^2, \tag{3.6}$$

where $\mathrm{d}^3\mathbf{x}$ denotes a volume element. Cavity energy losses have different components discussed next.

Conductor Loss

Due to the finite conductivity of the cavity walls, electromagnetic fields impinging on the wall surface do not cancel directly on the interface, but penetrate the wall material. Over a characteristic length scale called the skin depth δ_s, the field amplitude decreases by a factor 1/e [26]:

$$\delta_s = \sqrt{\frac{2}{\mu_w\sigma_w\omega_0}}, \tag{3.7}$$

where μ_w and σ_w denote the permeability and conductivity of the wall material respectively. In the case of a 4.6 GHz aluminum cavity at room temperature $\mu_w \approx \mu_0$ and $\sigma_w = 3.56 \times 10^7$ S/m [29] leading to a skin depth of $\delta_s = 1.2\,\mu$m. As cavity fields penetrate the cavity wall, the wall *surface* resistance R_S is dependent on the wall thickness d [26]:

$$R_S^{-1} = \int_0^d \sigma_w \exp\left(-\frac{x}{\delta_s}\right) \mathrm{d}x. \tag{3.8}$$

For $d \to \infty$ the surface resistance has a limiting value given by $R_S = 1/(\sigma_w \delta_s)$. In the case of a thick walled 4.6 GHz aluminum cavity $R_S = 23\,\mathrm{m}\Omega$. A common design criterion is to assume the surface resistance has reached its final value after 5 skin depths of penetration into the wall material.

With the surface resistance defined, the time-averaged conductor loss in the cavity walls can be estimated. Time-varying magnetic fields impinging on the wall surface lead to a surface current $\mathbf{J} = \mu_0^{-1} \hat{\mathbf{n}} \times \mathbf{B}|_{\text{wall}}$. Here $\hat{\mathbf{n}}$ is the wall surface normal unit vector pointing to the cavity interior. Using the fields defined in Eq. 3.2 the time-averaged conductor loss in the cavity wall reads [26, 28]:

$$P_{\text{wall}} = \frac{R_S}{2} \iint\limits_{\text{wall}} \frac{1}{\mu_0^2} \left|\hat{\mathbf{n}} \times \mathbf{B}\right|^2 \mathrm{d}^2\mathbf{x} = R_S \frac{\pi \varepsilon_0}{\mu_0} E_0^2 J_1^2\left(x_{01}\right) R\left(R + h\right). \tag{3.9}$$

Combining the results of Eqs. 3.6 and 3.9, an analytical expression for the Q-factor of the TM_{010} mode due to conductor loss in the cavity walls can be derived:

$$Q_{\text{wall}} = \omega_0 \frac{U}{P_{\text{wall}}} = \frac{1}{\delta_s} \frac{\mu_0}{\mu_w} \frac{Rh}{R + h}. \tag{3.10}$$

Assuming the cavity height to be the height of the GMOT overlap volume derived in the previous chapter ($h = 13.4\,\mathrm{mm}$), the Q-factor due to conductor loss for the TM_{010} mode in a 4.6 GHz aluminum cavity is approximately $Q_{\text{wall}} \sim 7000$.

Radiation Loss

Operating the GMOT in the cavity interior requires holes in the cavity walls for optical access. From an energy point of view, electromagnetic fields in the cavity interior can 'leak' out of the resonant structure through holes in the cavity walls and lead to radiation loss. The hole placement, geometry and dimensions all will have an influence on the radiation loss –and thus the Q-factor– and are important considerations for cavity design.

Mathematically, a hole in the cavity wall can be viewed as a separate resonant structure, just as the microwave cavity itself. Assuming a hole with a circular cross section –which is convenient for laser access– the hole behaves as a cylindrical waveguide. Hole (waveguide) dimensions are defined in Fig. 3.3, where l_h and r_h are the hole length and radius, respectively. Note $\hat{\mathbf{z}}$ is the hole longitudinal axis. It is the direction of power flow from the cavity interior to the exterior. The hole longitudinal axis $\hat{\mathbf{z}}$ might differ from the cavity coordinate z, dependent on the hole placement on the cavity wall.

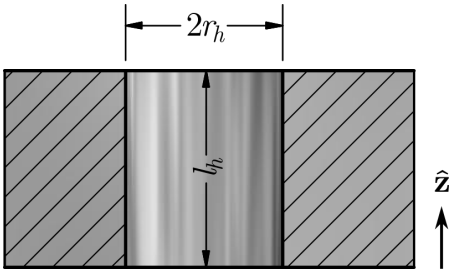

Figure 3.3: Hole in cavity wall for optical access, with radius r_h, length l_h and $\hat{\mathbf{z}}$ the direction of the longitudinal axis.

A cylindrical waveguide exhibits resonant modes TE_{mn} and TM_{mn}. These are the same modes as for a cylindrical cavity without the constraints in the longitudinal dimension along the z-axis. The dominant mode of a cylindrical waveguide is the TE_{11}-mode. Frequencies below the dominant mode cannot propagate in the waveguide and are *cut off*. Hence, in microwave theory, the dominant mode of a waveguide is called the *cutoff* frequency f_c. For vacuum cylindrical waveguides the cutoff frequency is given by [26]:

$$f_c = \frac{p_{11}^{'}}{2\pi r_h \sqrt{\varepsilon_0 \mu_0}}, \tag{3.11}$$

here $p_{mn}^{'}$ is the n^{th} root of the derivative of $J_m(x)$ with respect to x, and approximately amounts to $p_{11}^{'} = 1.841$.

Frequencies below the cutoff frequency cannot propagate in a waveguide. In the context of a microwave cavity with a hole in the cavity wall, cavity modes with resonant frequencies below the hole cutoff frequency ($f_0 < f_c$) will not propagate and reflect. In the case of total reflection there will be no radiation loss ($P_{\mathrm{hole}} \to 0$) and the associated Q-factor will approach infinity ($Q_{\mathrm{hole}} \to \infty$). The power loss in Eq. 3.5 is the sum of the individual components ($P_{\mathrm{cav}} = P_{\mathrm{wall}} + P_{\mathrm{hole}}$) and so:

$$Q_{\mathrm{cav}}^{-1} = Q_{\mathrm{wall}}^{-1} + Q_{\mathrm{hole}}^{-1}. \tag{3.12}$$

A hole totally reflecting a cavity mode will not significantly change the cavity Q-factor. The Q-factor of the TM_{010} mode in a 4.6 GHz aluminum cavity with totally reflecting holes for optical access is limited by conductor loss and remains approximately $Q_{\mathrm{cav}} \sim 7000$. In the context of an MCRS experiment, total reflection on the cavity holes is the desired situation as it achieves two things:

- The Q-factor of the cavity mode is preserved, maximizing MCRS measurement accuracy as we will see later this section.
- The cavity mode is isolated from the environment. Cavity fields will not propagate into the rest of the setup, nor will sources with frequency components $f < f_c$ in the rest of the setup contribute to the cavity fields. Hence we can be sure the measured MCRS signal is exclusively the result of cavity perturbation.

With different holes for optical access in the cavity walls, preserving the Q-factor of a cavity mode will depend on the hole with the largest radius. In the envisaged experiment, this will be the hole for the trapping laser. The trapping laser beam line uses 1 inch optics, so a hole radius $r_h = 13\,\text{mm}$ should be sufficient for optical access without limiting the trapping beam. A hole with a 13 mm radius has a cutoff frequency $f_c = 6.8\,\text{GHz}$, see Eq. 3.11. All cavity modes with $f_0 < f_c$ will not radiate into the rest of the setup and preserve their Q-factor. This is the case for the 4.6 GHz model cavity discussed in the previous section.

Note that reflection on a cavity hole is a resonant phenomenon, and cavity fields are not instantly reflected at the cavity–hole interface. Reflection will develop on a length scale in the order of the cutoff wavelength λ_c, where $\lambda_c = c/f_c$. Cavity holes with a length $l_h \ll \lambda_c$ will still radiate cavity fields. Likewise, even in the case of total reflection, cavity fields will penetrate the hole to some extent. Hence cavity holes contribute to the volume occupied by the cavity fields and change the geometry of the resonant structure. The resulting cavity mode profile and resonance frequency will deviate from the cavity fields discussed in Sec. 3.1.1, and are hard to compute analytically. During cavity design in Ch. 4 the mode profile, Q-factor and resonance frequency will be determined through numerical simulation.

External Loss

A microwave cavity cannot be operated in isolation. It will need a connection with the outside world for mode excitation and –in the case of an MCRS experiment– detection of the resonance frequency. The external part of the resonant circuit will invariably attribute to power loss, which is covered in the term *external* loss. To describe the external loss and how it influences the Q-factor of the cavity it is convenient to introduce some concepts from electronic circuit theory.

In electronic circuit theory the resistance, capacitance and inductance of a microwave cavity can be represented by a combination of idealized electrical components; resistors, capacitors and inductors. Components are connected by idealized, perfectly conducting wires into a lumped element model. The most basic lumped element model exhibiting resonant behavior is an RLC network, named after its three components. RLC networks exist in two topologies, a series network and a parallel network. Both can be used to describe the resonant behavior of a microwave cavity. In this thesis the arbitrary choice for a series RLC network is made.

A graphical representation of a series RLC network is shown in Fig. 3.4a. It consists of a resistor R_c, inductor L and capacitor C. In this model the resistor covers the losses while L and C represent the energy stored in the magnetic and electric cavity fields, respectively. An AC voltage of frequency ω applied across the terminals experiences an electrical impedance Z_{cav} given by:

$$Z_{\text{cav}} = R_c + \mathrm{i}\omega L + \frac{1}{\mathrm{i}\omega C}. \tag{3.13}$$

A series RLC network exhibits a resonance at a frequency $\omega_0 = 1/\sqrt{LC}$ and has a Q-factor $Q_{\text{cav}} = \omega_0 L/R_c$ [26, 30]. Note this definition for the resonance frequency and

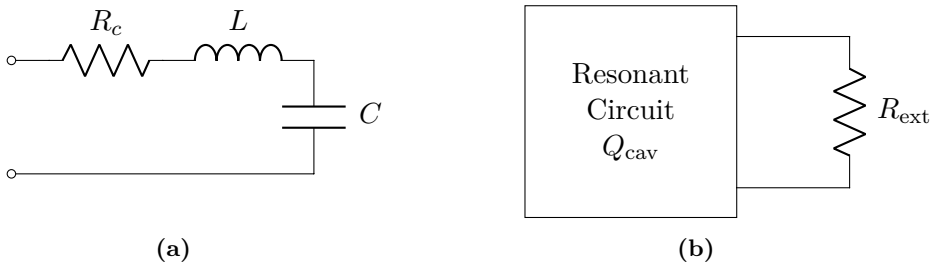

Figure 3.4: Lumped element networks representing the cavity electrical behavior **(a)** Series RLC network representing the microwave cavity itself with resistor R_c, inductor L and capacitor C. **(b)** Cavity circuit with Q-factor Q_{cav} connected to an external load R_{ext}.

Q-factor is strictly for a *series* RLC network. The cavity impedance Z_{cav} can be rewritten in terms of the Q-factor:

$$Z_{\text{cav}} = R_c + \mathrm{i}R_c Q_{\text{cav}} \left(\frac{\omega}{\omega_0} - \frac{\omega_0}{\omega} \right) \approx R_c \left(1 + 2\mathrm{i}Q_{\text{cav}} \frac{\Delta\omega}{\omega_0} \right), \tag{3.14}$$

where $\Delta\omega = \omega - \omega_0$ is the difference between the applied frequency and resonance frequency and we assume $\Delta\omega \ll \omega_0$ in the approximation. On resonance ($\omega = \omega_0$) the cavity impedance is purely real, and it reaches its minimum value of R_c.

For mode excitation, a microwave cavity is connected to a microwave generator matched to a transmission line. The transmission line has a characteristic impedance Z_0, where typically $Z_0 = 50\,\Omega$. Electromagnetic waves in a microwave network reflect on sudden changes in the electrical impedance. The fraction of the wave reflected on the interface is determined by the voltage reflection coefficient Γ_{V}. For electromagnetic waves propagating from a region of electrical impedance Z_1 to a region Z_2 it is defined as [26]:

$$\Gamma_{\text{V}} \equiv \frac{Z_2 - Z_1}{Z_2 + Z_1}. \tag{3.15}$$

On the cavity–transmission line interface, the voltage reflection coefficient is given by:

$$\Gamma_{\text{V}} = \frac{Z_{\text{cav}} - Z_0}{Z_{\text{cav}} + Z_0} = \frac{R_c - Z_0 + 2\mathrm{i}R_c Q_{\text{cav}} \Delta\omega/\omega_0}{R_c + Z_0 + 2\mathrm{i}R_c Q_{\text{cav}} \Delta\omega/\omega_0}. \tag{3.16}$$

During on-resonance excitation ($\omega = \omega_0$) reflection is minimal (zero) when the cavity impedance is matched to the transmission line $Z_{\text{cav}} = Z_0$. In all other cases, part of the voltage is reflected back into the transmission line and dissipated elsewhere in the network.

From the point of view of the microwave cavity, the microwave generator is seen as an external load. For a generator matched to the cavity transmission line, the load impedance Z_{gen} is purely real and $Z_{\text{gen}} = Z_0 = R_{\text{ext}}$, see Fig. 3.4b. To account for the

power dissipated *outside* of the cavity boundaries we can define an external Q-factor Q_{ext}. For a series network it is given by [26, 30]:

$$Q_{\text{ext}} = \frac{\omega_0 L}{R_{\text{ext}}} = \frac{\omega_0 L}{Z_0}. \tag{3.17}$$

The ratio of the cavity Q-factor to the external Q-factor is called the coupling coefficient β. It is the ratio of power loss in the network, with respect to power loss in the cavity:

$$\beta = \frac{Q_{\text{cav}}}{Q_{\text{ext}}} = \frac{P_{\text{ext}}}{P_{\text{cav}}} = \frac{Z_0}{R_c}. \tag{3.18}$$

Obviously $\beta > 0$. The range of possible coupling coefficients describes three distinct cases related to the main location of power dissipation. For $\beta < 1$ the cavity is *under*coupled, while for $\beta > 1$ the cavity is *over*coupled. In the case $\beta = 1$ the cavity is critically coupled and the power dissipation in the cavity is *matched* to the power dissipated in the external network. In practice coupling is achieved by connecting the transmission line to an antenna protruding the cavity interior. Details about how coupling is achieved in practice are discussed in Sec. 3.1.4. Note the coupling element is omitted from the discussion here, and in the lumped element models in Fig. 3.4. This is not a problem as this derivation boils down to an argument about power storage and dissipation. Power storage and dissipation in an antenna is negligible, as compared to the microwave cavity itself. The Q-factors of the cavity and the external network add reciprocally and form the loaded Q-factor of the microwave cavity $Q_{_L}$:

$$Q_{_L}^{-1} = Q_{\text{cav}}^{-1} + Q_{\text{ext}}^{-1} = (1+\beta)\, Q_{\text{cav}}^{-1}. \tag{3.19}$$

It is the Q-factor of the microwave cavity *loaded* by the external network. Contrastingly Q_{cav}, the Q-factor of the microwave cavity itself, is called the *unloaded* Q-factor and is purely a theoretical value. In an MCRS experiment the *loaded* Q-factor is of importance, during microwave cavity design we will optimize the *unloaded* Q-factor.

An MCRS experiment entails measurement of the shift in cavity resonance frequency due to a perturbation. Typically the resonance frequency is measured as a function of time. To determine the cavity resonance frequency one can measure the power reflected from the cavity $P_{\text{refl.}}$ as a function of frequency. Combining Eqs. 3.16 and 3.18 (after some algebra) the normalized reflected power is given by:

$$\frac{P_{\text{refl.}}}{P_{\text{inc.}}} = |\Gamma_{\text{V}}|^2 = 1 - \frac{4\beta}{(1+\beta)^2} \frac{1}{1 + 4\Delta\omega^2 Q_{_L}^2/\omega_0^2} = 1 - \mathcal{L}, \tag{3.20}$$

where the reflected power is normalized to the incoming power $P_{\text{inc.}}$, and $\mathcal{L}$ denotes a Lorentzian. The power reflected from the cavity describes a downward facing Lorentzian with a FWHM bandwidth BW:

$$\text{BW} = \frac{\omega_0}{Q_{_L}} = \frac{\omega_0\,(1+\beta)}{Q_{\text{cav}}}. \tag{3.21}$$

An example of the theoretical reflection curve of Eq. 3.20 for a critically coupled ($\beta = 1$) cavity mode with resonance frequency ω_0 is shown in Fig. 3.5. The bandwidth BW

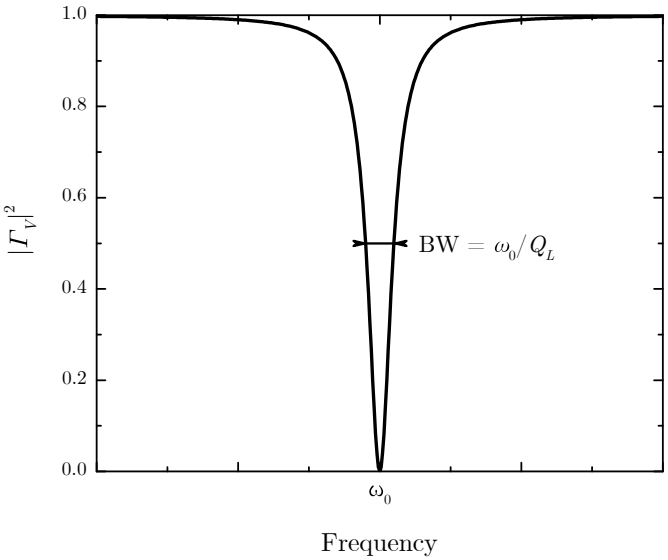

Figure 3.5: Normalized reflected power $|\Gamma_V|^2$ as a function of frequency for a critically coupled ($\beta = 1$) microwave cavity mode ω_0. The reflected power is described by a downward facing Lorentzian with an FWHM bandwidth BW $= Q_L/\omega_0$.

determines the *width* of the resonance peak (although facing downward, we will be using the term peak for convenience). Fitting the reflected power from the cavity with Eq. 3.20 one can determine the resonance frequency ω_0 of a cavity mode in an MCRS experiment.

With the resonance frequency $\omega_0 = 2\pi \times 4.6\,\text{GHz}$ and the unloaded Q-factor $Q_{\text{cav}} \sim 7000$ of the cavity mode estimated, the choice of the coupling factor β remains. Ultimately, the MCRS measurement sensitivity is determined by the maximum slope of the Lorentzian in Eq. 3.20. The maximum slope is found at the inflection point ($\partial^2 |\Gamma_V|^2 / \partial\omega^2 = 0$), and in terms of the unloaded Q-factor Q_{cav} it is given by:

$$\left.\frac{\partial |\Gamma_V|^2}{\partial \omega}\right|_{\text{max}} = \pm 3\sqrt{3}\frac{\beta}{(1+\beta)^2}\frac{Q_{\text{cav}}}{\omega_0}. \tag{3.22}$$

The maximum slope of the Lorentzian scales linear with the unloaded Q-factor Q_{cav}, and inversely with the resonance frequency ω_0 and bandwidth BW (see Eq. 3.21). It has an optimum for a critically coupled cavity ($\beta = 1$) and hence it is chosen to critically couple the microwave cavity to the external network in this proof-of-principle MCRS experiment. For critical coupling, the loaded Q-factor of the microwave cavity in the external network becomes $Q_L \sim 3500$.

3.1.3 Cavity Response Time

Build-up and decay of cavity fields in a microwave cavity takes a finite amount of time. In an MCRS experiment a time-dependent perturbation can be resolved up to a temporal resolution determined by the cavity response time. As a measure for the cavity response

time it is convenient to look at the cavity energy balance during transients in the power exciting the cavity mode.

In the switch-off transient the cavity is assumed to be excited on resonance ($\omega = \omega_0$) with power P_0, and operating in steady state. The power from the generator is *switched off* at $t = 0$:

$$P_{\text{inc.}} = \begin{cases} P_0 & t < 0 \\ 0 & t \geq 0 \end{cases}. \tag{3.23}$$

With no power coming from the generator, the time-averaged energy stored in the cavity fields U is discharged by the different loss components in P_{loss} discussed previously. The differential equation describing the switch-off transient reads [31]:

$$\frac{\mathrm{d}U}{\mathrm{d}t} = -P_{\text{loss}} = -\omega_0 \frac{U}{Q_{_L}}, \tag{3.24}$$

where we made use of Eq. 3.5 in rewriting P_{loss}. Integration of Eq. 3.24 with the boundary conditions in Eq. 3.23 yields:

$$U(t) = U_{\max} \mathrm{e}^{-t/\tau}, \tag{3.25}$$

where $U_{\max} = P_0 Q_{_L}/\omega_0$ is the time-averaged energy stored in the cavity fields during steady state, and $\tau = Q_{_L}/\omega_0$ is the cavity response time. During the switch-off transient the time-averaged energy stored in the cavity fields decays exponentially with time. The switch-on transient shows the same exponential behavior with a term $\left(1 - \mathrm{e}^{-\mathrm{t}/\tau}\right)$. If –during an MCRS experiment– the resonance frequency of a cavity mode changes instantly from ω_1 to ω_2 due to a perturbation of the cavity medium, frequency component ω_1 decays, and frequency component ω_2 builds up, exponentially in the cavity interior with a time factor τ. After 6 periods of the cavity response time the power from the cavity –as measured in reflection– has reached over 99.5% of its final value. For a 4.6 GHz cavity with a loaded Q-factor $Q_{_L} \sim 3500$ the cavity response time is $\tau \sim 120\,\text{ns}$. In our MCRS experiment the plasma behavior can be resolved with high accuracy up to a temporal resolution of $6\tau \sim 700\,\text{ns}$. A temporal resolution in the order of one microsecond is fine to resolve the ultracold plasma expansion.

Note the estimation of the loaded Q-factor is based on an idealized theoretical model. The Q-factor achieved in practice will be *lower*, and the associated cavity response time will be *faster*. Furthermore the model assumes full decay ($> 99.5\%$) of frequency component ω_1, and build up of component ω_2 as a measure for the time resolution in the experiment. Faster processes might still be detectable at the cost of signal-to-noise.

3.1.4 Coupling

Coupling of microwave power to a microwave cavity can be achieved in a variety of ways. In the low-power measurement application of the MCRS experiment envisaged in this thesis, power transmission on coaxial cables is the standard. A coaxial central conductor protruding from the wall into the cavity interior acts as an antenna and is a simple way of achieving coupling in practice. For these simple antennas two basic

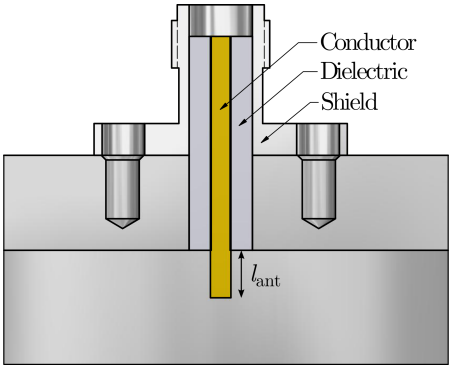

Figure 3.6: The central conductor of an SMA-type coaxial connector protrudes the cavity interior and acts as a linear antenna, with l_{ant} the antenna length.

geometries exist. In a loop antenna, currents on the central conductor terminated in a loop couple *magnetically* to the cavity fields. In a linear antenna, currents on the central conductor ending in a linear rod couple *electrically*. In this thesis the choice is made to use a linear antenna, as it is even easier to construct than a loop antenna. A linear antenna can be used in a 'set and forget' fashion.

A schematic representation of a linear antenna constructed from an SMA-type connector is shown in Fig. 3.6. The central conductor of the SMA connector is isolated from the outer conductor (shield) by dielectric material, usually Teflon. The conductor protrudes the cavity interior by a length l_{ant}. A general, exact analytical solution of antenna coupling to a microwave cavity cannot be given. However, for antenna lengths much smaller than the wavelength λ associated with the applied microwave power ($l_{\text{ant}} \ll \lambda$), a perturbative approach can be used [32, 33]. This approach gives insight into how coupling can be achieved and optimized in practice. In a perturbative approach a fractional wavelength linear antenna ($l_{\text{ant}} \ll \lambda$) can be approximated by an electric dipole $\mathbf{P}_{\text{ant}}$. Normalized to the applied microwave power, the dipole amplitude is dependent on the antenna length:

$$|\mathbf{P}_{\text{ant}}| \propto l_{\text{ant}}. \tag{3.26}$$

The dipole acts as a source for the cavity fields, and once the fields build up in the cavity interior, as a source for the fields radiated back into the transmission line. For a linear antenna excited near a cavity resonance ω_0 it can be shown that the *coupling strength* is proportional to the inner product between the electric dipole representing the coupler and the electric fields in the coupling region $\mathbf{E}_{\text{CR}}$ [25, 30]:

$$\text{Coupling strength} \propto \mathbf{P}_{\text{ant}} \cdot \mathbf{E}_{\text{CR}}, \tag{3.27}$$

where $\mathbf{E}_{\text{CR}}$ is the cavity electric field belonging to mode ω_0. This has consequences for antenna placement and tuning of the coupling factor β:

- For optimal coupling the linear antenna is aligned in parallel with the electric field in the coupling region ($\mathbf{P}_{\text{ant}} \parallel \mathbf{E}_{\text{CR}}$).

- Coupling is *stronger* in a high-field region of the excited mode, like in an antinode of the electric field profile.
- Coupling (and the coupling factor β) can be manipulated by tuning the length of the linear antenna, influencing the dipole amplitude $|\mathbf{P}_{\text{ant}}|$.

A longer antenna has more coupling strength, and an antenna with a given length couples more strongly in an anti-node of the electric field. At a given antenna position, the desired coupling factor can be achieved by reducing the length of an overlong antenna. With the correct orientation ($\mathbf{P}_{\text{ant}} \parallel \mathbf{E}_{\text{CR}}$) the antenna can be placed anywhere practical during cavity design. During tuning of the antenna length one can keep track of the achieved coupling factor by measuring the reflected power as a function of frequency with the use of a network analyzer. Fitting the measured values with Eq. 3.20 yields the coupling factor.

3.2 Cavity Perturbation

3.2.1 Plasma

In a microwave cavity, the cavity medium is perturbed by the introduction of free electrons, e.g. a plasma. This has implications for the resonance frequency of an excited cavity mode. In this section the resonance frequency shift of a microwave cavity due to a perturbation by a plasma is discussed in theory.

In the general case, consider a microwave cavity with a linear, isotropic cavity medium characterized by a permittivity ε and permeability μ. The unperturbed cavity fields are denoted by $\mathbf{E}$ and $\mathbf{H}$ belonging to mode ω. The cavity medium changes by a perturbation in the medium permittivity and/or permeability. In the new situation the medium permittivity is given by $\varepsilon + \Delta\varepsilon$, and the medium permeability by $\mu + \Delta\mu$. The cavity fields, and mode resonance frequency, are perturbed and denoted by $\mathbf{E}_p$, $\mathbf{H}_p$ and ω_p respectively. Plugging the new situation into Maxwell's equations and comparing it to the unperturbed case yields [6, 34]:

$$\frac{\omega_p - \omega}{\omega_p} = -\frac{\iiint_{\text{cav}} (\Delta\varepsilon \mathbf{E}_p \cdot \mathbf{E}^* + \Delta\mu \mathbf{H}_p \cdot \mathbf{H}^*)\, \mathrm{d}^3\mathbf{x}}{\iiint_{\text{cav}} (\varepsilon \mathbf{E}_p \cdot \mathbf{E}^* + \mu \mathbf{H}_p \cdot \mathbf{H}^*)\, \mathrm{d}^3\mathbf{x}}. \tag{3.28}$$

Here the asterisk (*) denotes a complex conjugate. Eq. 3.28 is an exact result and known as *Slater's perturbation theorem*. Its evaluation in practical situations poses a problem as $\mathbf{E}$ and $\mathbf{H}$ can be known analytically while $\mathbf{E}_p$ and $\mathbf{H}_p$ (in general) are not. In perturbation of an empty 'vacuum' cavity, $(\varepsilon, \mu, \omega)$ resort to their vacuum counterparts $(\varepsilon_0, \mu_0, \omega_{\text{vac}})$ and $\mathbf{E}$ and $\mathbf{H}$ are known from theory. For *vanishingly small* perturbations $(\Delta\varepsilon, \Delta\mu) \to 0$ we can approximate $\mathbf{E}_p$, $\mathbf{H}_p$ and ω_p with their unperturbed counterparts

E, **H** and ω_{vac} to arrive at:

$$\frac{\omega_p - \omega_{\mathrm{vac}}}{\omega_{\mathrm{vac}}} = -\frac{\iiint_{\mathrm{cav}} \left(\Delta\varepsilon E^2 + \Delta\mu H^2\right) \mathrm{d}^3\mathbf{x}}{\iiint_{\mathrm{cav}} \left(\varepsilon_0 E^2 + \mu_0 H^2\right) \mathrm{d}^3\mathbf{x}}, \tag{3.29}$$

which can be evaluated in the case of an experiment.

DC Field Free Case

In our proof-of-principle experiment we perturb the cavity medium (vacuum) with an ultracold plasma. In absence of external DC magnetic fields, the plasma is *unmagnetized* and $\Delta\mu = 0$ [5]. Eq. 3.29 resorts to:

$$\frac{\omega_p - \omega_{\mathrm{vac}}}{\omega_{\mathrm{vac}}} = -\frac{\iiint_{\mathrm{cav}} \Delta\varepsilon E^2 \, \mathrm{d}^3\mathbf{x}}{2\varepsilon_0 \iiint_{\mathrm{cav}} E^2 \, \mathrm{d}^3\mathbf{x}}, \tag{3.30}$$

where we have used the fact that $\iiint_{\mathrm{cav}} \varepsilon_0 E^2 \, \mathrm{d}^3\mathbf{x} = \iiint_{\mathrm{cav}} \mu_0 H^2 \, \mathrm{d}^3\mathbf{x}$ on resonance.

In general, a medium permittivity can be described relative to the vacuum permittivity $\varepsilon = \varepsilon_r \varepsilon_0$, where ε_r is the medium relative permittivity. For frequencies above the plasma frequency $\omega_p > \omega_{pe}$, in the collisionless plasma approximation, neglecting the effects of the (cold) ions, the relative plasma permittivity $\varepsilon_{r,p}$ is given by [5]:

$$\varepsilon_{r,p} = 1 - \frac{\omega_{pe}^2}{\omega_p^2}. \tag{3.31}$$

With Eq. 2.21 we can write the perturbation of the cavity medium permittivity $\Delta\varepsilon$ in terms of the plasma electron density n_e:

$$\Delta\varepsilon = -\varepsilon_0 \frac{\omega_{pe}^2}{\omega_p^2} = -\frac{n_e e^2}{m_e \omega_p^2}, \tag{3.32}$$

where $\Delta\varepsilon$ and n_e can be dependent on position and time. In the case of our ultracold model plasma $n_e(\mathbf{x}, t)$ is given by Eq. 2.24. With Eq. 3.32 we can define Eq. 3.30 in terms of the field-averaged electron density $\bar{n}_e$:

$$\bar{n}_e = \frac{2 m_e \varepsilon_0 \omega_p^2}{e^2} \frac{\omega_p - \omega_{\mathrm{vac}}}{\omega_{\mathrm{vac}}}. \tag{3.33}$$

Writing spatial dependencies explicitly, $\bar{n}_e$ itself is defined as:

$$\bar{n}_e \equiv \frac{\iiint_{\mathrm{cav}} n_e(\mathbf{x}) \, E^2(\mathbf{x}) \, \mathrm{d}^3\mathbf{x}}{\iiint_{\mathrm{cav}} E^2(\mathbf{x}) \, \mathrm{d}^3\mathbf{x}}. \tag{3.34}$$

The field-averaged electron density is the plasma electron density *weighted* by the square of the local electric field of the cavity mode. It is the electron density that –if spread over the full cavity volume– results in the same change in resonance frequency as the perturbation $n_e(\mathbf{x})$. The absolute value of $\bar{n}_e$ is *sensitive* to electron densities $n_e(\mathbf{x})$ located in an *antinode* of the electric field profile, and *insensitive* to electron densities located in a *node*.

Since the UCP in our MCRS experiment evolves with time $n_e(\mathbf{x}, t)$, so will the cavity resonance frequency. For interpretation of measurement results it is convenient to rewrite Eq. 3.33 in terms of the ordinary cavity frequency shift $\Delta f_p = f_p - f_{\mathrm{vac}}$. Writing time dependence explicitly, it is given by:

$$\Delta f_p(t) \approx \frac{e^2}{8\pi^2 \varepsilon_0 m_e f_{\mathrm{vac}}} \bar{n}_e(t), \tag{3.35}$$

where we have assumed $\Delta f_p \ll f_{\mathrm{vac}}$, and neglected higher orders of Δf_p.

In the context of our proof-of-principle experiment, Equations 3.34 and 3.35 have consequences for optimization of microwave cavity design, and more specifically, placement of the UCP within the cavity interior. The cavity frequency shift Δf_p is sensitive to electron densities located in an antinode of the electric field, which is located on the z-axis in the case of the TM_{010} mode see Fig. 3.2. Creating the UCP on the z-axis maximizes the MCRS measurement sensitivity and parameter space available in the experiment. The optimal attainable UCP with our GMOT setup amounts to $N_e \approx 2 \times 10^6$ electrons in a volume of typical dimensions $\sigma_0 \sim 350\,\mu\mathrm{m}$, see Table 2.3. Placing the UCP on the z-axis the maximum attainable frequency shift with the TM_{010} mode in our 4.6 GHz model cavity is $\Delta f_{\max} \sim 3\,\mathrm{kHz}$. This is a relative frequency shift of $\Delta f_{\max}/f_0 \sim 7 \times 10^{-7}$, very small indeed.

In practice, the cavity resonance frequency can be resolved with a finite resolution. This will impose a limit on the minimum frequency shift that can be measured in an MCRS experiment. The current record of our colleagues of the *EPG group* is to resolve the resonance frequency of a TM_{010} mode ($f_0 = 1.6\,\mathrm{GHz}$) in a microwave cavity ($Q_L = 490$) with an RMS error of $\sigma_{f_0} \sim 280\,\mathrm{Hz}$ [34]. Using a similar reflection based setup as our colleagues this would mean we should be able to measure a minimum relative frequency shift of $\Delta f_{\min}/f_0 = \sigma_{f_0}/f_0 \sim 2 \times 10^{-7}$. In absolute terms the minimum measurable frequency shift in our model cavity is about $\Delta f_{\min} \sim 800\,\mathrm{Hz}$. More information about the cavity and measurement setup of the *EPG group* can be found in Ref. [7].

Measuring a maximum relative frequency shift of $\Delta f_{\max}/f_0 \sim 7 \times 10^{-7}$, while the minimum measurable is $\Delta f_{\min}/f_0 \sim 2 \times 10^{-7}$ does not leave a lot of room for error. To be fair, we should be able to measure relative frequency shifts below $\sim 2 \times 10^{-7}$ as the estimated Q-factor of our model cavity is considerably higher than that of the *EPG group* ($\sim$ 3500 vs. 490). However, the Q-factor of our model cavity is a theoretical value and it remains to be seen whether it can be achieved in practice. Increasing the difference between the minimum and maximum relative frequency shift would give more room for error and expands the parameter space available for scanning the electron density in the experiment. Since the initial volume occupied by the UCP ($V_{\mathrm{ucp}} \sim 1\,\mathrm{mm}^3$) is much smaller than the cavity volume ($V_{\mathrm{cav}} \sim 25\,\mathrm{cm}^3$), the electric field is essentially

constant over the plasma. This means the maximum relative frequency shift $\Delta f_{\max}$ can be improved by increasing the fill factor $\mathrm{FF} = V_{\mathrm{ucp}}/V_{\mathrm{cav}}$ of the plasma in the microwave cavity, see Equations 3.34 and 3.35. In our situation the fill factor can be increased by reducing the cavity volume (height). Increasing the cavity fill factor is explored during cavity design in Ch. 4.

Temperature stability of the microwave cavity resonance frequency is another challenge. A temperature drift of $\Delta T \sim 30\,\mathrm{mK}$ would lead to the same change in resonance frequency as the maximum expected perturbation by the UCP ($\Delta f_{\max} \sim 3\,\mathrm{kHz}$), see Eq. 3.4. During experiments temperature drifts should be minimized, or known and corrected for.

DC Magnetic Field - MOT Coils

The previous analysis is held in absence of DC electromagnetic fields. This is not strictly the case as a DC magnetic quadrupole field (see Fig. 2.1) is used to trap ultracold atoms in the MOT. Presently the MOT coils cannot be switched off at a reasonable time scale below 1 ms due to the self induction of the coils and eddy currents in the setup. Note the ultracold atoms are trapped, and the UCP is created, in the zero crossing of the quadrupole. The influence of the DC magnetic field on microwave cavity perturbation is discussed in this section.

Slater's perturbation theorem (Eq. 3.28) is derived from Maxwell's equations. The addition of a DC magnetic field does not lead to new AC components in Maxwell's equations and the theorem remains valid. This leaves the influence of the DC magnetic field upon the plasma permittivity and permeability to be discussed.

Under the influence of a DC magnetic field a plasma becomes an anisotropic medium. Instead of an isotropic plasma permittivity ε_p the plasma permittivity is split in a direction parallel $\varepsilon_{\parallel}$, and a direction perpendicular $\varepsilon_{\perp}$ to the local magnetic field. Perpendicular to an uniform DC magnetic field $\mathbf{B}_{\mathrm{DC}}$ the plasma permittivity becomes [35]:

$$\varepsilon_{\perp} = \varepsilon_0 \left(1 - \frac{\omega_{pe}^2}{\omega^2 - \omega_{ce}^2}\right), \tag{3.36}$$

where ω_{ce} is the (angular) electron cyclotron frequency. It is the field free plasma permittivity with a correction term $-\omega_{ce}^2$ due to the electron gyration. The electron cyclotron frequency is defined to be strictly positive $\omega_{ce} > 0$ and given by $\omega_{ce} = eB_{\mathrm{DC}}/m_e$. Parallel to the magnetic field $\mathbf{B}_{\mathrm{DC}}$ the plasma permittivity is unchanged and remains [35]:

$$\varepsilon_{\parallel} = \varepsilon_0 \varepsilon_{r,p} = \varepsilon_0 \left(1 - \frac{\omega_{pe}^2}{\omega^2}\right), \tag{3.37}$$

as in Eq. 3.31. Note Eqs. 3.36 and 3.37 are valid in the collisionless plasma approximation and assume cold ions. Both are valid assumptions in a freely expanding UCP.

The DC magnetic field in the setup is produced by the previously mentioned MOT coils. The coils have a radius of 91 mm, consist of 196 turns and are capable of drawing 15 A of current [36]. Neglecting the quadrupole field topology, a MOT coil has a

maximum magnetic field of $B_{\max} \sim 20\,\mathrm{mT}$ on axis at the coil center. This would lead to a electron cyclotron frequency of $f_{ce} \sim 570\,\mathrm{MHz}$. Since $f_{ce} \ll f_0$ in our 4.6 GHz model cavity the permittivity perturbation perpendicular to the DC magnetic field ($\Delta\varepsilon_{\perp} = \varepsilon_{\perp} - \varepsilon_0$) would lead to a correction of about $\sim 1\%$ with respect to the scalar value in Eq. 3.32. During expansion the UCP will collide with the cavity wall before it reaches the location of the magnetic field maximum and the correction of Eq. 3.36 can be safely ignored our proof-of-principle experiment. This leaves the effect of the DC magnetic field on the plasma permeability perturbation to be discussed next.

The effect of the DC magnetic field on the plasma permeability perturbation $\Delta\mu$ remains unclear. The perturbation $\Delta\mu$ is expected to be small with respect to the permittivity perturbation $\Delta\varepsilon$ as in the field free case for two reasons:

1. The permeability perturbation $\Delta\mu$ in Slater's perturbation theorem (Eq. 3.28) is the permeability perturbation due to the *AC fields* of the cavity mode or $\Delta\mu_{(\mathrm{AC})}$. A DC magnetic field might lead to a DC plasma permeability $\mu_{\mathrm{DC}} \neq \mu_0$ and can only *indirectly* influence the cavity resonance frequency shift $\Delta\mu\,(\mu_{\mathrm{DC}})$.

2. The *Bohr–Van Leeuwen Theorem* states that [37]:

   > *In a constant magnetic field and in thermal equilibrium, the magnetization of an electron gas in the classical Drude–Lorentz model is identically zero.*

   Thermal equilibrium and the Drude–Lorentz model are good assumptions for the electrons in a freely expanding UCP. These are the same assumptions as used in the UCP expansion model in Sec. 2.5 and in the derivation of the (relative) plasma permittivity in Eq. 3.31. According to the Bohr–Van Leeuwen theorem the magnetization of a plasma in a DC magnetic field is identically zero (the plasma is unmagnetized) and the DC plasma permeability is unchanged $\mu_{\mathrm{DC}} = \mu_0$. Ref. [5] states that $\Delta\mu_{(\mathrm{AC})} = 0$ for *unmagnetized* plasmas ($\mu_{\mathrm{DC}} = \mu_0$) which suggests that $\Delta\mu_{(\mathrm{AC})} = 0$ in the case of a DC magnetic field *as well*.

For these two reasons the effect of the permeability perturbation $\Delta\mu$ on the cavity frequency shift Δf_p is neglected in the remainder of this thesis, and efforts are focused on realization of the experiment in practice. Note that the electric field of the TM_{010} mode has an antinode on the cavity z-axis where the magnetic field has a node, see Fig. 3.2. Creating the UCP on the cavity z-axis the initial cavity frequency shift due to the permittivity perturbation $\Delta f_p\,(\Delta\varepsilon)\,|_{t=0}$ will be *maximal*, where the initial shift due to the permeability perturbation $\Delta f_p\,(\Delta\mu)\,|_{t=0}$ will be *minimal*. If needed, the effect of the DC magnetic field can be examined by switching off the MOT coils in between MOT loading and ionization. With some effort the MOT coils can be switched off at timescales below 1 ms with counter-current compensation [38]. With a typical temperature $T_a \sim 1\,\mathrm{mK}$ of the trapped atoms in the magneto-optical trap, MOT expansion in 1 ms negligible and does not hinder experiments.

3.2.2 Dielectric Bead

The main goal of this thesis is to design a microwave cavity for a proof-of-principle MCRS experiment on a UCP. Creating the UCP in the cavity interior requires relatively large holes in the cavity walls for optical access. These holes change the cavity geometry and numerical simulation is required to determine the cavity Q-factor, resonance frequency and field profile during cavity design. To validate the simulations the cavity Q-factor and resonance frequency can be determined externally with the use of a network analyzer (see Sec. 3.1.2), however the cavity field profile cannot. The cavity electric field profile can be validated experimentally by perturbing the microwave cavity fields with a high permittivity dielectric bead. A summary of the theoretical background of this technique is described in this section.

In the case of perturbing the microwave cavity fields with a vanishingly small perturbation in the previous section we assume the electric field to be constant over the perturbation. In the case of perturbation with a high permittivity dielectric material this assumption does not hold. Due to the high permittivity, the internal electric field E_{int} in the dielectric material starts to deviate from the external applied field E of the cavity mode. This difference needs to be corrected for. In the case of a spherical object which is small with respect to the cavity dimensions, the internal electric field in a dielectric material with relative permittivity ε_r can be approximated by [5, 6, (Corrigendum)]:

$$E_{\text{int}} = \frac{3}{\varepsilon_r + 2} E. \tag{3.38}$$

Comparing an empty (vacuum) cavity with one containing a piece of dielectric material with permittivity $\varepsilon = \varepsilon_0 \varepsilon_r$ we can write for Slater's perturbation theorem (Eq. 3.28):

$$\frac{\omega_d - \omega_{\text{vac}}}{\omega_{\text{vac}}} = -\frac{\iiint_{\text{cav}} \Delta\varepsilon\left(\mathbf{x}\right) \mathbf{E}_d\left(\mathbf{x}\right) \cdot \mathbf{E}^*\left(\mathbf{x}\right) \mathrm{d}^3\mathbf{x}}{2\varepsilon_0 \iiint_{\text{cav}} E^2\left(\mathbf{x}\right) \mathrm{d}^3\mathbf{x}}, \tag{3.39}$$

where $\mathbf{E}_d = \mathbf{E}_{\text{int}}$ in the dielectric material and corresponds to the unperturbed cavity fields $\mathbf{E}$ elsewhere, ω_d is the resonance frequency of the perturbed cavity and spatial dependencies are written explicitly. Note we still assume the overall cavity perturbation to be small and approximate the perturbed cavity fields with their unperturbed counterparts as before. Evaluating the numerator of Eq. 3.39 for a spherical dielectric bead of volume V_d at position $\mathbf{x}_d$ yields:

$$\frac{\omega_d - \omega_{\text{vac}}}{\omega_{\text{vac}}} = -\frac{3\left(\varepsilon_r - 1\right)}{2\left(\varepsilon_r + 2\right)} \frac{V_d E^2\left(\mathbf{x}_d\right)}{\iiint_{\text{cav}} E^2\left(\mathbf{x}\right) \mathrm{d}^3\mathbf{x}}. \tag{3.40}$$

Defining the cavity frequency shift in the same way as in the previous section $\Delta f_d = \left(\omega_d - \omega_{\text{vac}}\right)/2\pi$ we arrive at the result of practical importance:

$$\Delta f_d\left(\mathbf{x}_d\right) \propto E^2\left(\mathbf{x}_d\right). \tag{3.41}$$

The cavity frequency shift due to the perturbation with a spherical dielectric bead scales with the square of the *local* electric field averaged over the bead volume. By pulling a dielectric bead attached to a string through the cavity interior, one can measure the electric field profile (bead-pull method). With the electric field profile known, the magnetic field profile follows from Maxwell's equations. To increase the measurement accuracy and resolution it is advantageous to use a *small* dielectric bead with a *high* permittivity. Note that determination of the absolute electric field profile with this technique is challenging. It requires absolute knowledge of the volume V_d and relative permittivity ε_r of the dielectric bead, which are both hard to determine with high accuracy. However, the *relative* electric field profile can be easily determined and is sufficient for verification of numerical simulations.

3.3 Summary for Design

In this chapter the relevant microwave cavity theory for the proof-of-principle MCRS experiment on a UCP is discussed in the context of a 4.6 GHz model cavity for the TM_{010} mode. The model cavity material is chosen to be aluminum (Al) and the cavity measures 13.4 mm in height and has a 25 mm radius. The skin depth δ_s in aluminum at 4.6 GHz is 1.2 μm which leads to a Q-factor of the microwave cavity of ~ 7000 due to conductor loss in the cavity walls. Holes in the cavity walls needed to operate the MOT in the cavity interior can lead to power loss and a deterioration of the cavity Q-factor. A hole with a circular cross section and a 13 mm radius has a cutoff frequency $f_c = 6.8$ GHz and should reflect the 4.6 GHz cavity fields. In the case of total reflection the unloaded cavity Q-factor is preserved and remains $Q_{\text{cav}} \sim 7000$. Drilling a 13 mm radius hole in a 25 mm radius cavity alters the resonant structure and associated mode profile, resonance frequency and Q-factor. These changes are hard to determine analytically and will have to be simulated numerically in Ch. 4. Simulated cavity fields can be verified experimentally with the bead-pull method discussed in Sec. 3.2.2. By critically coupling ($\beta = 1$) the microwave cavity to the external circuit –needed for mode excitation and detection of the MCRS signal– the loaded Q-factor of the cavity becomes $Q_{_L} \sim 3500$. A 4.6 GHz microwave cavity with $Q_{_L} \sim 3500$ has a 1/e cavity response time $\tau \sim 120$ ns, which is fine to resolve the ultracold plasma expansion. Creating the UCP on the central (z) axis of the microwave cavity maximizes the MCRS measurement sensitivity. For an optimal UCP with $N_e \approx 2 \times 10^6$ electrons in a volume with initial dimensions $\sigma_0 \sim 350\,\mu$m the maximum expected cavity frequency shift measures $\Delta f_{\text{max}} \sim 3$ kHz. Using a similar reflection based setup as our colleagues of the *EPG group* the expected minimum measurable frequency shift is $\Delta f_{\text{min}} \sim 800$ Hz, which gives little room for error in our proof-of-principle experiment. The maximum attainable frequency shift Δf_{max} can be optimized by increasing the fill factor in Ch. 4, i.e. by increasing the ratio of the UCP to cavity volume $V_{\text{ucp}}/V_{\text{cav}}$. The change in resonance frequency of the TM_{010} mode in a 4.6 GHz aluminum microwave cavity due to thermal expansion is $\partial f_0/\partial T \sim 100$ kHz. During experiments temperature fluctuations should be minimized, or known and corrected for. Relevant parameters for design of the experiment are

Table 3.1: Summary of estimations for microwave cavity design.

Model Cavity			
Material		Al	
Height	h	13.4	mm
Radius	R	25	mm
Mode		TM_{010}	
Resonance frequency	f_0	4.6	GHz
Thermal stability (Al – 4.6 GHz)	$\partial f_0/\partial T$	~ 100	kHz/K
Quality Factor			
Skin depth (Al – 4.6 GHz)	δ_s	1.2	μm
Hole cutoff frequency	f_c	6.8	GHz
Unloaded Q-factor	Q_{cav}	~ 7000	
Coupling factor	β	1	
Loaded Q-factor	$Q_{_L}$	~ 3500	
Cavity response time	τ	~ 120	ns
MCRS			
Maximum frequency shift	Δf_{max}	~ 3	kHz
– relative	$\Delta f_{\text{max}}/f_0$	~ 7	$\times 10^{-7}$
Measurable frequency shift	Δf_{min}	~ 800	Hz
– relative	$\Delta f_{\text{min}}/f_0$	~ 2	$\times 10^{-7}$
UCP volume (initial)	V_{ucp}	~ 1	mm^3
Cavity volume	V_{cav}	~ 25	cm^3

summarized in Table 3.1.

4 Microwave Cavity Design & Characterization

In this chapter microwave cavity design and characterization for the envisaged proof-of-principle microwave cavity resonance spectroscopy (MCRS) experiment is discussed. Section 4.1 deals with microwave cavity design, Q-factor optimization, and cavity commissioning and characterization. In Sec. 4.2 the design, commissioning and characterization of the parts needed to mount the cavity in the experimental setup is discussed.

4.1 Microwave Cavity

4.1.1 Cavity Design

A microwave cavity for the envisaged MCRS experiment was designed to meet the requirements discussed in the previous chapters. The cavity design is optimized for maximum MCRS signal and measurement resolution in three ways:

1. The UCP is created on the central cavity axis in an antinode of the TM_{010} cavity electric field profile. In this way the frequency shift Δf_p of the cavity mode is maximized for a given number of free electrons in the UCP.

2. The cavity volume is minimized to increase the fill-factor of the UCP in the cavity for the same reason as in point 1. A given number of free electrons perturbing a smaller cavity will result in a bigger frequency shift Δf_p.

3. The geometry and placement of the holes in the cavity walls, required for optical access are optimized to maximize the cavity Q-factor. A higher Q-factor increases the measurement resolution of the MCRS technique and lowers the minimum frequency shift $\Delta f_{\min}$ that can be measured in the experiment.

An exploded view of the cavity is shown in Fig. 4.1. The grating chip (1) used to create the GMOT in the cavity interior lies within a recess centered on the back wall of the cavity housing (2). The recess ensures the grating surface is parallel to the cavity back wall with the four semi-circle features at the grating corner points being a consequence of milling. Two miniaturized metal clamps hold the grating in place and prevent charging of the grating surface during experiments. Opposite to the grating is the cavity screw cap (3), with the big hole providing optical access for the trapping laser. When closed, the screw cap screws tight to a rim in the cavity housing, ensuring electrical contact. Four symmetrically placed smaller holes in the cavity housing (2) provide optical access for the ionization laser and the camera used to observe the MOT fluorescence in the

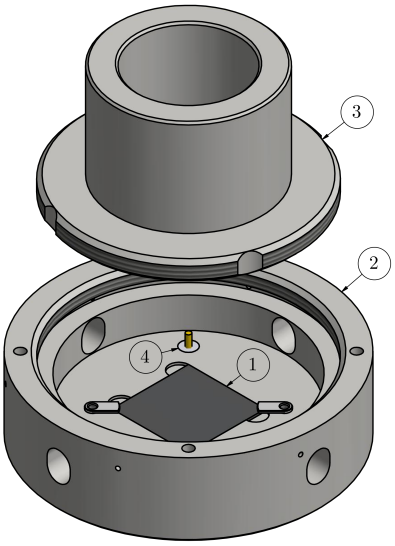

Figure 4.1: Exploded view of the microwave cavity. The grating (1) and microwave antenna (4) are positioned on the cavity back wall in the cavity housing (2), opposite to the cavity screw cap (3).

cavity interior. The microwave antenna (4) is placed on the back face of the cavity housing, out of view from all optical access holes. Aluminum is chosen as the cavity material for its vacuum compatibility, machinability and good electrical conductivity (high Q-factor). The clamps holding the grating are made of aluminum as well. Where possible all locations of air pockets are vented to shorten the pump-down time in the setup (virtual leak). For the same reason, there is a small hole directly behind the grating chip (not in the figure). This hole is useful when removing the grating from the cavity as well.

Cavity dimensions A cross section of the microwave cavity with dimensions is shown in Fig. 4.2. For clarity, the orientation of the trapping and ionization lasers is shown in Fig. 4.3.

The cavity diameter is minimized while still comfortably housing the $21 \times 21\,\mathrm{mm}^2$ grating (1) in the cavity interior. Note the effective grating surface measures only $20 \times 20\,\mathrm{mm}^2$. A diameter of 50 mm (radius $R = 25\,\mathrm{mm}$) leads to a resonance frequency $f_0 \sim 4.6\,\mathrm{GHz}$ of the TM_{010} mode (see Eq. 3.3). The access hole for the trapping laser (I) is located in the screw cap (3), opposite to the grating. The trapping laser beam path uses 1 inch optics, hence its access hole measures 26 mm in diameter (radius $r_h = 13\,\mathrm{mm}$) to prevent clipping. Hole I has a length l_h to be determined later in Sec. 4.1.2. The trapping laser incident on the grating results in an overlap volume in which ^{85}Rb atoms can be cooled and trapped. In Fig. 4.3 the boundary of the overlap volume is depicted by the dashed line. The overlap volume has a height of $h_o = 13.4\,\mathrm{mm}$ perpendicular to the grating, see Table 2.3. With an inner height of $h = 8\,\mathrm{mm}$ the cavity volume is

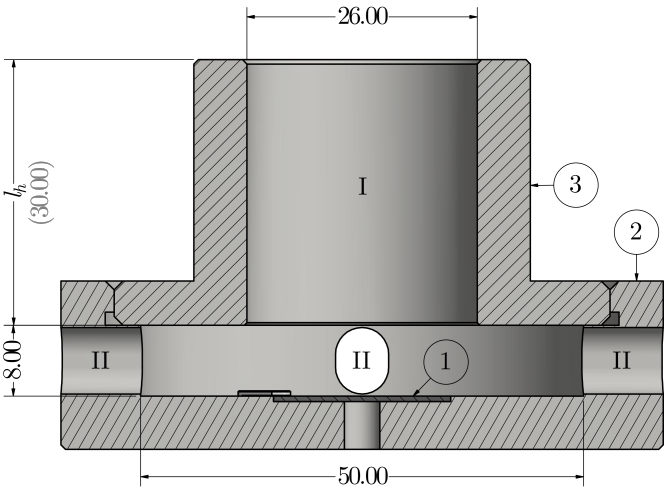

Figure 4.2: Microwave cavity cross section with dimensions (dimensions in mm). The grating (1) is centered on the back wall of the cavity housing (2), opposite to the cavity screw cap (3). Hole I located in the screw cap provides optical access for the trapping laser, the four holes (II) in the cavity housing provide optical access for the ionization laser and MOT camera.

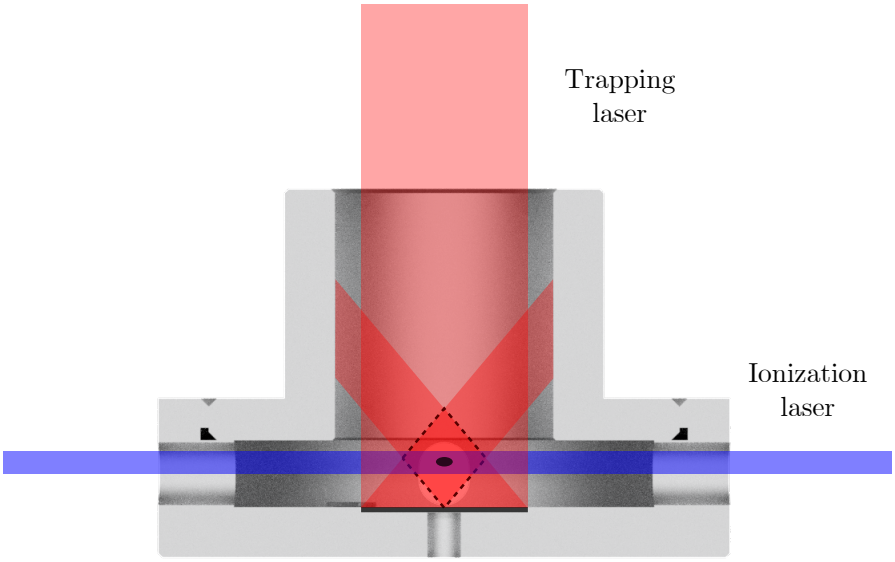

Figure 4.3: Microwave cavity cross section with orientation of the trapping and ionization lasers. The MOT (black ellipsoid) is centered in the overlap volume (boundaries dashed).

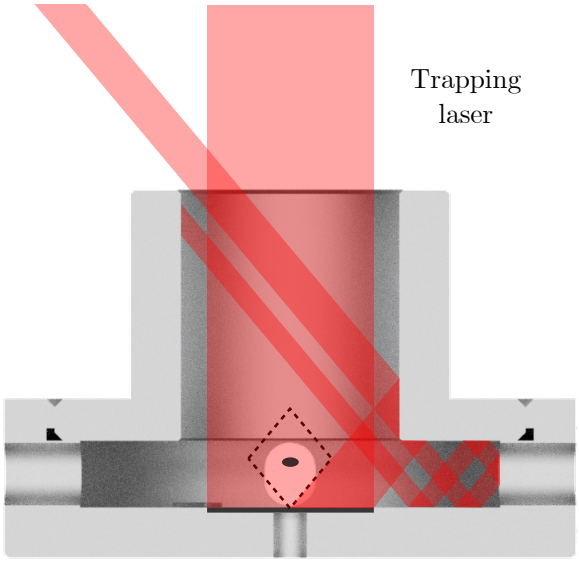

Figure 4.4: Microwave cavity cross section with the trapping laser light reflected in the negative (n = -1) grating order. The MOT (black ellipsoid) is centered in the overlap volume (dashed line) as in Fig. 4.3. About 30% of the trapping laser light reflected into the negative order leaves the cavity after multiple reflections in the cavity interior.

minimized (fill-factor maximized) while the center of the overlap volume remains visible for the MOT camera and ionization remains possible. The overlap volume protrudes into hole I and is not clipped by the cavity wall. The expected number of atoms in the MOT (black ellipsoid in Fig. 4.3) remains optimal. Lowering the cavity height has the added advantage that a higher percentage of the trapping laser light leaves the cavity through hole I directly. With a height of 8 mm about 70% of the light diffracted into the n = -1 order leaves the cavity through hole I directly, just as the light diffracted into the n = +1 order. This is illustrated in Fig. 4.4. The remaining 30% of trapping laser light in the negative grating order leaves the cavity through hole I after multiple reflections in the cavity interior. The reflections do not pass the MOT position and do not disturb the MOT balance. The four small holes (II) in the cavity housing (2) are 7.5 mm high and 6 mm wide with semi-circular top and bottom edges.

Influence of cavity holes Holes in the cavity walls change the resonant geometry of the microwave cavity. Care has to be taken to preserve the cavity Q-factor and numerical simulation is required to determine the cavity field profile.

The hole for the trapping laser (hole I) has a 13 mm radius which leads to a cut-off frequency $f_c = 6.8$ GHz (see Eq. 3.11). The hole will reflect cavity modes with frequencies $f < f_c$ over a length scale in the order of the cutoff wavelength $\lambda_c = c/f_c$ (order 10 mm). Hole I is located in an antinode of the (analytical) electric field profile of the TM_{010} mode (see Eq. 3.2 and Fig. 3.2), and coupling of the cavity fields is high. Care has to be taken to prevent radiation loss. The length l_h of hole I is varied in numerical simulations

in Sec. 4.1.2 to prevent radiation loss and consequently preserve the cavity Q-factor. Due to its size and location in a high coupling region, hole I will change the cavity field profile. Simulated cavity fields are discussed and verified in Sec. 4.1.3. The four access holes in the cavity housing (hole II) have a cut-off frequency above 250 GHz. Due to their small size, coupling of the cavity fields into the holes is minimal and the holes have a negligible influence on the cavity fields and Q-factor.

4.1.2 Quality Factor

To optimize the cavity Q-factor and determine the cavity fields, the cavity electromagnetic behavior is simulated in CST Microwave Studio [39]. Microwave Studio is a numerical simulation package, using a finite element method. Simulations are performed using the frequency domain solver and the reflection coefficient Γ_V at the antenna port is exported for analysis. To extract the cavity Q-factor, resonance frequency and coupling factor, the simulated reflection coefficient is fitted with a modified version of Eq. 3.20 including an offset α, infinitely far off resonance [25, 40]:

$$|\Gamma_V| = \sqrt{\frac{(\alpha-1)^2(\beta\delta_V)^2 + (\alpha+\beta-1)^2}{(\alpha+1)^2(\beta\delta_V)^2 + (\alpha+\beta+1)^2}}, \tag{4.1}$$

where $\beta = Q_{\text{cav}}/Q_{\text{ext}}$ is the coupling factor and δ_V is given by:

$$\delta_V \approx 2Q_{\text{ext}}\left(\frac{\omega-\omega_0}{\omega_0}\right). \tag{4.2}$$

To recapitulate, Q_{cav} is the unloaded Q-factor of the microwave cavity which is related to the loaded Q-factor Q_L of the cavity in the external network by $Q_L = Q_{\text{cav}}/(1+\beta)$, see Eq. 3.19, and ω_0 is the (angular) resonance frequency of the cavity mode. The offset α can be attributed to losses in the transmission line connecting the microwave cavity to the generator and will be of use in the next section.

In simulations the length l_h of the hole for the trapping laser (hole I in Fig. 4.2) is varied to minimize radiation loss and consequently preserve the Q-factor of the microwave cavity. First, an empty cavity is optimized. The complex structure of the clamps and grating chip are added later. As the optimization parameter the unloaded Q-factor Q_{cav} of the cavity is chosen to isolate the process from coupling effects of the antenna and the external circuit. In the remainder of this discussion, simulated Q-factor values are rounded to the nearest ten. Results of the Q-factor optimization are shown in Fig. 4.5. The unloaded Q-factor of the empty cavity (black squares) increases rapidly up to a hole length of 20 mm after which it levels off. At $l_h = 26$ mm the unloaded Q-factor effectively has reached its limiting value of about $Q_{\text{cav}} \sim 4000$. With a 4 mm safety margin, $l_h = 30$ mm is chosen as the trapping laser hole length, which results in a simulated unloaded Q-factor of the empty cavity $Q_{\text{cav}} = 3990$ and a resonance frequency $f_0 = 5.0$ GHz.

Simulations in Fig. 4.5 include the effects of surface roughness of the wall material. Milling of the microwave cavity out of a piece of solid aluminum leads to a typical RMS

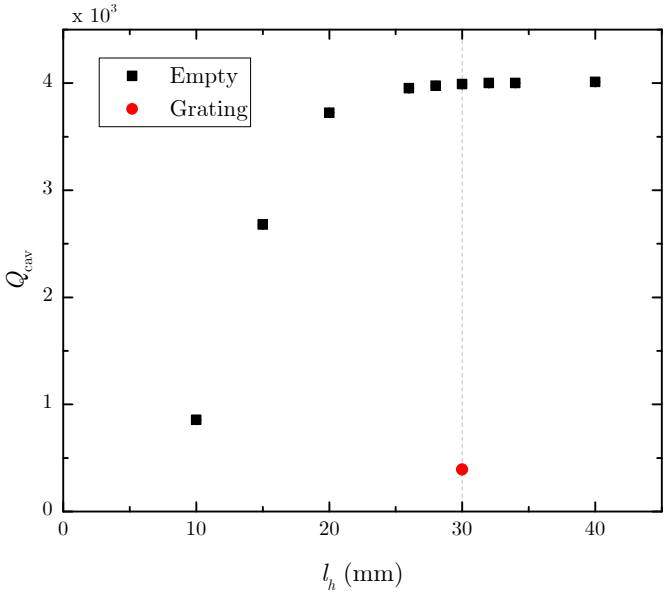

Figure 4.5: Simulated unloaded cavity Q-factor Q_{cav} as a function of hole length l_h. Squares - empty cavity, circle - cavity with grating and hole length $l_h = 30\,\text{mm}$.

surface roughness $R_q = 0.5\,\mu\text{m}$ [41]. A surface roughness of $0.5\,\mu\text{m}$ is within an order of magnitude of the skin depth at 5 GHz in aluminum ($\delta_s = 1.2\,\mu\text{m}$) and has a significant effect on the effective conductivity of the wall material. The effective conductivity of the cavity wall is reduced by $\sim 25\%$ to $\sigma_{\text{eff}} = 2.7 \times 10^7\,\text{S/m}$ [39]. The analytical unloaded Q-factor for the TM_{010} mode in a microwave cavity with radius $R = 25\,\text{mm}$, height $h = 8\,\text{mm}$ and an effective conductivity $\sigma_{\text{eff}} = 2.7 \times 10^7\,\text{S/m}$ is $Q_{\text{cav}} \sim 4250$ (Eq. 3.10). This value is very close to the simulated Q-factor of $Q_{\text{cav}} = 3990$. Introduction and optimization of the optical access holes in the cavity walls has a minimal effect on the Q-factor of the cavity TM_{010} mode and there is not much to be gained in further optimization.

Due to the introduction of the grating and clamps in the cavity interior the simulated unloaded Q-factor drops significantly to $Q_{\text{cav}} = 390$, see Fig. 4.5. The grating is simulated as a $21 \times 21\,\text{mm}$, 0.6 mm thick piece of silicon dielectric, with a 100 nm aluminum reflector on top. The reflector thickness is about four orders of magnitude smaller than any other length scale in the simulation, and so it is modeled as an infinitely thin (2D) metal sheet to prevent simulation artifacts. The frequency domain solver of CST Microwave Studio does not include dissipation in 2D metal sheets in the calculation of the electromagnetic field profile. It can either treat 2D metal sheets as fully transparent (all fields pass the material), or fully opaque (no fields pass the material). A 5.0 GHz electromagnetic wave propagating through 100 nm aluminum retains over 90% of its amplitude and so the grating reflector is modeled as a *transparent* 2D metal sheet. The simulation overestimates the field amplitude on the cavity wall behind the grating, and the resulting Q-factor will be a lower estimate of the expected value.

As 100 nm is only a fraction of the skin depth in aluminum at 5.0 GHz ($\delta_s = 1.2\,\mu$m), special care is taken to model the material properties of the grating reflector. The reflector material is modeled as a single layer, 100 nm thick aluminum *tabulated surface impedance* material (no surface roughness) to account for these effects. Due to its limited thickness the surface resistance (Eq. 3.8) of the grating reflector is about $R_s \sim 300\,\mathrm{m}\Omega$, much higher than the surface resistance of the aluminum cavity wall $R_s \sim 25\,\mathrm{m}\Omega$ (at 5.0 GHz). The increase in surface resistance leads to an increased power dissipation with respect to the empty cavity, and a lower Q-factor. The dissipation is further increased by concentration of surface currents on the reflector edges and clamps. To ensure physical contact between the clamps and grating, the grating surface is elevated $\sim 20\,\mu$m above the cavity back wall. As a consequence, the clamps are the only electric contacts between the cavity housing and grating reflector which results in the concentration of surface currents mentioned previously. When the clamps are removed in simulations the unloaded Q-factor increases to $Q_{\mathrm{cav}} = 740$. Note that the big effect of the increased reflector surface resistance on the cavity Q-factor was only discovered after commissioning of the microwave cavity. Microwave Studio assumes any structure in the simulation is more than five skin depths ($> 5\delta_s$) thick and assigns the full surface conductance (minimum surface resistance) of the material to the structure properties. Structures less than $5\delta_s$ thick can be simulated without warning. During cavity design the expected unloaded Q-factor of the microwave cavity was $Q_{\mathrm{cav}} = 2300$, a less severe drop. An idea to increase the cavity Q-factor will be discussed in Ch. 7.

4.1.3 Commissioning

A microwave cavity was commissioned using the design described in this section and the result is shown in Fig. 4.6. Fig. 4.6a shows the cavity interior (top view) with the grating and clamps installed in the cavity interior. Fig. 4.6b shows the cavity with the screw cap closed.

Quality Factor

An antenna was matched, and the voltage reflection coefficient measured as a function of frequency both for the empty cavity, and with the grating installed in the cavity interior. Measurement data of the network analyzer[1] is shown in Fig. 4.7 and fitted with Eq. 4.1. Results of the fitting procedure are compared to simulated values in Table 4.1.

Measurement results for the empty cavity are shown in Fig. 4.7a. The unloaded Q-factor measures $Q_{\mathrm{cav}} = 3848 \pm 8$, the coupling factor is $\beta = 1.04$ and the resonance frequency is $f_0 = 5.05\,\mathrm{GHz}$. Here, and in the remainder of this discussion only measurement errors exceeding the last digit are mentioned. With $Q_{\mathrm{cav}} = 3848 \pm 8$, the unloaded Q-factor of the microwave cavity is very close to the simulated value of $Q_{\mathrm{cav}} = 3990$ and it can be concluded that simulations provide an accurate description of reality. With the introduction of the grating into the cavity interior the unloaded Q-factor drops significantly. Due to the large change in Q-factor, a new antenna was tuned to effectively

[1] Rohde&Schwarz ZVH8

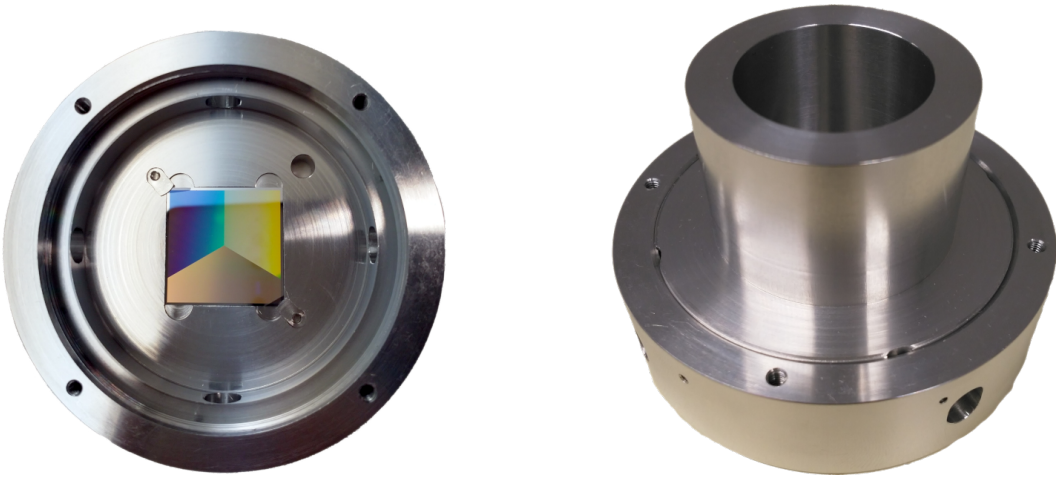

(a) **(b)**

Figure 4.6: Photos of the commissioned microwave cavity. **(a)** Cavity housing with clamps and grating. **(b)** Microwave cavity with screw cap.

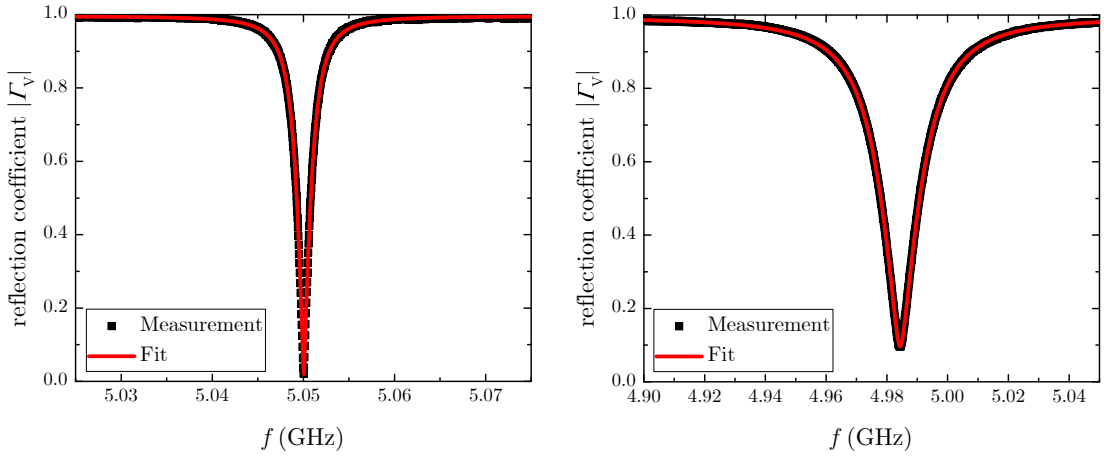

(a) **(b)**

Figure 4.7: Q-factor of the microwave cavity with fit for **(a)** an empty cavity, and **(b)** the cavity with grating. The fit results are compared to simulated values in Table 4.1.

Table 4.1: Simulated and measured unloaded Q-factor Q_{cav} of the microwave cavity. Simulated Q-factors are rounded to the nearest ten.

	Measurements			**Simulation**
	f_0 (GHz)	β	Q_{cav}	Q_{cav}
Empty	5.05	1.04	3848 ± 8	3990
Grating	4.98	1.21	491.0 ± 0.3	390

couple microwave power into the microwave cavity in the new situation. Measurement results for the cavity with grating are shown in Fig. 4.7b. The unloaded Q-factor measures $Q_{\mathrm{cav}} = 491.0 \pm 0.3$ with a coupling factor $\beta = 1.21$ and resonance frequency $f_0 = 4.98\,\mathrm{GHz}$. The cavity was left slightly overcoupled ($\beta > 1$) for reasons that will become clear in Sec. 4.2. With a coupling factor $\beta = 1.21$ about 1% of microwave power is reflected by the microwave cavity during on-resonance excitation, which is not a problem in the experiment. With $Q_{\mathrm{cav}} = 491.0 \pm 0.3$ the measured Q-factor exceeds the simulated value of $Q_{\mathrm{cav}} = 390$. This is not surprising as the grating reflector is modeled as a *transparent* metal sheet, leading to an increase in the simulated dissipation as discussed previously. Still, it is clear the increased surface resistance of the grating reflector is the main contribution to the drop in cavity Q-factor and the simulations are surprisingly accurate given the complexity of the grating and clamp structure. The validity of the simulation is investigated in more detail with the verification of the cavity fields discussed next.

Cavity Fields

The introduction of the grating into the microwave cavity interior, and the hole for the trapping laser, have a significant influence on the cavity field profile. The simulated field profile of the TM_{010} microwave cavity mode is discussed and verified in this section. As the envisaged MCRS experiment only depends on the (squared) cavity *electric* field profile, the magnetic field profile is left out of the discussion.

A plot of the simulated squared electric field profile E^2 in the cavity yz-plane is shown in Fig. 4.8. The field is normalized to $E^2\,(0, 0, 2\,\mathrm{mm})$ for easy comparison with the fields obtained in the verification process later this section. The orientation of the cavity axes is indicated in the top right of the figure and the cavity walls are depicted in black. The analytical cavity electric field profile of the TM_{010} mode has the shape of a Bessel function along the radial cavity dimension, see Eq. 3.2 and Fig. 3.2. Due to the introduction of the grating, and the hole for the trapping laser, the 'Bessel shape' is modified to a 'flat top' profile, as shown in Fig. 4.8. At the cavity front wall ($z = 8\,\mathrm{mm}$), the cavity electric field concentrates on the hole edge and forms 'spikes' in the radial profile. Along the cavity z-axis the electric field profile continually decreases for $z > 0$. This evolution of the radial cavity electric field profile is shown more clearly in Fig. 4.9d. In the figure, the radial (squared) electric field profile E^2 along the y-axis is plotted at three z-axis positions. At $z = 2\,\mathrm{mm}$ (black curve) the radial profile has the flat top structure as discussed earlier. At $z = 4\,\mathrm{mm}$ (red curve) the flat top structure is more pronounced, and at $z = 6\,\mathrm{mm}$ (blue curve) the spikes caused by the field concentration on the hole edge are clearly visible. The radial profiles have a slight asymmetry due to the antenna position in the $(x, -y)$ cavity quadrant and the field amplitude is slightly higher in the region close to the microwave antenna.

To verify the cavity field simulations, measurements of the cavity electric field have been performed using the bead-pull method discussed in Sec. 3.2.2. To that end a barium titanate ($BaTiO_3$) dielectric bead, attached to a piece of fishline, was pulled through the cavity interior along the cavity y-axis while manually recording the cavity

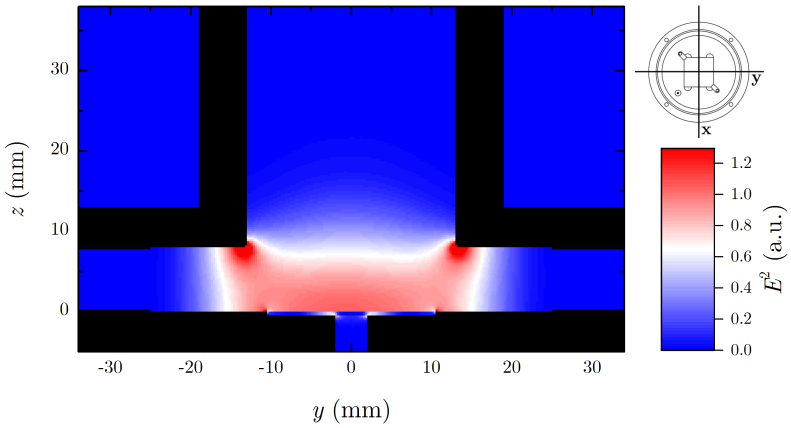

Figure 4.8: Squared electric field profile E^2 of the TM_{010} mode in the cavity yz-plane. Fields are normalized to $E^2\,(0, 0, 2\,\mathrm{mm})$ and cavity walls are depicted in black. Field amplitude corresponds to Fig. 4.9. Orientation of cavity axes is indicated in the top-right of the figure.

resonance frequency shift on a network analyzer. Barium titanate was chosen as the bead material for its very high relative permittivity $\varepsilon_r > 10^3$ at 5 GHz [42], increasing the measurement sensitivity of the technique. The dielectric bead measures a small 2 mm in diameter, which defines the spatial resolution of the measurement. The radial cavity electric field profile was recorded at three positions along the z-axis, at $z = 2$, 4 and 6 mm respectively, and measurement results are compared to simulations in Fig. 4.9a–c. All data is combined in Fig. 4.9d for an overview. Every data point in the figure is the average of three independent measurements. The RMS spread is calculated for every data point individually, and averaged over all data points in the figure to determine the error bars. In the figure, the relative (squared) electric field profile is normalized to $E^2\,(0, 0, 2\,\mathrm{mm})$ for easy comparison with simulations. The simulated field amplitudes correspond to Fig. 4.8, and the orientation of the cavity axes is indicated in the top-right of the figure.

In general, the data from the bead-pull method corresponds really well with simulations. At $z = 2\,\mathrm{mm}$ measurements deviate slightly from simulations near the grating location in the center of the figure. This is not surprising, considering the difficulty in accurately simulating the complicated structure of the grating reflector and clamps. At $z = 6\,\mathrm{mm}$ measurements and simulations deviate about 10% near the left hole edge at $y = -15\,\mathrm{mm}$. The deviation is already slightly visible in the data at $z = 4\,\mathrm{mm}$, and the source remains to be guessed. It could be that the cavity screw cap is slightly skewed in the cavity housing, locally prohibiting electrical contact. Or it could be the hole chamfer (flattened edge) is slightly wider at $y = -15\,\mathrm{mm}$. A chamfered hole edge is less sharp, and more chamfer leads to less concentration of the cavity electric field on the

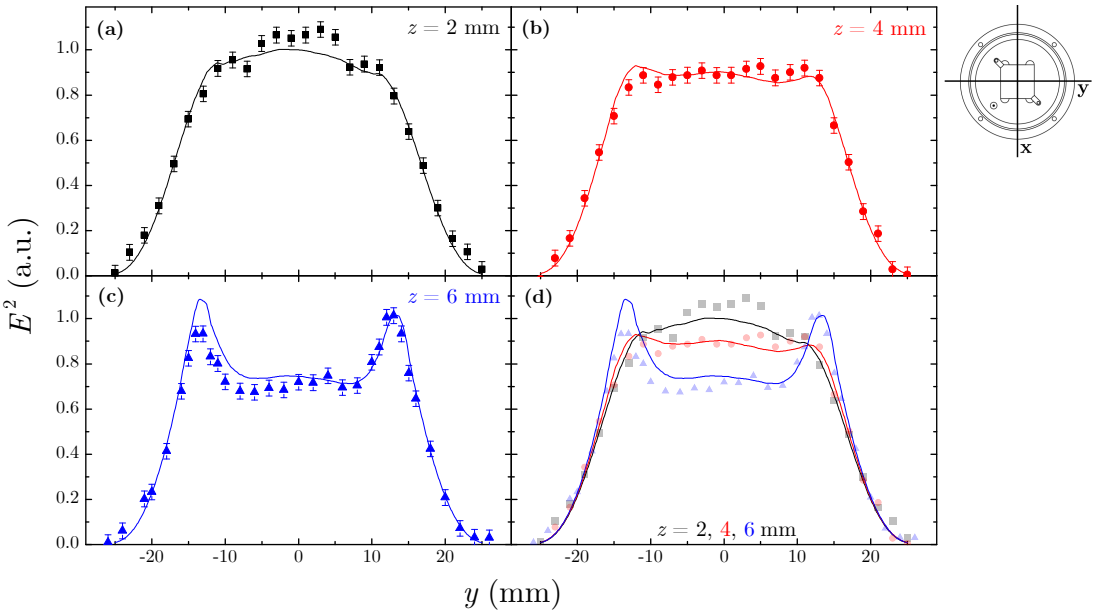

Figure 4.9: Squared cavity electric field profile E^2 of the TM_{010} mode on the cavity y-axis, comparison between bead-pull measurements (marks) and simulations (lines). Data at **(a)** $z = 2\,\mathrm{mm}$ (squares) **(b)** $z = 4\,\mathrm{mm}$ (circles) **(c)** $z = 6\,\mathrm{mm}$ (triangles) **(d)** all combined. Electric field amplitude is normalized to $E^2\,(0, 0, 2\,\mathrm{mm})$ and corresponds to Fig. 4.8. Orientation of cavity axes is indicated in the top-right of the figure.

hole edge. Either way, the deviation of the cavity fields will be encountered during UCP expansion and will lead to an error of a few percent in the cavity resonance frequency shift, as compared to simulated values. This is not a problem in the proof-of-principle experiment.

The MCRS measurement sensitivity is reduced due to the flat top profile of the cavity electric field. A UCP with $\sim 2 \times 10^6$ electrons centered on the cavity z-axis at $z = 5\,\mathrm{mm}$ results in a simulated maximum cavity resonance frequency shift $\Delta f_{\mathrm{max}} \sim 1.5\,\mathrm{kHz}$, about twice the minimum measurable frequency shift of $\Delta f_{\mathrm{min}} \sim 800\,\mathrm{Hz}$. This leaves little room for error, but could still be detectable.

4.2 Cavity in Setup

The envisaged MCRS experiment will be conducted within the boundaries of a shared setup for grating based cold atom experiments. In Section 4.2.1 the details of the shared setup are discussed, and Sec. 4.2.2 deals with the design and commissioning of the custom flange and parts needed to house the cavity within the setup.

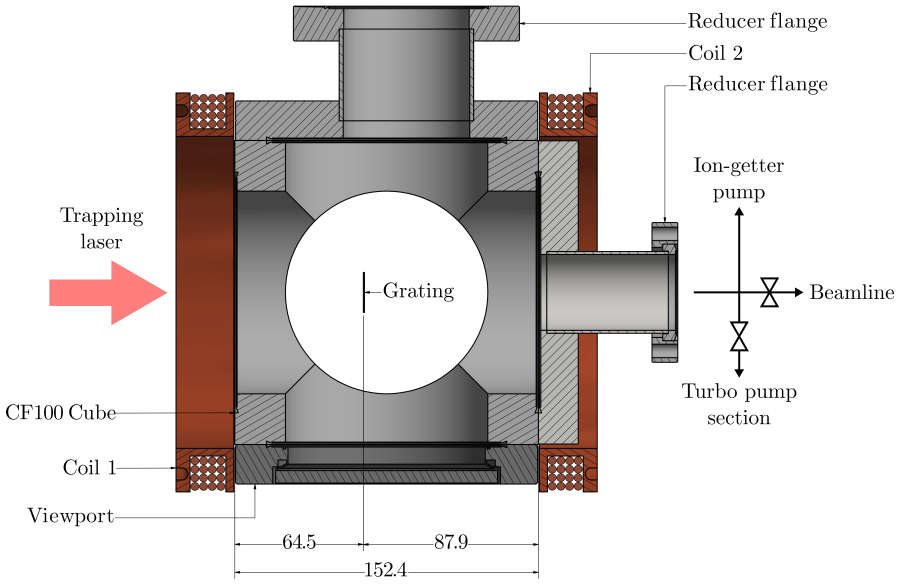

Figure 4.10: Cross sectional view of the shared setup for grating based cold atom experiments. The setup is based on a CF100 cube. Two coils outside the cube produce a magnetic quadrupole field required for MOT operation. The fixed grating position on the cube horizontal axis, at 64.5 mm from the left cube face allows for easy switching of experiments. Dimensions in mm.

4.2.1 Shared Setup

Our proof-of-principle MCRS experiment will be conducted within the boundaries of a shared setup for grating based cold atom experiments. A cross section of the setup is shown in Fig. 4.10. The grating chip is housed in a CF100 cube and positioned perpendicular to the trapping laser entering the cube along the center axis from the left of the figure. Sharing the grating position at 64.5 mm from the (left) cube face prevents realignment of the optical setup (lasers and cameras) and allows for easy switching of experiments. Two coils produce the magnetic quadrupole field required for MOT operation. The quadrupole zero crossing (MOT position) can be moved along the shared coil axis by changing the ratio of the currents driving the two coils. At the top face a CF100 to CF63 reducer flange connects the cube to the rubidium dispensers[2]. At the right face a CF100 to CF40 reducer flange connects the cube to the vacuum pump section and beamline. The beamline is used in other experiments conducted on this setup where a GMOT is used as an ultracold electron source. The beamline is not used in the experiment described in this thesis and its valve is kept closed permanently. The vacuum pump section consist of a Ion-getter pump[3] and a turbo pump section. The current drawn by the ion pump serves as a pressure gauge. Initial pump down of the setup is performed by the turbo pump section. At a few 10^{-8} mbar the ion pump is

[2]SAES Rb/NF/7/25 FT10-10
[3]SAES NEXTorr D 100-5

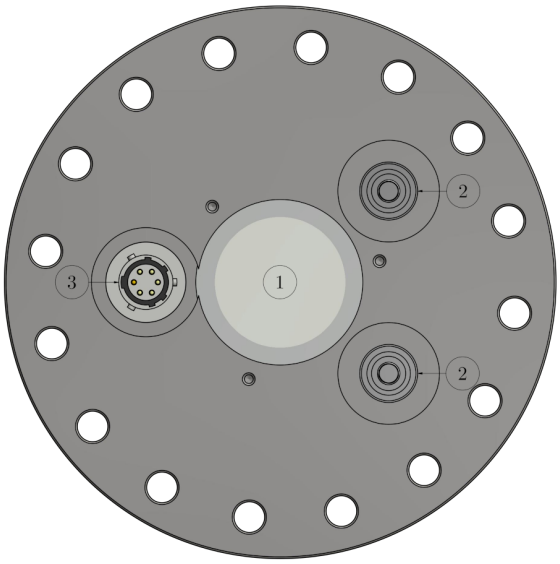

Figure 4.11: Custom CF100 flange with viewport (1), 2× 50 Ω SMA microwave feedthrough (2) and circular 6-pin electrical feedthrough (3).

sparked, the getter element is activated and the setup pumps down to the 10^{-10} mbar regime. The valve to the turbo pump section is closed and the setup is held at pressure by the ion-getter pump. During experiments the partial rubidium pressure in the cube is in the 10^{-9} mbar regime. The front, back and bottom face of the cube are covered by UV grade CF100 viewports allowing for maximal optical access. The ionization laser (not shown in the figure) propagates in a direction out-of-plane in the figure through the viewports at the front and back face of the cube. The viewport on the bottom face of the cube provides optical access to the excitation laser (not used in this experiment) and to the camera used for fluorescence measurements (MOT characterization). All metal components in the setup are made of non-ferrous materials (copper, aluminum) or nonmagnetic 316L stainless steel to prevent interference with experiments.

4.2.2 Custom Flange

To house the microwave cavity in the shared setup, a custom flange and cavity support have been designed and commissioned. The custom CF100 flange provides all the required optical and electrical feedthroughs for the experiment, and is intended to be mounted on the left cube face of the CF100 cube in Fig. 4.10. The cavity support connects the microwave cavity to the CF100 flange and ensures the grating in the cavity interior ends up at the correct position.

A schematic drawing of the custom CF100 flange is shown in Fig. 4.11. The viewport (1), located on the central axis of the flange, provides optical access for the trapping laser. It has a UV grade fused silica window with a 36 mm view diameter. The

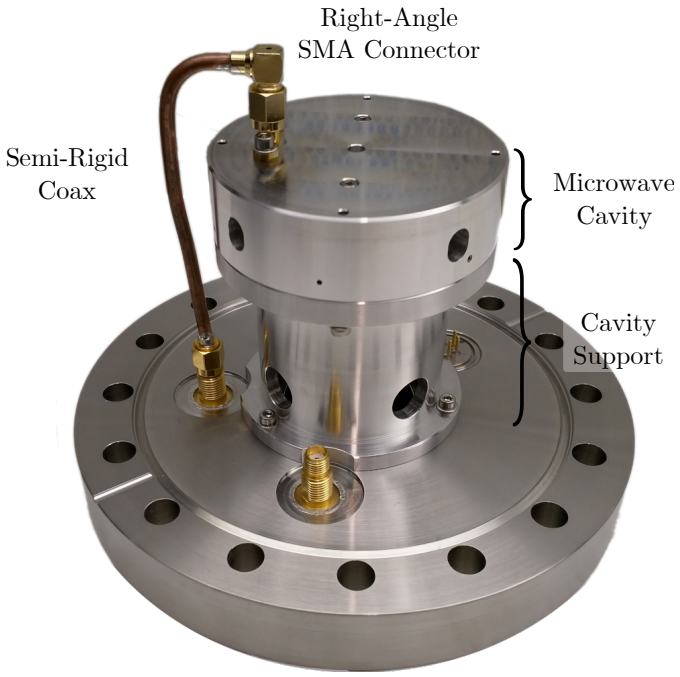

Figure 4.12: Microwave cavity mounted on the CF100 flange, vacuum side. The cavity support holds the microwave cavity in place and ensures the grating in the cavity interior is in the correct position within the setup. The semi-rigid coax cable transports microwave signals to the microwave cavity.

high quality 50 Ω SMA microwave feedthrough[4] (2) transports microwave signals for the MCRS experiment into the vacuum chamber. The SMA feedthrough transmits microwave signals in the frequency range of $0 - 18\,\mathrm{GHz}$ and is implemented in twofold to allow for multi-mode MCRS experiments in the future. The circular 6-pin electrical feedthrough (3) is installed to allow the microwave cavity temperature to be recorded with an NTC thermistor during the experiment. The CF100 flange is made of non-magnetic 316L stainless steel to prevent interference with the MCRS experiment and is specified at a helium leak-rate below $1 \times 10^{-10}\,\mathrm{mbar \cdot L/s}$.

The microwave cavity is mounted on the vacuum side of the CF100 flange on top of the cavity support, see Fig. 4.12. The cavity support is made of aluminum for its non-ferrous properties and UHV compatibility. Four 12 mm diameter holes in the base of the support help pumping down the cavity interior. The cavity support allows the propagation of the trapping laser into the microwave cavity and ensures the grating in the cavity interior ends up at 64.5 mm from the left cube face of the CF100 cube, see Fig. 4.10. In this position the MOT camera, trapping and ionization lasers in the setup can be reused without major realignment. A UHV compatible semi-rigid coax cable transmits the microwave signals to the microwave cavity. The SMA connectors are

[4] Allectra 242-SMAD18G

soldered to the semi-rigid coax cable using a UHV compatible silver solder[5].

For stable MOT operation, the background pressure in the vacuum vessel is preferably in the 10^{-9} mbar regime. The holes in the cavity and connector flange might hinder pumping down of the cavity and frustrate MOT operation in the cavity interior. At a pressure of 10^{-9} mbar, the mean free path of the gas molecules is sufficiently large for the gas flow to be in the free molecular flow regime. In this regime parts obstructing the gas flow (pipes, holes) are commonly described by a flow *conductance*, the inverse of the flow *resistance*. The conductance between the cavity interior and CF100 cube (all paths combined) is $2.9 \times 10^{-2}\,\mathrm{m}^3/\mathrm{s}$. The conductance between the cube interior and the ion-getter pump (see Fig. 4.10) is $2.7 \times 10^{-2}\,\mathrm{m}^3/\mathrm{s}$. With both conductances in the same order of magnitude, the pressure in the cavity interior is not limited by the cavity hole dimensions. Assuming a nitrogen (N_2) background gas, the ion-getter pump has a pumping speed of 40 L/s. A pressure reading of 1×10^{-9} mbar at the pump leads to a pressure of a few times 10^{-9} mbar in the microwave cavity interior, which is fine for MOT operation.

After installation of the microwave cavity onto the CF100 flange a curious effect was observed. For a critically coupled cavity ($\beta \approx 1$), the coupling factor of the cavity TM_{010} mode decreased by about $\Delta\beta = -0.2$, as measured on the atmospheric side of the CF100 flange (ⓒ in Fig. 4.11). By leaving the cavity (without flange) slightly overcoupled $\beta \approx 1.2$, a coupling factor close to the planned coupling factor $\beta = 1$ was achieved when mounted on the flange. This is the reason for leaving the cavity slightly overcoupled ($\beta = 1.21$) in Sec. 4.1.2.

A later investigation showed the drop in coupling factor disappeared when the semi-rigid coax cable, used to transport the microwave signal in vacuum, was replaced by a cable only containing straight SMA connectors. This suggests the drop in coupling factor is due to the right-angle SMA connector, connecting the semi-rigid coax cable to the microwave cavity antenna (see Fig. 4.12). The wavelength of an 5 GHz signal propagating in the semi-rigid coax cable is about 4 cm. Forcing the 5 GHz signal in a right-angle (90°) turn within a few millimeters is bound to cause reflections. Interference between the signal reflected on the connector, and microwave cavity could explain the drop in coupling factor, as measured on the flange. Details of the investigation can be found in the Appendix.

To determine the microwave cavity characteristics, the voltage reflection coefficient $|\Gamma_V|$ is measured as a function of frequency on two positions; on the flange (label: with flange), and on the cavity directly (label: without flange). The result is shown in Fig. 4.13. In the figure, data measured without flange is plotted in black, and data measured with flange is plotted in orange. The black line corresponds to the data in Fig. 4.7b. With flange, far off resonance, reflection is lower due to the extra propagation distance of the microwave signal in the transmission line (microwave feedthrough and semi-rigid coax). On resonance the voltage reflection coefficient without flange measures $\sim 10\%$ ($\sim 1\%$ in power), which drops to $\sim 4\%$ ($\sim 1‰$ in power) with the flange. On resonance reflection with the flange is lower due to the aforementioned drop in coupling factor. Data in the

[5]The solder is based on an Sn/Cu/Ag alloy

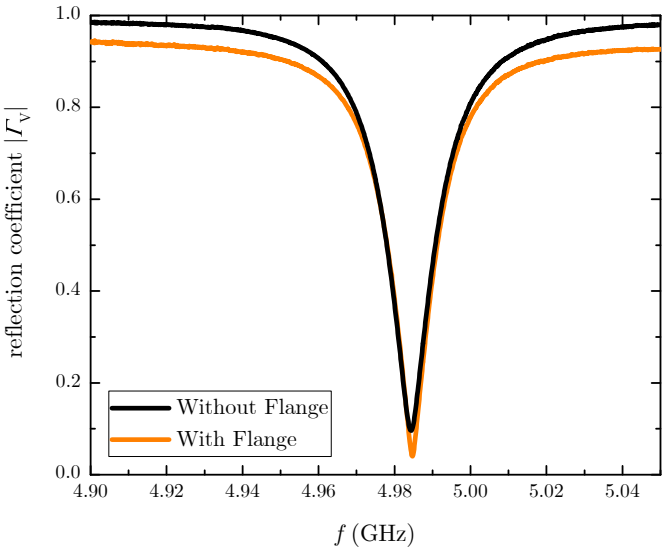

Figure 4.13: Voltage reflection coefficient $|\Gamma_V|$ as a function of frequency for the cavity TM_{010} mode. Comparison between measurements on cavity directly (label: without flange), and measured on the CF100 flange (label: with flange). Microwave cavity characteristics are listed in Table 4.2.

graph is fitted with Eq. 4.1 and fit results are listed in Table 4.2. Without flange, the resonance frequency of the cavity TM_{010} mode measures 4.98 GHz, the coupling factor is 1.21 and the loaded Q-factor $Q_L = 222$, as mentioned in Sec. 4.1.2. Here, the loaded Q-factor is mentioned as it is the parameter of practical importance in an MCRS experiment. It determines the width of the resonance peak, and the cavity response time in the measurement setup. When the microwave cavity is installed on the CF100 flange, the microwave cavity characteristics as perceived by the measurement setup change slightly to a resonance frequency of 4.99 GHz, a coupling factor of 1.06 and a loaded Q-factor $Q_L = 229$.

The reflection on the right-angle SMA connector slightly modifies the microwave cavity characteristics, as perceived by the MCRS measurement system outside the vacuum chamber. This modification is constant in time, and might only drift slowly with temperature due to material expansion (contraction). On the typical timescale of the MCRS experiment, defined by the UCP expansion ($1 - 100\,\mu$s), temperature drift is negligible and does not influence the experiment. In future experiments the right-angle SMA connector on the semi-rigid coax cable should be replaced by a straight SMA connector.

Table 4.2: Comparison of microwave cavity characteristics with and without flange. Data obtained from fitting the graphs in Fig. 4.13 with Eq. 4.1. Measurement errors are beyond the last digit.

	f_0 (GHz)	β	Q_L
Without Flange	4.98	1.21	222
With Flange	4.99	1.06	229

5 Results

To conduct the microwave cavity resonance spectroscopy (MCRS) experiment on an ultracold plasma (UCP), the microwave cavity and flange have been installed in the shared setup for grating based cold atom experiments. This chapter deals with the characterization of the MCRS setup, the creation and characterization of the MOT in the microwave cavity interior, and the attempt to conduct the envisaged proof-of-principle MCRS experiment on a UCP. The microwave cavity and experimental setup are described in Sec. 5.1. Section 5.2 deals with the MCRS measurement setup, measurement scheme and characterization. Finally, Sec. 5.3 describes the creation and characterization of the MOT in the microwave cavity interior, and the envisaged proof-of-principle experiment.

5.1 Setup

The microwave cavity and flange have been installed in the shared setup for cold atom experiments. An overview of the setup with the location of the main components is shown in Fig. 5.1. Sticking to the orientation of the CF100 cube faces introduced in the discussion of Fig. 4.10, the cavity and flange have been installed on the left cube face of the CF100 cube. The vacuum system is pumped down by the vacuum pumps located behind the reducer flange on the right cube face and the rubidium vapor is supplied by the dispensers on top of the cube. The rubidium gas is cooled and trapped by the trapping beam entering the vacuum system through the viewport in the cavity flange. The resulting magneto-optical trap (MOT) fluorescence is observed by two cameras. MOT camera 1 is located below the setup. MOT camera 2 is located in the ionization laser beam path, and observes the MOT fluorescence behind a dichroic mirror (mirror not in the figure). The ionization laser enters the vacuum system through the viewport at the front cube face and exits at the back viewport after passing through the cavity. In passing the cavity, the ionization laser pulse partially ionizes the MOT and the resulting UCP shifts the cavity resonance frequency. This shift in the cavity resonance frequency is subsequently recorded by the microwave setup located outside of the vacuum system (not shown in the figure). The microwave setup will be described in full detail the next section.

The trapping laser is based on a 780 nm diode laser[1] generating up to 250 mW of laser light. The laser is locked to the $\left(5^2\mathrm{S}_{1/2},\, F = 3 \rightarrow 5^2\mathrm{P}_{3/2},\, F' = 4\right)$ cooling transition by a rubidium vapor cell and passes an acousto-optic modulator (AOM) to be able to detune the light with respect to the transition. An electro-optic modulator

[1] Moglabs cateye diode laser

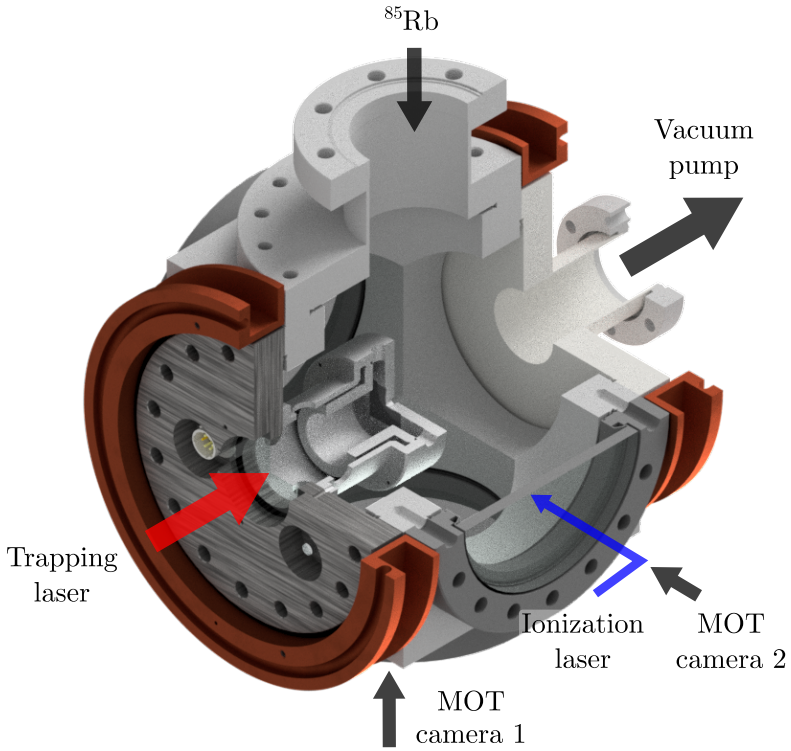

Figure 5.1: Overview of the MCRS setup with location and orientation of the main components; vacuum pumps, rubidium supply, trapping and ionization lasers and MOT cameras. MOT camera 2 is mounted behind a dichroic mirror in the ionization laser beam path.

(EOM) generates two sidebands at ±2.915 GHz, one of which drives the repump transition $\left(5^2S_{1/2},\, F = 2 \rightarrow 5^2P_{3/2},\, F' = 3\right)$ to keep the cooling transition populated. A more detailed description of the trapping laser can be found in Ref. [36]. The trapping laser light is amplified up to a maximum of 500 mW by a tapered amplifier[2] and coupled into a polarization maintaining fiber for transport to the setup. At the setup the laser light is coupled out of the fiber and expanded into a beam with a flattop-like transverse intensity profile measuring 1 inch in diameter (25.4 mm). Before entering the vacuum system, the trapping laser is circularly polarized with a $\lambda/4$ waveplate.

The flattop-like transverse intensity profile of the trapping laser is created by expanding the (Gaussian) beam exiting the fiber, and clipping the sides on an orifice. A flattop intensity profile is important in balancing the cooling force (Eq. 2.2) at the MOT position with our grating type [43]. A force imbalance in the cooling force reduces the trap depth of the magneto-optical trap and consequently the MOT atom number and density. A suboptimal MOT atom number would reduce the chance of measuring an MCRS signal in the experiment.

The ionization laser is a pulsed dye laser[3] which generates 6 ns FWHM pulses at a repetition rate of up to 10 Hz. With the Coumarin 480 laser dye, the accessible wavelength range is $460 - 500$ nm. Before transportation to the setup, the ionization laser is linearly polarized with a polarizing beamsplitter cube, and the laser wavelength is determined with a spectrometer[4]. At the setup, the ionization laser beam can be manipulated with a 2D translation stage to scan the MOT position and optimize the number of electrons in the UCP. After the stage a long focal length lens (750 mm) weakly focuses the ionization laser at the MOT. Before entering the vacuum system, 1% of the ionization laser light is split off and imaged on a CCD camera to determine the transverse intensity profile at the MOT position. The ionization laser is operated below maximum power, and at 10 Hz, to increase the laser stability. At the MOT position $\sim 300\,\mu$J pulses are available for the experiment. A cross section of the microwave cavity with orientation of the trapping and ionization lasers, MOT and overlap volume is shown in Fig. 4.3.

5.2 Microwave Cavity Resonance Spectroscopy

The microwave setup used to excite the cavity mode and determine its resonance frequency is a variation of the reflection based setup of Ref. [7]. A schematic representation of the setup is shown in Fig. 5.2. The cavity mode is excited by a microwave generator[5] capable of producing -60 to +14 dBm microwave signals in the frequency range of $25 - 6000$ MHz. The microwave signal arrives at the cavity after passing through the directional coupler[6] and microwave feedthrough in the cavity flange. After reflection on

[2] New Focus TA-7600
[3] Spectra-Physics Quanta-Ray PDL-3
[4] Avantes AvaSpec-3648
[5] Mini-Circuits SSG-6000RC
[6] Mini-Circuits ZHDC-10-63+

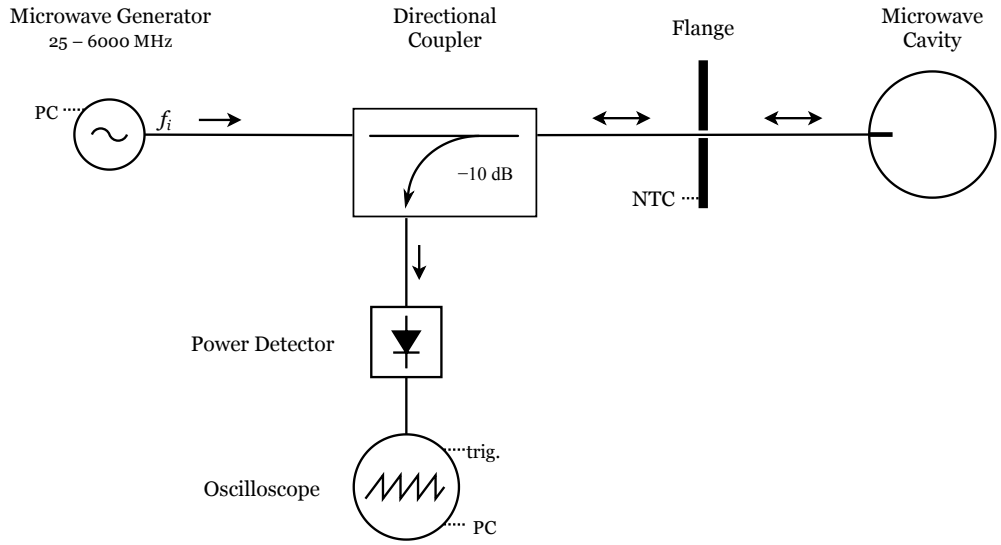

Figure 5.2: Microwave Setup. The microwave generator is connected to the cavity through a directional coupler. The directional coupler directs -10 dB of the microwave signal reflected by the cavity to the power detector. The DC voltage from the power detector is recorded by an oscilloscope.

the cavity, the directional coupler directs -10 dB of the reflected cavity microwave signal to the power detector[7]. The power detector is a logarithmic detector which converts the incoming microwave signal to a DC voltage. The power detector is sensitive to -60 to +10 dBm microwave signals in the frequency range of $1 - 8000$ MHz. Its DC output voltage ranges between $0 - 2$ V and has a negative nominal slope of -25 mV/dB. Finally, the power detector output voltage is recorded by an oscilloscope[8].

The power and frequency of the microwave generator, and the horizontal and vertical range of the oscilloscope as well as the number of averages N_{avg} are set by a PC. The oscilloscope is synchronized to the ionization laser by a trigger signal from a fast TTL pulse generator[9] and read out by the PC after the number of averages has been reached. To get an idea of the cavity temperature drift during the experiment, the temperature of the cavity flange is recorded with an NTC thermistor[10].

[7] Analog Devices HMC602
[8] Agilent Infinivision DSO7054A
[9] SpinCore PulseBlaster PB12-100-4k
[10] Epcos G560/5k/+

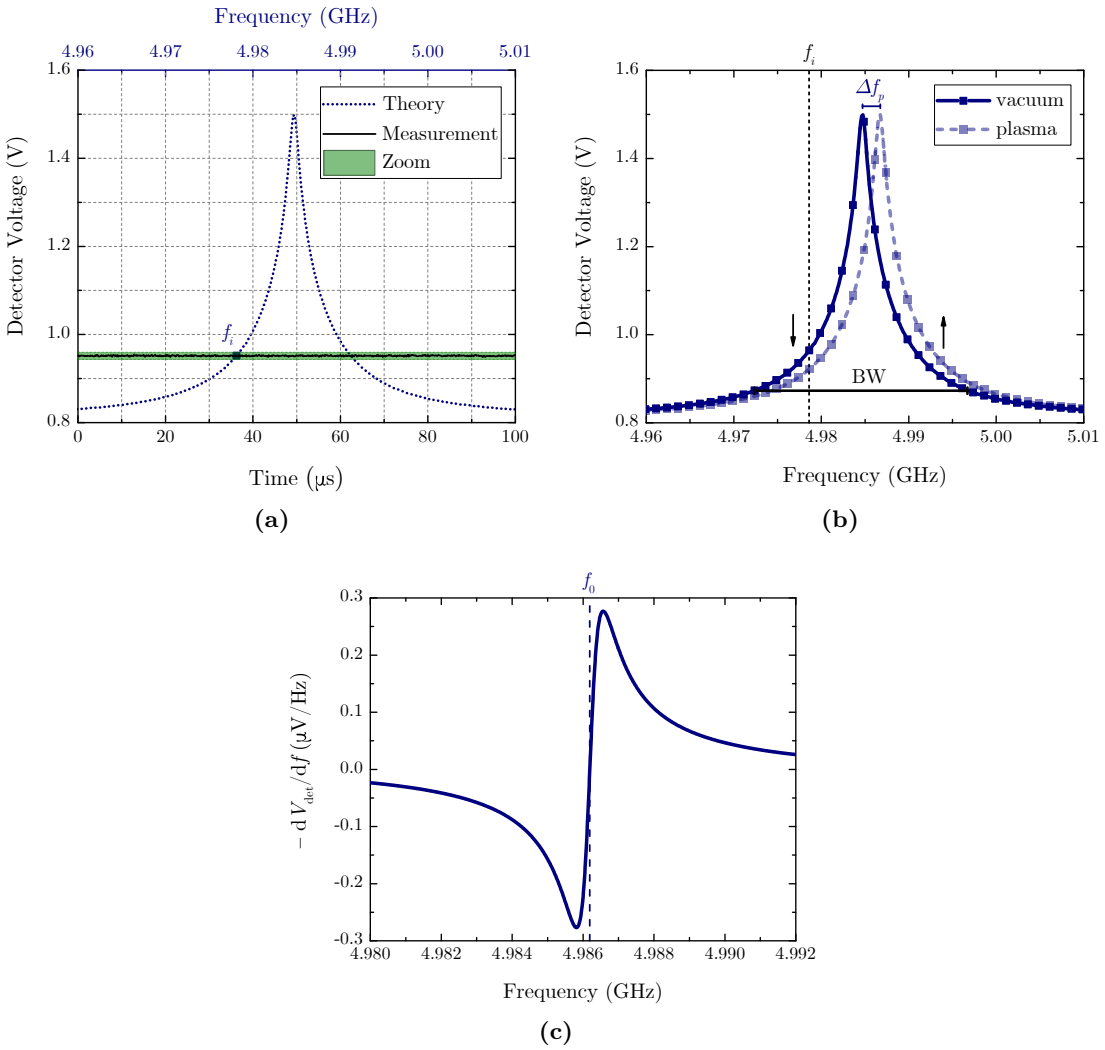

Figure 5.3: Explanation of the MCRS measurement scheme. **(a)** Example of an oscilloscope measurement trace (solid line) at frequency f_i. With oscilloscope zoom range (green band) and theoretical reflection curve (dotted line). Details in text. **(b)** Microwave cavity frequency shift Δf_p on the power detector due to the presence of a plasma (exaggerated). The detector voltage drops for frequencies $f_i < f_{\mathrm{vac}} + \frac{1}{2}\Delta f_p$, and rises for $f_i > f_{\mathrm{vac}} + \frac{1}{2}\Delta f_p$. For small shifts $\Delta f_p \ll \mathrm{BW}$ the change in detector voltage goes with the (negative) slope of the reflection curve $-\mathrm{d}V_{\mathrm{det}}/\mathrm{d}f$, see **(c)**.

5.2.1 Measurement Scheme

On the output port of the power detector, the reflected microwave signal from the cavity is converted to a DC voltage. In turn this detector voltage is recorded by the oscilloscope. An example of the theoretical reflection curve of the cavity mode as seen on the oscilloscope is shown in Fig. 5.3a. In the figure, the dotted line resembles the theoretical reflection curve (microwave power vs. frequency), with the frequency plotted at the top axis. The shape of the downward facing Lorentzian of Eq. 3.20 is modified due to the logarithmic nature of the detector, and faces upward due to its negative output slope.

An MCRS experiment entails tracking the resonance frequency of a cavity mode as a function of time, and determining the resonance frequency shift $\Delta f_p(t)$. To determine the mode resonance frequency with the setup described in Fig. 5.2, the resonance is scanned by the microwave generator with a discrete number of frequencies f_i, where $i = 1, 2, 3\ldots$ The oscilloscope is synchronized to the ionization laser by a trigger signal and the detector voltage V_{det} is recorded as a function of time during UCP expansion $\sim 100\,\mu$s. An example of an oscilloscope measurement trace is shown in Fig. 5.3a (solid line). To determine the mode resonance frequency at a specific time t_j in the experiment, all measurements $V_{\mathrm{det}}(f_i, t = t_j)$ are fitted with a modified version of Eq. 3.20 to include the effects of the logarithmic detector:

$$V_{\mathrm{det}}(f) = V_0 + 10C \cdot \log(1 - \mathcal{L}), \quad \text{where} \tag{5.1}$$

$$\mathcal{L} = A \cdot \frac{\mathrm{BW}^2}{4(f - f_0)^2 + \mathrm{BW}^2}. \tag{5.1a}$$

Here V_0 is a voltage offset of the peak on the detector, C is the detector slope and $\mathcal{L}$ denotes the Lorentzian of the reflection curve in Eq. 3.20. For fitting, the Lorentzian is slightly modified and rewritten in terms of ordinary frequencies. The modified Lorentzian is shown on the second line of the equation, with A the peak amplitude, and BW the FWHM bandwidth in ordinary frequency. The resonance frequency shift $\Delta f_p = f_p - f_{\mathrm{vac}}$ is determined as a function of time, and the field-averaged electron density $\bar{n}_e(t)$ is determined with the use of Eq. 3.33 for interpretation of the experiment.

In the envisaged MCRS experiment on a UCP, the resonance frequency of a vacuum cavity mode shifts due to the presence of the plasma. Since the relative plasma permittivity is smaller than unity ($\varepsilon_{r,p} < 1$) the resonance frequency shift is positive $\Delta f_p > 0$, see Fig. 5.3b. As illustrated in the figure, the resonance frequency shift will be observed as a change in detector voltage at generator frequency f_i. The voltage drops for frequencies $f_i < f_{\mathrm{vac}} + \frac{1}{2}\Delta f_p$, and rises for frequencies $f_i > f_{\mathrm{vac}} + \frac{1}{2}\Delta f_p$ (see arrows in the figure). Effects in the figure are exaggerated for clarity. For small shifts $\Delta f_p \ll \mathrm{BW}$ the change in detector voltage goes with the (negative) slope of the reflection curve on the detector $-\mathrm{d}V_{\mathrm{det}}/\mathrm{d}f$, see Fig. 5.3c. The change in detector voltage is maximal ($\pm 0.3\,\mu$V/Hz) close to the resonance, and changes sign across the resonance. Ultimately, the minimum frequency shift Δf_{min} that can be measured with the MCRS setup is limited by the resolution at which the detector voltage can be resolved by the oscilloscope. For the maximal expected frequency shift of $\Delta f_{\mathrm{max}} \sim 1.5\,$kHz, the maximal change in

detector voltage at constant frequency amounts to about $\Delta V_{\max} \sim \pm 0.5\,\mathrm{mV}$. This value is a crude measure for the lower limit of the oscilloscope resolution needed to resolve the frequency shift $\Delta f_{\max}$.

The oscilloscope used in the MCRS setup[8] has 8-bit vertical resolution, and a maximum sample rate of 4 GHz. It has 10 horizontal, and 8 vertical divisions as shown by the grid lines in Fig. 5.3a. The resonance peak of the microwave cavity TM_{010} mode measures about 0.7 V (28 dB). As shown in the figure, the oscilloscope vertical scale is set to 100 mV/div (0.8 V total) to be able to measure the full resonance peak. This results in a measurement resolution (least significant bit – LSB) of about 3 mV. Not enough to resolve the maximum expected frequency shift of the MCRS experiment. To maximize the MCRS measurement sensitivity, the scope vertical resolution is optimized in two ways:

1. The oscilloscope is zoomed in to its maximum vertical resolution of 2 mV/div for measurement at each generator frequency f_i. In this way the vertical resolution of the oscilloscope is increased 50×, as compared to the 100 mV/div full scale shown in Fig. 5.3. The green band in the figure represents the zoom range for the specific measurement trace at frequency f_i. In short the procedure is as follows: The generator is set to frequency f_i, and an oscilloscope trace of the experiment is recorded at full scale. The average voltage of the oscilloscope trace V_{avg} is read out by the PC, and the oscilloscope is zoomed to its maximum resolution centered on V_{avg}. Measurement data for the required number of repetitions N_{avg} is collected and the procedure is repeated at the next frequency f_{i+1} until finished.

2. The oscilloscope vertical resolution is artificially increased to 12-bit resolution with an oversampling technique. At relatively long time bases compared to the maximum sampling rate, the oscilloscope can combine multiple subsequent measurement samples into one data point (oversampling). For voltage signals with an RMS noise level exceeding 1/2 LSB, as is the case in our experiment, averaging of subsequent measurement samples leads to an increased measurement resolution. A time base of 10 µs/div leads to 4-bit of extra vertical resolution (12-bit total).

With these two techniques combined the oscilloscope measurement resolution is increased to an LSB of 4 µV, or a minimum detectable change in reflected power of 2×10^{-4} dB. The increased measurement resolution results in a minimum detectable frequency shift $\Delta f_{\min}$ in the order of 10 Hz that could be achievable in the experiment.

5.2.2 Measurement Sensitivity

In an MCRS measurement the MCRS signal depends on the *shift* of the resonance frequency f_0 of a cavity mode at successive time steps t_j. As such, the minimal detectable frequency shift $\Delta f_{\min}$ is limited by the RMS spread σ_{f_0} in the resonance frequency measurement. To test the setup, and determine the RMS spread of the resonance frequency measurement, an MCRS measurement on an empty cavity was performed.

The resonance of the TM_{010} cavity mode was scanned from 4.981 to 4.991 GHz in frequency steps of 100 kHz at a generator power of 10 dBm. The oscilloscope was operated

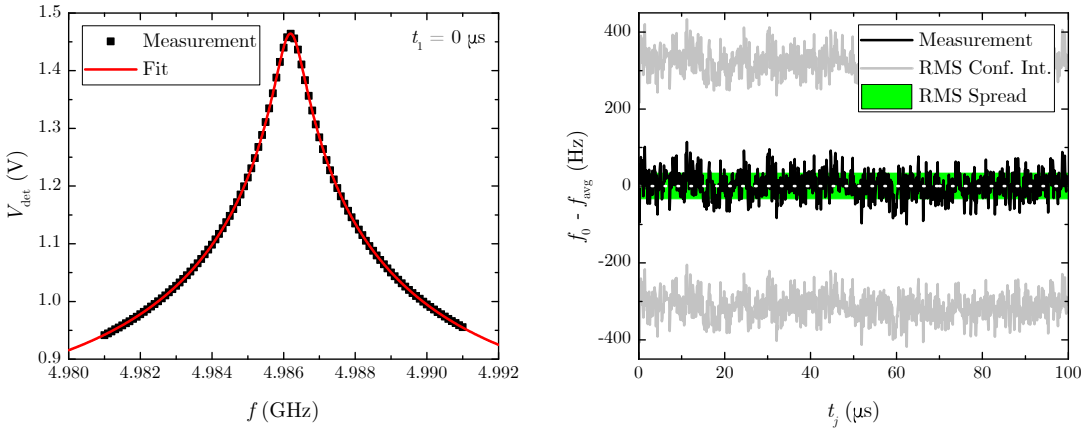

Figure 5.4: Determination of the MCRS measurement sensitivity on an empty cavity. **(a)** MCRS measurement at time step $t_1 = 0\,\mu$s. Measurement data (squares) is fitted with Eq. 5.1 (red line) to determine the resonance frequency $f_0\,(t_1)$. **(b)** Resonance frequency f_0 as a function of time t_j (black line). For clarity the difference with the average resonance frequency f_{avg} determined in the experiment is plotted $(f_0 - f_{\text{avg}})$. The RMS confidence interval of the fit procedure (gray line) measures $\sim 320\,$Hz, whereas the RMS spread in the resonance frequency (green bar) measures $\sigma_{f_0} = 34\,$Hz.

at maximum vertical resolution with the previously discussed measurement scheme, and every oscilloscope trace (1000 time steps t_j) was averaged $N_{\text{avg}} = 100$ times to reduce background noise. At a repetition rate of 10 Hz the MCRS measurement took about 20 minutes to complete.

All measurements $V_{\text{det}}\,(f_i, t = t_j)$ were fitted with Eq. 5.1 to determine the resonance frequency $f_0\,(t_j)$. An example of the measurement data (squares) and fit (red line) at time step $t_1 = 0\,\mu$s is shown in Fig. 5.4a. At a cavity temperature of about 22.6 °C the average resonance frequency of the TM_{010} mode was determined to be $f_{\text{avg}} = \overline{f_0\,(t_j)} = 4.9862\,$GHz. The resonance frequency f_0 is plotted as a function of time t_j in Fig. 5.4b (black line). For clarity, the resonance frequency is plotted in terms of the difference with the average resonance frequency determined in the experiment $(f_0 - f_{\text{avg}})$. The RMS confidence interval of the individual resonance frequency measurements $f_0\,(t_j)$ measures about $\sim$ 320 Hz and is shown by the gray lines in the figure. The RMS spread σ_{f_0} in the resonance frequency measurements (green bar) is considerably smaller, and measures $\sigma_{f_0} = 34\,$Hz. This is the MCRS measurement resolution of the experiment, and a good measure for the minimum detectable frequency shift Δf_{min}.

The minimum detectable frequency shift of $\Delta f_{\text{min}} = \sigma_{f_0} = 34\,$Hz is within the expected order of magnitude determined by the oscilloscope vertical resolution ($\sim$ 10 Hz) and results in a minimum relative shift of $\Delta f_{\text{min}}/f_0 = 7 \times 10^{-9}$. The minimum detectable frequency shift corresponds to a field-averaged electron density $\bar{n}_e = 4 \times 10^9\,\text{m}^{-3}$ or about 3×10^4 electrons at the expected MOT position on the cavity z-axis, 5 mm above the

grating surface. It provides ample resolution to resolve the maximum expected frequency shift $\Delta f_{\max} \sim 1.5\,\mathrm{kHz}$, even if a suboptimal number of rubidium atoms can be trapped and ionized. The minimum detectable field-averaged electron density is more than two orders of magnitude below the previous record mentioned in scientific literature [7]. A considerable result in its own right.

This measurement on an empty cavity has been optimized to maximize the MCRS measurement resolution (minimize $\Delta f_{\min}$) within a practical measurement time. Increasing the number of frequency steps and/or number of averages per frequency step could still improve the MCRS measurement resolution.

Temperature drift

In this proof-of-principle experiment, the cavity temperature is measured on the atmospheric side of the cavity flange, see Figs. 5.1 and 5.2. In future experiments the temperature should be measured in vacuum, on the cavity directly, to rule out ambiguities in the measurement.

During the empty cavity measurement, the temperature of the cavity flange drifted by about 30 mK, see Fig. 5.5a. In the figure the flange temperature drift ΔT is plotted as a function of measurement time t_m (bottom axis) and corresponding generator frequency f_i (top axis). In the experiment, the cavity is thermally isolated from the environment apart from the cavity support on which it is mounted (see Fig. 4.12). The only potential source heating the cavity is the microwave power coming from the generator. The microwave generator operates at 10 dBm, of which about 5 dBm (3 mW) reaches the cavity. Even at this low power, heat conduction through the cavity support is not sufficient to be sure the cavity follows the temperature of the cavity flange. During measurement, the cavity temperature could deviate from the value measured on the flange. If, in a worst-case scenario, all generator power would be absorbed by the 170 g cavity, the cavity temperature would rise 25 mK on top of the temperature drift of the cavity flange (55 mK total). Let's assume the cavity temperature drift measured 100 mK in the experiment. For the cavity TM_{010} mode with a resonance frequency of 4.99 GHz the temperature drift results in a frequency drift of $\Delta f_{\mathrm{drift}} = \text{-}12\,\mathrm{kHz}$ (see Eq. 3.4). Very small compared to the bandwidth of the resonance peak $|\Delta f_{\mathrm{drift}}| \ll \mathrm{BW}$, where $\mathrm{BW} = 22\,\mathrm{MHz}$.

The effect of temperature drift on the MCRS measurement is illustrated in Fig. 5.5b for small drifts $|\Delta f_{\mathrm{drift}}| \ll \mathrm{BW}$. In the figure the resonance peak of the cavity mode drifts over a range $\Delta f_{\mathrm{drift}}$ between the start (dotted line) and end (dashed line) of the measurement. The positive temperature drift $\Delta T > 0$ ($\Delta f_{\mathrm{drift}} < 0$) and scanning direction $f_{i+1} > f_i$ have the result that the measured resonance peak (squares) appears contracted on the detector. The measured resonance frequency f_0 obtained through fitting (solid line) lies within the resonance frequency drift range of the measurement.

Due to the temperature drift in the empty cavity measurement, the relative error in the (absolute) accuracy of the measured resonance frequency $\Delta f_{\mathrm{drift}}/f_0 \sim 10^{-6}$ is higher than the relative MCRS measurement resolution $\Delta f_{\min}/f_0 \sim 10^{-8}$. This is fine in the case of an MCRS experiment where the resonance frequency *shift* is the important metric. For small frequency drifts $|\Delta f_{\mathrm{drift}}| \ll \mathrm{BW}$ the resonance peak will be slightly

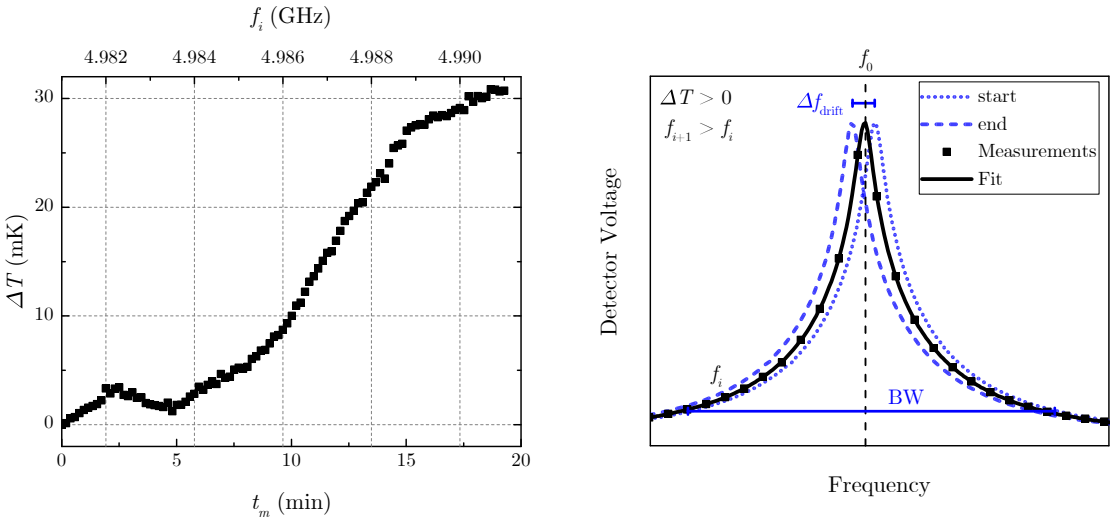

Figure 5.5: Temperature drift during an MCRS measurement. **(a)** Temperature drift ΔT during the empty cavity measurement as measured on the cavity flange. Bottom axis: measurement time t_m. Top axis: generator frequency f_i. **(b)** Influence of temperature drift on an MCRS measurement. For a positive temperature drift ($\Delta T > 0$), the resonance peak drifts towards lower frequencies between the start (dotted line) and end (dashed line) of an MCRS measurement. For small drifts $|\Delta f_{\text{drift}}| \ll \text{BW}$, and a positive scanning direction $f_{i+1} > f_i$, the measured resonance peak (squares) appears contracted on the detector. A stable resonance frequency f_0 within the drift range is obtained through fitting (solid line). Drift in the figure is exaggerated for clarity.

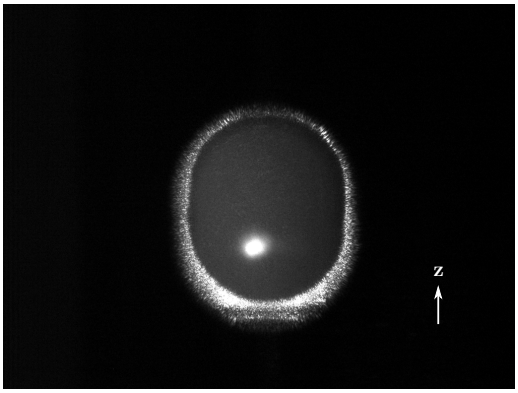

Figure 5.6: First MOT in the microwave cavity interior. In the photo, the MOT fluorescence is shown in white.

deformed on the detector, however it will shift on the timescale of the UCP expansion ($\sim 100\,\mu$s). Small temperature drifts have a negligible influence on the envisaged MCRS measurement due to the large disconnect in timescales of the respective processes. The cavity frequency drifts $\sim 10\,$kHz in a time span of ~ 10 minutes whereas the expected frequency shift measures $\sim 1\,$kHz in $\sim 100\,\mu$s.

5.3 Proof-of-Principle

To conduct the MCRS experiment on a UCP, a MOT was created in the microwave cavity interior, see Fig. 5.6. The figure shows a photo of the MOT fluorescence as seen through one of the small holes in the cavity side wall at the back viewport of the setup. Subsequently the MOT parameters have been optimized for the proof-of-principle experiment.

In first experiments, the MOT loading and ionization scheme is kept as simple as possible. The trapping laser loads the MOT continuously, and the ionization laser creates UCPs at a repetition rate of 10 Hz. The MOT atom number and loading time are optimized with MOT camera 1 located below the setup to maximize the total number of electrons in the UCP. Both MOT parameters depend on the background rubidium pressure in the vacuum system. A higher rubidium pressure leads to faster MOT loading times, and a lower MOT atom number due to an increased number of collisions with the hot rubidium atoms in the background. The MOT loading rate was determined by switching on the trapping laser at $t = 0\,$s and determining the MOT atom number N_a at different time steps through fluorescence measurements. Measurements are fitted with Eq. 2.8 to determine the linear loss rate Γ_{BG}, and related loading time $\tau_{\mathrm{load}} = \Gamma_{\mathrm{BG}}^{-1}$, as well as the MOT atom number N_a at long times $t \gg \tau_{\mathrm{load}}$.

To prevent MOT depletion during ionization, the MOT atom number was optimized with the constraint of the MOT loading time approximately matching the repetition period of the ionization laser ($\tau_{\mathrm{load}} \approx 100\,$ms). Optimum conditions were found at a

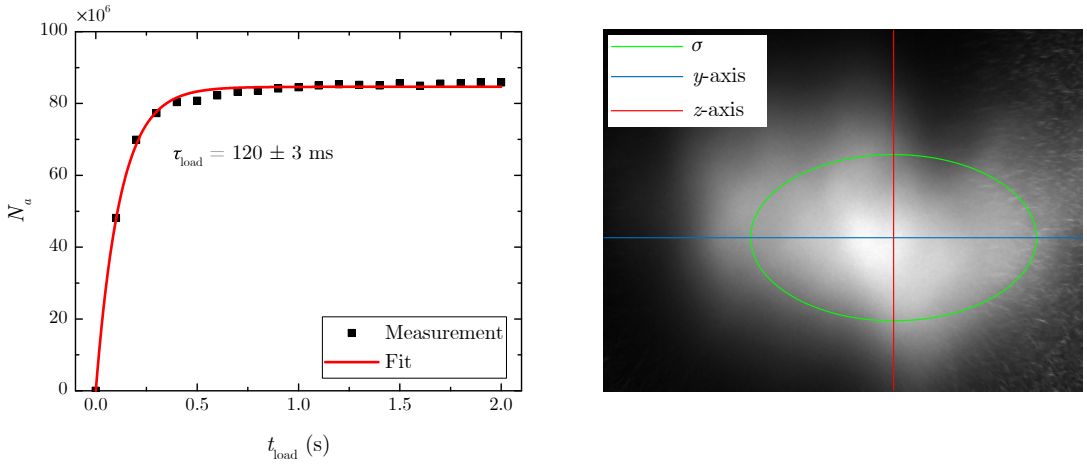

(a) **(b)**

Figure 5.7: Optimized MOT characteristics at $p_{\mathrm{Rb}} = 2.2\times10^{-9}$ mbar. **(a)** MOT loading curve. The MOT atom number N_a is fitted with Eq. 2.8 as a function of time t_{load}. The MOT has a loading time of $\tau_{\mathrm{load}} = 120 \pm 3$ ms and a maximum number of atoms $N_a = 84.6 \pm 0.3 \times 10^6$ when fully loaded. **(b)** Picture of a fully loaded MOT with 2D Gaussian fit. The MOT RMS size (green line) measures $\sigma_{ay} = 825 \pm 1\,\mu$m and $\sigma_{az} = 479 \pm 1\,\mu$m.

partial rubidium pressure of $p_{\mathrm{Rb}} = 2.2 \times 10^{-9}$ mbar, measured at the ion-getter pump. The pressure of all other atomic and molecular species in the background gas was $p_X < 10^{-10}$ mbar. In Fig. 5.7a the MOT loading curve is plotted and fitted with Eq. 2.8 as discussed previously. This leads to a loading time of $\tau_{\mathrm{load}} = 120 \pm 3$ ms and an atom number $N_a = (84.6 \pm 0.3) \times 10^6$ when the MOT is fully loaded. During the experiment MOT coil 1 was driven at I_1 = -8.2 A and coil 2 at I_2 = 14.0 A, see Fig. 4.10 for coil locations. The trapping laser power incident on the grating measured 40.6 mW/cm^2 of which $\sim$ 55% drives the cooling transition and $\sim$ 20% is in the sideband driving the repump transition. The remainder of trapping laser power is in the second repumper sideband and its higher orders and do not contribute to the experiment. The optimized MOT is located on the cavity z-axis, approximately 3.45 mm above the grating surface, and has an RMS size of $\sigma_{ay} = 825 \pm 1\,\mu$m and $\sigma_{az} = 479 \pm 1\,\mu$m, see Fig. 5.7b. The MOT x-dimension cannot be observed on MOT camera 1.

The number of atoms in the MOT is about a factor 7 higher than expected during the MOT estimations in Sec. 2.3 ($\sim 8.5 \times 10^7$ measured where $\sim 1.2 \times 10^7$ were expected). This result is a consequence of the trapping laser characteristics. In a previous attempt, we could only trap 2.4×10^6 rubidium atoms with a collimated trapping laser with a Gaussian transverse intensity profile and a 1/e^2 diameter of 25 mm. The estimations in Sec. 2.3 are based on experiments in Ref. [13] in which the collimated trapping laser has a Gaussian transverse intensity profile with a 40 mm 1/e^2 diameter. It seems the MOT atom number improves considerably the closer the trapping laser resembles a flattop

transverse intensity profile. Higher up in the overlap volume the lower intensity wings of the trapping laser could lead to an imbalance in the cooling force acting upon the MOT atoms. An imbalance in the cooling force leads to a reduced MOT trap depth and atom number. A second possibility is the (ever so slight) divergence of the flattop like trapping beam used in the final experiment. In discussion with the grating developers of the *Riis group*, Dr. A.S. Arnold reported the GMOT atom number is very sensitive to beam divergence/convergence. The effect is not yet fully understood and on their list of ideas for future research. Either way, the result is beneficial for the envisaged MCRS experiment. Note, at the time of the experiment the tapered amplifier output was halved at a maximum of 0.25 W due to a manufacturing problem. The MOT atom number as a function of trapping laser power has not yet saturated, so it is possible more atoms can be trapped when the tapered amplifier is repaired.

To conduct the experiment, the ionization laser was aligned through the cavity. For a maximum number of electrons in the UCP, and an optimal MCRS signal, the ionization laser was scanned over the MOT position with the 2D translation stage. The ionization laser was set to a wavelength of 477.86 nm corresponding to an initial electron temperature $T_e = 50\,\mathrm{K}$. It contained 260 μJ per pulse at a repetition rate of 10 Hz. Due to the new loss channel of the MOT ionization, the MOT atom number reduced to $N_a = (7.0 \pm 0.1) \times 10^7$. The resonance of the TM_{010} cavity mode was scanned from 4.981 to 4.991 GHz in frequency steps of 100 kHz, the same as in the empty cavity measurement. The generator power remained 10 dBm and measurements at every generator frequency were averaged with $N_{\mathrm{avg}} = 100$ times. All potential sources heating the cavity, like the MOT coils and trapping laser, were switched on more than an hour before the experiment to be sure the cavity temperature has stabilized. The measurement took about 33 minutes to complete.

First measurement results of the proof-of-principle MCRS experiment are shown in Fig. 5.8. In the figure the detector voltage V_{det}, recorded by the oscilloscope, is plotted as a function of time t after ionization for a few frequency steps across the vacuum resonance frequency $f_{\mathrm{vac}} = 4985.85\,\mathrm{MHz}$ at 25.0 °C. As expected, the detector voltage drops for generator frequencies below, and rises for generator frequencies above, resonance. Also, the shift in detector voltage increases with distance to the resonance for the generator frequencies presented here. Further away from resonance, the shift in detector voltage diminishes as expected.

In Fig. 5.9 the temperature drift of the cavity flange ΔT is plotted as a function of measurement time t_m. The corresponding generator frequency f_i is plotted at the top axis. During the experiment, the temperature of the cavity flange changed by about ΔT = -45 mK. The total cavity temperature drift, including cavity heating by the power from the microwave generator, is well within 100 mK and has a negligible influence on the experiment.

The measurement data of the proof-of-principle experiment has been fitted with Eq. 5.1 to determine the resonance frequency shift. The result is shown in Fig. 5.10. In the figure the cavity resonance frequency shift Δf_p of the TM_{010} mode has been plotted as a function of time t after ionization (black line). The field-averaged electron density $\bar{n}_e$ on the right axis is reconstructed with the use of Eq. 3.35.

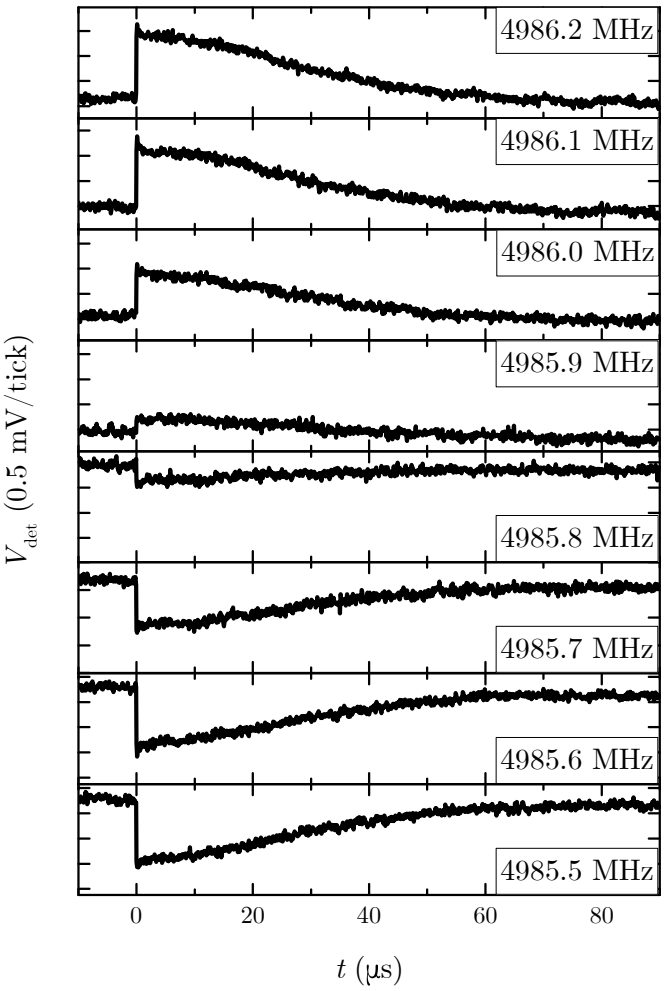

Figure 5.8: Detector voltage V_{det} as a function of time after ionization t at different generator frequencies 4985.5−4986.2 MHz. Measurements are averaged $N_{\mathrm{avg}} = 100$ times and shown on a constant vertical scale of 0.5 mV per tick. Notice the shift in V_{det} changes sign across the resonance, in between generator frequency 4985.8 and 4985.9 MHz. The shift increases with distance to the resonance.

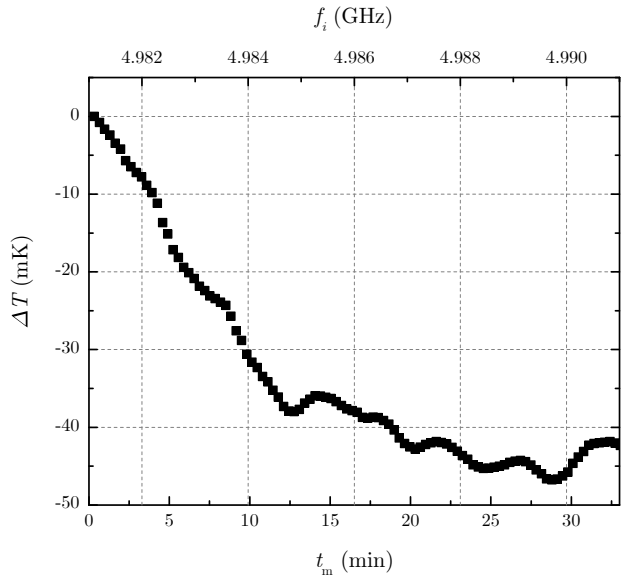

Figure 5.9: Temperature drift ΔT during the proof-of-principle MCRS experiment as measured on the cavity flange. Bottom axis: measurement time t_m. Top axis: generator frequency f_i.

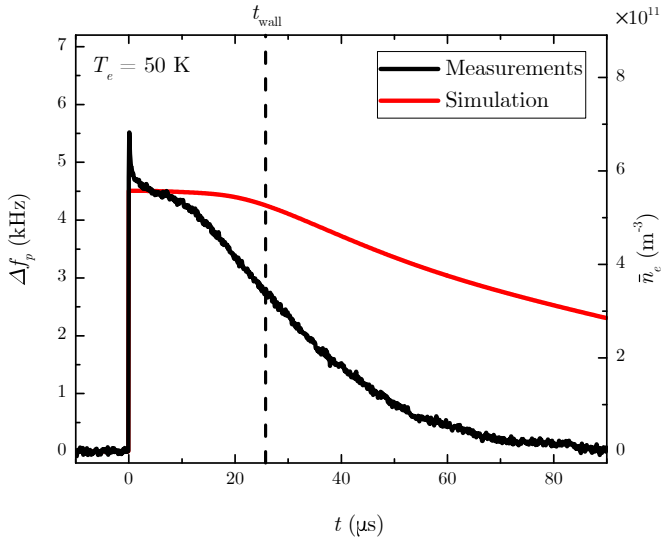

Figure 5.10: Proof-of-Principle MCRS experiment on a ^{85}Rb UCP. The cavity frequency shift Δf_p of the TM_{010} mode is plotted as a function of time t after ionization (black line). The field-averaged electron density $\bar{n}_e$ on the right axis is reconstructed with Eq. 3.35. The simulated cavity frequency shift (red line) is determined using the simulated cavity fields and the self-similar expansion model of Eq. 2.24. With an initial electron temperature $T_e = 50\,\mathrm{K}$, the expansion velocity is $v_{\mathrm{exp}} \approx 66\,\mathrm{m/s}$. In simulations the MOT arrives at the nearest wall (grating reflector) at $t_{\mathrm{wall}} \approx 26\,\mu\mathrm{s}$ (dashed line). Details in text.

The evolution of the MCRS signal can be divided into two distinct phases related to characteristic processes within the lifetime of a UCP. In the first phase, the frequency shift rises to 5.5 kHz and quickly declines to about 4.5 kHz within a time span of 1 μs after ionization. This is the electron-electron, and ion-ion equilibration phase. Hot electrons escape the UCP and the plasma becomes slightly positively charged due to the ion surplus. The net positive charge creates a potential well, trapping the remaining electrons. This is the free-space analogue of the formation of a plasma sheath on a wall. The process continues during ion-ion equilibration. Disorder-induced heating (DIH) of the ions acts as an energy source for the electrons and hot electrons keep escaping the plasma until ion-ion equilibration is finished. This is typically the case after a few periods of the ion plasma frequency, or about $\sim 1\,\mu$s. In the second phase the UCP freely expands into the microwave cavity interior driven by the thermal energy of the remaining electrons. In the expansion phase, two subphases can be distinguished related to the cavity electric field profile. The UCP is created at $z = 3.45$ mm on the cavity central axis. This is within the region of the flattop electric field profile of the cavity mode, see Figs. 4.8 and 4.9. The UCP expands into a region of near-constant electric field amplitude and the resulting MCRS signal is near-constant up to $t \sim 10\,\mu$s. After $\sim 10\,\mu$s the UCP expands into the rest of the cavity interior and experiences a lower electric field amplitude. The MCRS signal declines until diminished at $\sim 90\,\mu$s, a typical value for the lifetime of a UCP.

For the quantitative analysis of the MCRS signal, the initial number of electrons and dimensions of the UCP have been determined with Eq. 2.18. In the proof-of-principle experiment, the MOT contained $N_a = (7.0 \pm 0.1) \times 10^7$ atoms in a volume with RMS dimensions $\sigma_{ax} = 1198 \pm 8\,\mu$m, $\sigma_{ay} = 788 \pm 6\,\mu$m and $\sigma_{az} = 498 \pm 2\,\mu$m centered on the z-axis at a height $z = 3.45$ mm above the grating. The ionization laser pulse contained 260 μJ per pulse at a wavelength of 477.86 nm and measured $\sigma_{I_x} = 368 \pm 7\,\mu$m and $\sigma_{I_z} = 189 \pm 8\,\mu$m at the MOT position. By interpolation of measurement results in Ref. [20], the photoionization cross section at the ionization laser wavelength was determined to be $\sigma_{\mathrm{PI}} = 17 \times 10^{-22}\,\mathrm{m}^2$. The resulting UCP contains $N_e = 5.26 \times 10^6$ electrons in an approximate Gaussian density distribution with initial RMS dimensions $\sigma_{ex0} \approx 420\,\mu$m, $\sigma_{ey0} \approx 770\,\mu$m and $\sigma_{ez0} \approx 210\,\mu$m. The evolution of the UCP expansion has been determined with the self-similar expansion model of Eq. 2.24 for $t > 0$. At an initial electron temperature of $T_e = 50$ K, the expansion velocity measured $v_{\mathrm{exp}} \approx 66$ m/s. The resulting cavity frequency shift Δf_p and field-averaged electron density $\bar{n}_e$ have been determined using Eqs. 3.34 and 3.35, and the simulated cavity fields discussed in Ch. 4. The resulting simulated cavity frequency shift is shown by the red line in Fig. 5.10. After an expansion time of $t_{\mathrm{wall}} \approx 26\,\mu$s the UCP expands into the nearest wall that is the grating reflector ($2\sigma_{ez}(t_{\mathrm{wall}}) = 3.45$ mm). This is indicated by the dashed vertical line in the figure. At this time, the concequences of the plasma-wall interaction on the self-similar plasma expansion model are unclear. One could expect a deviation from the model due to recombination on the cavity wall, and rising asymmetries in the plasma density distribution. In the current simulations, electrons touching the wall surface are simply excluded from simulations and the plasma is left to expand in self-similar fashion.

The simulated cavity frequency shift at $t = 0$ s measures 4.5 kHz and is within 20% of

the measured value. A good result given all the uncertainties in laser alignment, MOT and laser dimensions and the photoionization cross section. However, the simulated MCRS signal decline is considerably slower as compared to the MCRS measurements. At $t_{\mathrm{wall}} = 26\,\mu$s the measured MCRS signal has lost about 50% of its initial value whereas the simulated MCRS signal has only just started to decrease. On closer inspection there are a few signs of electron heating and an increased UCP expansion velocity in the MCRS signal of Fig. 5.10. The initial peak in the MCRS signal of the hot electrons leaving the plasma measures about 1 kHz, or about 18% of the maximum. This points to 88% of the electrons remaining trapped in the plasma. Extrapolating the data in Ref. [11], a UCP with 5.25×10^6 electrons and an initial electron temperature of 50 K is expected to retain about 98% of its electrons. Electron heating by the microwave fields could explain the increased loss of electrons [44]. Also, curiously, there is no change in the measured MCRS signal at the expected time the UCP touches the wall (t_{wall}). One would expect an increased decline in MCRS signal due to plasma recombination on the wall surface. The decline in the MCRS measurement already starts at $\sim 10\,\mu$s. This points to an increased UCP expansion velocity, possibly the consequence of the electron heating discussed previously. Further experiments will have to shed light on these effects.

6 Conclusions

In this thesis a proof-of-principle microwave cavity resonance spectroscopy (MCRS) experiment on an ultracold plasma (UCP) is described. The UCP is created by two-step photoionization of a cloud of cold rubidium atoms trapped in a grating based magneto-optical trap (GMOT) in the interior of a microwave cavity. The main body of this thesis deals with microwave cavity design and commissioning after which a proof-of-principle MCRS experiment has been demonstrated.

This research has shown it is possible to retain the Q-factor of a cavity mode in a microwave cavity with a relatively big hole in the cavity walls. In particular, the unloaded Q-factor of the TM_{010} mode of a cylindrical pillbox cavity geometry was optimized by varying the length of the hole required for optical access of the trapping laser to the cavity interior. The unloaded Q-factor of the commissioned aluminum cavity without grating measured $Q_{\mathrm{cav}} = 3848 \pm 8$, close to the theoretical maximum of $Q_{\mathrm{cav}} \sim 4250$ for a pillbox cavity with the same dimensions. Maximizing the Q-factor of a cavity mode has two important results in the context of an MCRS experiment:

- It maximizes the MCRS measurement resolution and detection limit as a high-Q (narrow) resonance peak is more easy to resolve with high accuracy.
- It isolates the MCRS experiment from the surrounding environment. If not isolated, microwave sources outside the cavity might influence the MCRS measurement, or the cavity behavior could become sensitive to the setup geometry in the proximity of the hole in the cavity wall (i.e. reflections).

The hole for the trapping laser did have a considerable influence on the field profile and resonance frequency of the TM_{010} mode. The 'Bessel' shape of the radial electric field profile changed into a flattop profile, and the resonance frequency shifted from 4.6 GHz to about 5.0 GHz.

Due to the installation of the grating into the cavity interior the unloaded Q-factor of the TM_{010} mode dropped from $Q_{\mathrm{cav}} = 3848 \pm 8$ to $Q_{\mathrm{cav}} = 491.0 \pm 0.3$. The 100 nm aluminum reflector on top of the grating has a considerably higher surface resistance ($R_s \sim 300\,\mathrm{m\Omega}$) than the aluminum cavity walls ($R_s \sim 25\,\mathrm{m\Omega}$) and increased dissipation of microwave power in the grating reflector leads to a lower Q-factor of the cavity mode. The problem is further aggravated by concentration of surface currents on the reflector edges and grating clamps. A solution to mitigate this problem will be presented in the next chapter.

We have shown it is possible to cool and trap ^{85}Rb atoms in the microwave cavity interior in a magneto-optical trap (MOT) based on the GMOT concept. Trapping laser light reflected into the negative grating order does not get back to the MOT position

and does not disturb the MOT balance with this cavity geometry. Using a trapping beam with a flattop-like transverse intensity profile $(84.6 \pm 0.3) \times 10^6$ rubidium atoms can be trapped in the cavity interior, about 7 times more than expected. The higher MOT atom number is a consequence of the trapping laser characteristics as in an earlier attempt with a Gaussian trapping laser beam only 2.4×10^6 atoms could be trapped. The details about the mechanism of the improved trapping are not fully understood, however the result is very beneficial for the realization of the experiment.

With the MCRS setup the resonance frequency of the cavity TM_{010} mode can be resolved up to an RMS noise level of $\sigma_{f_0} = 34\,\mathrm{Hz}$ (relative $\sigma_{f_0}/f_0 = 7 \times 10^{-9}$) in a measurement time of about 20 minutes. This corresponds to a minimum detectable field-averaged electron density of $\bar{n}_e = 4 \times 10^9\,\mathrm{m}^{-3}$, more than two orders of magnitude better than the previous record mentioned in scientific literature [7]. The detection limit corresponds to about 3×10^4 electrons on the cavity central axis, a considerable result in its own right. With increased averaging, the detection limit could be reduced even further at the cost of measurement time. A cavity temperature drift of 100 mK (12 kHz) over the total measurement time is not a problem in the experiment as it only influences the *absolute* resonance frequency, not the resonance frequency *shift* important to the MCRS experiment. Temperature drift on the timescale of UCP expansion ($\sim 100\,\mu\mathrm{s}$) is practically non-existent and can be safely neglected.

A proof-of-principle MCRS experiment on a UCP has been demonstrated. In the experiment, the MOT atom number dropped to $(7.0 \pm 0.1) \times 10^7$ atoms due to repeated ionization of the MOT atom cloud by the ionization laser. Qualitatively the recorded MCRS signal behaves as expected. An initial peak in the MCRS signal points to hot electrons escaping the UCP. The ion surplus creates a potential well, trapping the remaining electrons. The flattop electric field profile of the cavity mode results in a near-constant MCRS signal in the first $\sim 10\,\mu\mathrm{s}$ of the UCP expansion phase. After $10\,\mu\mathrm{s}$ the MCRS signal declines on the timescale of about $90\,\mu\mathrm{s}$, typical for the lifetime of a UCP. Quantitatively the measured maximum resonance frequency shift of $\Delta f_{\max} = 5.5\,\mathrm{kHz}$ is within 20% of the expected value determined through fluorescence measurements in combination with simulations. However, the electron temperature seems higher than expected. About 18% of the electrons escape the plasma within a microsecond after formation, where a loss of a few percent was expected. Also, the measured MCRS signal drops off before the UCP is expected to have expanded into the nearest cavity wall. Both effects could be explained by electron heating by the microwave cavity fields [44]. These effects will have to be investigated in more detail in future experiments.

7 Outlook

As with any first demonstration of a measurement technique applied to an existing field of physics, new measurement possibilities arise exploiting the technique's particular strengths. The validity of previous experimental results can be tested and new experimental frontiers can be probed. With the demonstration of the proof-of-principle microwave cavity resonance spectroscopy (MCRS) experiment on an ultracold plasma (UCP) a new technique to study UCPs has arrived [10, 11]. With MCRS we probe the average plasma electron density in situ in a nondestructive fashion and with submicrosecond temporal resolution. The opportunities for future research are many, here we name a few.

By scanning the power and wavelength of the ionization laser the relation between the initial electron temperature and the fraction of trapped electrons can be revisited, see Ref. [11]. The same holds for the relation between the initial electron temperature and the UCP expansion velocity of Eq. 2.25. These experiments might shed new light on the lower trapped electron fraction and the discrepancy fall off time scales between the simulated, and measured, MCRS signal in the proof-of-principle experiment. The same experiment could yield information about the ^{85}Rb photoionization cross section from the $5^2P_{3/2}$-level at arbitrary wavelengths above the ionization threshold.

MCRS is the first measurement technique available that can study the behavior of the UCP electron density on a submicrosecond timescale. It would be interesting to investigate whether there is any structure within the peak of the hot electrons escaping the plasma in the first stage of UCP evolution.

The single most detrimental effect on the MCRS measurement sensitivity of the proof-of-principle experiment is the drop in Q-factor due to the installation of the grating into the microwave cavity interior. The unloaded Q-factor dropped from $Q_{\mathrm{cav}} \sim 3850$ to

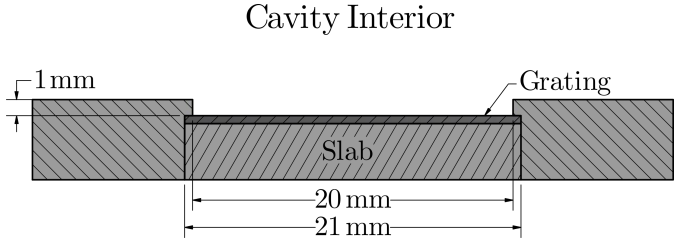

Figure 7.1: Cross section of the microwave cavity back wall with receded grating. The $21 \times 21\,\mathrm{mm}^2$ grating is clamped flush to a $20 \times 20\,\mathrm{mm}^2$, 1 mm deep hole in the cavity back wall. The $20 \times 20\,\mathrm{mm}^2$ patterned grating surface is exposed to the cavity interior and the 0.5 mm rim has full electrical contact with the cavity back wall.

~ 500 due to the high surface resistance of the 100 nm aluminum reflector on top of the grating, and concentration of surface currents on the reflector edges and grating clamps. Simulations have shown the latter is the most detrimental effect. The grating measures $21 \times 21\,\mathrm{mm}^2$, all of which is covered by the grating reflector. Only $20 \times 20\,\mathrm{mm}^2$ is effectively patterned, leaving a 0.5 mm rim on the grating edge that could be used to ensure electrical contact with the cavity. If, in the current cavity design, the grating were clamped below a $20 \times 20\,\mathrm{mm}^2$ square, 1 mm deep hole in the cavity back wall, the cavity Q-factor is expected to increase to $Q_{\mathrm{cav}} \sim 3000$. A cross section of the cavity back wall in the new situation is shown in Fig. 7.1. The increase in Q-factor measures about a factor 6. When achieved in practice, a similar increase in MCRS measurement sensitivity can be expected (see Eq. 3.22). Note there is an aluminum slab behind the grating in Fig. 7.1 to mitigate concentration of the cavity electric field on the hole edge facing the cavity interior. The slab prevents power loss through the hole in the cavity wall behind the grating as well. The latter can also be achieved by increasing the hole length, as is done with the hole for the trapping laser in Ch. 4.

Spatial information about the UCP electron density can be obtained by conducting multi-mode MCRS, as demonstrated in Ref. [7]. In the current cavity design the next cavity mode is located at 6.6 GHz, close to the cut-off frequency of the hole for the trapping laser. The mode is not isolated from the cavity exterior, has a low Q-factor ($Q_{\mathrm{cav}} \sim 100$), and is out-of-reach for the microwave generator and directional coupler used in the experiment. In a redesign of the microwave cavity, the cavity radius could be increased to lower the mode resonance frequency. This would increase the mode Q-factor and bring it within reach of excitation and detection with the current microwave setup. Potentially other cavity modes could be brought within reach as well. Investigating the spatial evolution of the UCP electron density distribution is interesting in its own right. However, multi-mode MCRS opens the door to resolving patterned initial plasma distributions as well. For example, by modulating the intensity profile of the excitation and/or the ionization laser we could study the evolution and interaction of two or more adjacent UCPs.

Bibliography

[1] G. E. Moore. "Cramming More Components onto Integrated Circuits." In: *Electronics* 38.8 (1965), pp. 114–117.

[2] M. V. Klein. *Optics*. Wiley, 1970. ISBN: 0471490806.

[3] R. M. van der Horst. "Electron dynamics in EUV-induced plasmas." PhD thesis. Department of Applied Physics, Nov. 2015. ISBN: 978-90-386-3947-5.

[4] A. Yen, H. Meiling, and J. Benschop. "EUV Lithography at Threshold of High-Volume Manufacturing." In: *2018 IEEE International Electron Devices Meeting (IEDM)*. Dec. 2018. DOI: 10.1109/IEDM.2018.8614502.

[5] F. M. J. H. van de Wetering. "Formation and dynamics of nanoparticles in plasmas." en. PhD thesis. Eindhoven University of Technology, 2016. DOI: 10.6100/f3331ca8-0d98-4cf4-92cb-58a6a8ca047c.

[6] R. F. Harrington. *Time-Harmonic Electromagnetic Fields*. Wiley-Blackwell, 2001. 496 pp. ISBN: 978-0-471-20806-8.

[7] J. Beckers, F. M. J. H. van de Wetering, et al. "Mapping electron dynamics in highly transient EUV photon-induced plasmas: a novel diagnostic approach using multi-mode microwave cavity resonance spectroscopy." In: *Journal of Physics D: Applied Physics* 52.3 (Nov. 2018), p. 034004. DOI: 10.1088/1361-6463/aaeb17.

[8] W. J. Engelen. "Coherent Electron Bunches from Laser-Cooled Gases." PhD thesis. Eindhoven University of Technology, 2013. ISBN: 9789038634340.

[9] H. J. Metcalf and P. van der Straten. *Laser Cooling and Trapping*. Springer, 1999. 323 pp. ISBN: 9780387987286.

[10] T. C. Killian, T. Pattard, et al. "Ultracold neutral plasmas." In: *Physics Reports* 449.4-5 (Sept. 2007), pp. 77–130. DOI: 10.1016/j.physrep.2007.04.007.

[11] M. Lyon and S. L. Rolston. "Ultracold neutral plasmas." In: *Reports on Progress in Physics* 80.1 (Nov. 2016), p. 017001. DOI: 10.1088/0034-4885/80/1/017001.

[12] J. G. H. Franssen, T. C. H. de Raadt, et al. "Compact ultracold electron source based on a grating magneto-optical trap." In: *Physical Review Accelerators and Beams* 22.2 (Feb. 2019). DOI: 10.1103/physrevaccelbeams.22.023401.

[13] C. C. Nshii, M. Vangeleyn, et al. "A surface-patterned chip as a strong source of ultracold atoms for quantum technologies." In: *Nature Nanotechnology* 8.5 (Apr. 2013), pp. 321–324. DOI: 10.1038/nnano.2013.47.

[14] E. W. Streed, A. P. Chikkatur, et al. "Large atom number Bose-Einstein condensate machines." In: *Review of Scientific Instruments* 77.2 (Feb. 2006), p. 023106. DOI: 10.1063/1.2163977.

[15] J. F. Barry, D. J. McCarron, et al. "Magneto-optical trapping of a diatomic molecule." In: *Nature* 512.7514 (Aug. 2014), pp. 286–289. DOI: 10.1038/nature13634.

[16] J. Miao, J. Hostetter, et al. "Magneto-optical trapping of holmium atoms." In: *Physical Review A* 89.4 (Apr. 2014). DOI: 10.1103/physreva.89.041401.

[17] B. J. Claessens. "Dynamics and Applications of Excited Cold Atoms." PhD thesis. Eindhoven University of Technology, 2006. ISBN: 90-386-2531-6.

[18] D. A. Steck. *Rubidium 85 D Line Data*. Version 2.1.6. Sept. 20, 2013. URL: http://steck.us/alkalidata.

[19] Ankit Rohatgi. *Web Plot Digitizer*. URL: https://apps.automeris.io/wpd/ (visited on 09/2018).

[20] A. Nadeem and S. U. Haq. "Photoionization from the $5p^2P_{3/2}$ state of rubidium." In: *Physical Review A* 83.6 (June 2011). DOI: 10.1103/physreva.83.063404.

[21] J. A. Bittencourt. *Fundamentals of Plasma Physics*. Springer New York, 2004. ISBN: 9781475740301.

[22] J. T. Mendonça and H. Terças. *Physics of Ultra-Cold Matter*. Springer New York, 2012. 420 pp. ISBN: 9781461454120.

[23] S. Kulin, T. C. Killian, et al. "Plasma Oscillations and Expansion of an Ultracold Neutral Plasma." In: *Physical Review Letters* 85.2 (July 2000), pp. 318–321. DOI: 10.1103/physrevlett.85.318.

[24] X. L. Zhang, R. S. Fletcher, et al. "Ultracold Plasma Expansion in a Magnetic Field." In: *Physical Review Letters* 100.23 (June 2008). DOI: 10.1103/physrevlett.100.235002.

[25] M. A. W. van Ninhuijs. "Time-of-Flight Electron Energy Loss Spectroscopy by using miniaturized RF technology." Master's Thesis. Eindhoven University of Technology, Mar. 2016.

[26] D. M. Pozar. *Microwave Engineering*. John Wiley & Sons Inc., 2012. 752 pp. ISBN: 9780470631553.

[27] J. R. Rumble, ed. *CRC Handbook of Chemistry and Physics*. CRC Press. URL: http://hbcponline.com (visited on 09/2018).

[28] T. van Oudheusden. "Electron source for sub-relativistic single-shot femtosecond diffraction." PhD thesis. Eindhoven University of Technology, 2010.

[29] CST AG. *CST Studio Suite 2017*. Comp. software. Version 2017.05. Aug. 4, 2017.

[30] W. Verhoeven. "Ultrafast electron microscopy and spectroscopy using microwave cavities." PhD thesis. Eindhoven University of Technology, 2018. ISBN: 978-90-386-4590-2.

[31] B. Gyüre, B. G. Márkus, et al. "A time domain based method for the accurate measurement of Q-factor and resonance frequency of microwave resonators." In: *Review of Scientific Instruments* 86.9 (Sept. 2015). Supplementary Material, p. 094702. DOI: 10.1063/1.4929865.

[32] D. Alesini. "Power coupling." In: *CERN Yellow Report CERN-2011-007, pp. 125-147* (Dec. 14, 2011). arXiv: 1112.3201.

[33] R. E. Collin. *Foundations for Microwave Engineering - 2nd edition*. Wiley-IEEE Press, 2001. ISBN: 0-7803-6031-1.

[34] F. M. J. H. van de Wetering. *Personal communication*. Trieste, Nov. 20, 2017.

[35] M. A. Lieberman. *Principles of Plasma Discharges and Materials Processing*. Wiley-Blackwell, 2005. ISBN: 0471720011.

[36] J. G. H. Franssen. "An ultracold and ultrafast electron source." PhD thesis. Eindhoven University of Technology, 2019. ISBN: 9789038647319.

[37] B. Savoie. "A rigorous proof of the Bohr–van Leeuwen theorem in the semiclassical limit." In: *Reviews in Mathematical Physics* 27.08 (2015), p. 1550019. DOI: 10.1142/s0129055x15500191.

[38] C. J. Dedman, K. G. H. Baldwin, and M. Colla. "Fast switching of magnetic fields in a magneto-optic trap." In: *Review of Scientific Instruments* 72.11 (Nov. 2001), pp. 4055–4058. DOI: 10.1063/1.1408935.

[39] CST AG. *CST Studio Suite 2017*. Materials Library. Comp. software. Version 2017.05. Aug. 4, 2017.

[40] J. C. Slater. *Microwave Electronics*. Dover Publications Inc., 1969.

[41] J. van Gemerden. *Technische informatie voor werktuigbouwkundigen*. (Dutch). Wolters-Noordhoff Groningen, 2000. ISBN: 9001331076.

[42] A. Rosa, D. Tulli, et al. "Barium titanate ($BaTiO_3$) RF characterization for application in electro-optic modulators." In: *Optical Materials Express* 7.12 (Nov. 2017), p. 4328. DOI: 10.1364/ome.7.004328.

[43] T. C. H. de Raadt. "Ultra-cold electron source. Ponderomotive measurement of self-compression." Master's Thesis. Eindhoven University of Technology, 2019.

[44] M. A. W. van Ninhuijs, K. A. Daamen, et al. "Microwave cavity resonance spectroscopy of ultracold plasmas." 2019. Submitted for publication.

Appendix

Reflection on a Right-Angle Connector

When the microwave cavity was installed on the CF100 flange a curious drop in coupling factor β was observed, as measured on the atmospheric side of the CF100 flange. For a critically coupled cavity ($\beta \approx 1$) the coupling factor, as measured on the flange ((2) in Fig. 4.11), was reduced by about $\Delta\beta = -0.2$. For experiments the cavity (without flange) was left slightly overcoupled ($\beta = 1.21$) to have a coupling factor close to the planned $\beta = 1$ with the flange.

On the vacuum side of the CF100 flange, the microwave signal is transported to the cavity by a semi-rigid coax cable, see Fig. 4.12. To investigate the drop in coupling factor, the semi-rigid coax cable (cable I) was replaced by a cable with straight-angle connectors (cable II). A photo of both cables is shown in Fig. 1. For both cables, the voltage reflection coefficient $|\Gamma_V|$ was measured on the flange with the use of a network analyzer. Measurements on the flange (label: with flange) are compared to measurements without flange (label: without flange) in Fig. 2 and fitted with Eq. 4.1 to determine the microwave cavity characteristics. Fit results are listed in Table 1. In the figure, the reflection measurement without flange is shown by the black line. The coupling factor $\beta = 1.21$ (see Table 1) leads to a on-resonance voltage reflection of 10% (1% in power) apparent in the peak (minimum) of the reflection curve. With the flange and cable I (orange line) the coupling factor drops to $\beta = 1.06$ and the on-resonance voltage reflection improves to 4% (2‰ in power). This effect disappears when the cable I is replaced by cable II (red line). With cable II the coupling factor remains $\beta = 1.21$ and the on-resonance voltage reflection is 11%. A marginal difference with the situation without the flange.

The main difference between cable I and II is that the latter does not contain a right-angle connector. In the right-angle connector the microwave signal is forced in a 90° turn (right angle) in a propagation distance of a few millimeters. Since the wavelength of a 5 GHz microwave signal propagating on a coax cable is about 4 cm, taking a 90° turn in a propagation distance of a few millimeters is bound to cause reflections. A reflection of 1% of microwave power (10% voltage) on the right-angle connector could explain the drop in on-resonance reflection when the cavity is installed on the flange with the semi-rigid coax cable. In future experiments right-angle connectors should be avoided in the transmission line. Also apparent in Fig. 4.12 is the off-resonance drop in reflected voltage in the wings of the reflection peak when the cavity is installed on the flange (both with cable I and II). This effect is due to dissipation in the extra piece of transmission line of the SMA-feedthrough in the flange and the cables. Obviously cable II is of lesser quality and dissipates more.

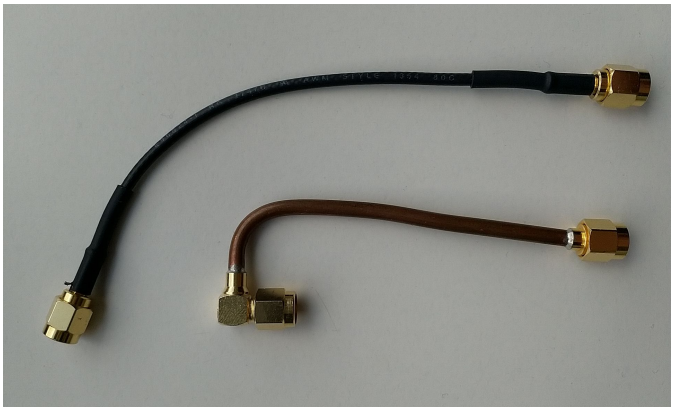

Figure 1: Coax cables used for testing. Bottom – semi rigid coax cable with right-angle connector used in the experiment (cable I). Top – non-UHV compatible coax cable with only straight-angle connectors (cable II).

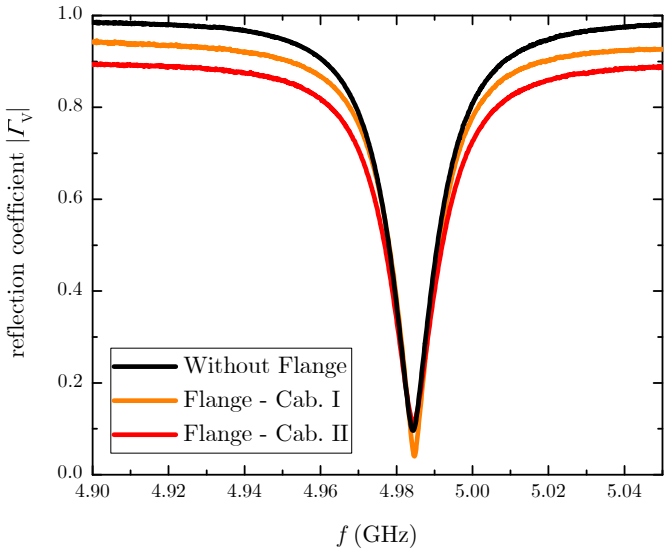

Figure 2: Measured voltage reflection coefficient $|\Gamma_V|$ as a function of frequency for the cavity TM_{010} mode. Comparison between measurements on the cavity (label: without flange), on the flange with cable I (label: flange - cab. I) and on the flange with cable II (label: flange - cab. II). Cavity characteristics of all situations are listed in Table 1.

Table 1: Comparison of microwave cavity characteristics without flange, flange with cable I and flange with cable II. Data obtained from fitting the graphs in Fig. 2 with Eq. 4.1. Measurement errors are beyond the last digit.

	f_0 (GHz)	β	Q_L
Without Flange	4.98	1.21	222
Flange - Cab. I	4.99	1.06	229
Flange - Cab. II	4.98	1.21	208